11-14-2014

# An Investigation on Biocompatibility of Bio-Absorbable Polymer Coated Magnesium Alloys

Sushma Amruthaluri
Samru001@fiu.edu

**DOI:** 10.25148/etd.FI14032310

FLORIDA INTERNATIONAL UNIVERSITY

Miami, Florida

# AN INVESTIGATION ON BIOCOMPATIBILITY OF BIO-ABSORBABLE POLYMER COATED MAGNESIUM ALLOYS

A dissertation submitted in partial fulfillment of the

requirements for the degree of

DOCTOR OF PHILOSOPHY

in

MATERIAL SCIENCE AND ENGINEERING

by

Sushma Amruthaluri

2014

To: Dean Amir Mirmiran
College of Engineering and Computing

This dissertation, written by Sushma Amruthaluri, and entitled An Investigation on Biocompatibility of Bio-Absorbable Polymer Coated Magnesium Alloys, having been approved in respect to style and intellectual content, is referred to you for judgment.

We have read this dissertation and recommend that it be approved.

_____
Kinzy Jones

_____
Arvind Agarwal

_____
Anthony McGoron

_____
Sharan Ramaswamy

_____
Benjamin Boesl

_____
Norman Munroe, Major Professor

Date of Defense: November 14, 2014

The dissertation of Sushma Amruthaluri is approved.

_____
Dean Amir Mirmiran
College of Engineering and Computing

_____
Dean Lakshmi N. Reddi
University Graduate School

## DEDICATION

I am blessed with a loving and caring family with whose support and encouragement I accomplished this research. I dedicate this dissertation to my family.

To my mother : the greatest gift I ever received from heavens

To my sister : my never failing friend

To my brother-in-law: source of support and encouragement

To my husband : caring and loving person and my greatest blessing

To my daughter : my tiny bundle of joy

This is a tribute I pay to my family as an expression of gratitude.

ACKNOWLEDGMENTS

Travelling from an eastern country – landing in a western country – pursuing Ph.D. at Florida International University (FIU) – a journey from a land of intuition to a land of science and technology is something that I never dreamt in my life. Hence, it is with great pleasure that I acknowledge the people and the organizations associated with this major task in my academic life. First and foremost, I salute thee: Florida International University – for providing this rare opportunity.

It is my great pleasure to acknowledge the people who have provided support, guidance and encouragement.

With immense pleasure and special appreciation I express my deep sense of gratitude to my advisor, Dr. Norman Munroe for his patient guidance and parental caring. He has been a tremendous mentor for me, encouraging my research and allowing me to grow as research scientist. His suggestions on both research as well as my career have been priceless. Dr. Munroe's intellectual heft is matched only by his genuinely good nature and down-to-earth humility and I am truly fortunate to have had the opportunity to work with him. He encouraged me to grow not only as an experimentalist and an engineer but also as an instructor and an independent thinker. He has taught me to challenge myself and stretch my imagination despite any limitations. He has always been there to listen and give me advice. I am deeply grateful to him for spending time on long discussions to sort out technical details of my work.

I would like to express my gratitude and special appreciation to my committee members, Dr. Benjamin Boesl, Dr. Kinzy W. Jones, Dr. Arvind Agarwal, Dr. Anthony McGoron, and Dr. Sharan Ramaswamy for their precious guidance and thought

provoking suggestions that each of them offered to me over the years. Dr. Benjamin Boesl has been like a second advisor to me. I am thankful for his aspiring guidance and honest advices. His encouraging words during my research work helped me focus my ideas. I am sincerely grateful to Dr. Sharan Ramaswamy for sharing his illuminating views on a number of issues related to the research. I specially thank him for providing great assistance with his research facilities for hemocompatibility studies. I sincerely thank Dr. Kinzy W. Jones for his insightful comments and constructive criticisms at different stages of my research. I am indebted to him for his suggestions and timely feedback on mechanical testing. I am especially thankful to Dr. Arvind Agarwal for his continuous encouragement, support and timely feedback. I express my deepest thanks to Dr. Anthony McGoron for his careful and precious guidance which were extremely valuable for my study. I take this opportunity to acknowledge his guidance in conducting experiments on biocompatibility studies.

I would like to convey my special thanks to Dr. Hakan Engqvist and Mr. Wei Xia who assisted in conducting XPS and polymer adhesion tests at Uppsala University. I would like to thank Mr. Ryszard Rokicki from Electrobright® for sample preparation and Dr. Hassan Mahfuz and Mr. Sabet for assisting with the performance of tensile tests. My special thanks to Neal Ricks, Alexander Franco and Tom Beasley for assisting me to utilize Advanced Materials Engineering Research Institute (AMERI) and Florida Center for Analytical Electron Microscopy (FCAEM) facilities for surface characterization analyses. I would like to express my gratitude to Dr. Yong Cai and Dr. Guangliang Liu from the Department of Chemistry and Biochemistry for permitting me to use their Inductively Coupled Mass Spectrometer (ICP-MS).

I sincerely thank Dr. Puneet Gill, for his informative discussions and spears of ideas. Special word of thanks go to Abhignyan Nagesetti who provided extensive assistance in bio related studies and Phani Kiran Vabbina who assisted me in building a dip coating setup.

I appreciate the effort of my group members Dr. Chandan Pulletikurthi and Vishal Musaramthota. My sincere thanks are extended to them for their invaluable contribution.

Most importantly, none of this would have been possible without the love and patience of my family to whom this dissertation is dedicated to. They have been a constant source of love, concern and strength all these years. I express my heartfelt gratitude to my mother, sister, and brother-in-law. I would like to express appreciation to my husband who was always my support to overcome many crisis situations and finish this dissertation. With immense appreciation I acknowledge my two month old daughter Krithi Ghantasala for her cooperation during her presence in my womb and also after delivery. I also express my appreciation to my nephew Reyhaan Thummadi and my niece Avlokitha Thummadi, whose smiley faces and innocent words boosted my strength and refreshed my mind. I thank all my friends, Aishwarya Raghavan, Sudheer Chinta, Neha Chawla, Aditya Katragadda, Raghavendra Khadakbhavi and Bala Ponnusamy for providing immense support and help in times of need.

Finally, once again, I thank everyone who made a meaningful contribution to my dissertation.

ABSTRACT OF THE DISSERTATION

AN INVESTIGATION ON BIOCOMPATIBILITY OF BIO-ABSORBABLE POLYMER COATED MAGNESIUM ALLOYS

by

Sushma Amruthaluri

Florida International University, 2014

Miami, Florida

Professor Norman Munroe, Major Professor

Advances in biomaterials have enabled medical practitioners to replace diseased body parts or to assist in the healing process. In situations where a permanent biomaterial implant is used for a temporary application, additional surgeries are required to remove these implants once the healing process is complete, which increases medical costs and patient morbidity. Bio-absorbable materials dissolve and are metabolized by the body after the healing process is complete thereby negating additional surgeries for removal of implants.

Magnesium alloys as novel bio-absorbable biomaterials, have attracted great attention recently because of their good mechanical properties, biocompatibility and corrosion rate in physiological environments. However, usage of magnesium as biodegradable implant has been limited by its poor corrosion resistance in the physiological solutions. An optimal biodegradable implant must initially degrade slowly to ensure total mechanical integrity for desired structural support of biological tissue then degrade over time as the tissue heals.

The current research focuses on surface modification of magnesium alloys by surface treatment and polymer coating in an effort to enhance corrosion rate and biocompatibility. It is envisaged that the results obtained from this investigation would provide the academic community with insights for the utilization of bio-absorbable implants particularly for patients suffering from atherosclerosis.

The alloying elements used in the current research are zinc and calcium both of which are essential minerals in the human metabolic and healing processes. A hydrophobic biodegradable co-polymer, polyglycolic-co-caprolactone (PGCL), was used to coat the surface treated Mg-Zn-Ca (MZC) in order to retard the initial degradation rate. Two surface treatments were selected: (a) acid etching and (b) anodization to produce different surface morphologies, roughness, surface energy, chemistry and hydrophobicity that are pivotal for PGCL adhesion onto the MZC. Additionally, analyses of biodegradation, biocompatibility, and mechanical integrity of surface treated MZC were performed against the PGCL coated MZC in order to investigate the optimum surface modification process, suitable for biomaterial implants.

The results of the current research showed that anodization created better adhesion between the MZC and PGCL coating. Furthermore, PGCL coated anodized MZC exhibited lower corrosion rate, good mechanical integrity, and better biocompatibility as compared with acid etched.

TABLE OF CONTENTS

CHAPTER PAGE

LIST OF TABLES

TABLE PAGE

LIST OF FIGURES

FIGURE PAGE

ABBREVIATIONS

| | |
|---|---|
| AE | Acid Etching |
| ANOVA | Analysis of Variance |
| ASTM | American Society for Testing Materials |
| ATR- FTIR | Attenuated Total Reflectance Fourier Transform Infrared Spectroscopy |
| BAS | Bio Absorbable Stents |
| BM | Bare Metal |
| BMS | Bare Metallic Stents |
| CA | Contact Angle |
| CAD | Coronary Artery Disease |
| CRT | Cardiovascular Research Technologies |
| DCM | Dichloro methane |
| DES | Drug Eluting Stents |
| DMEM | Dulbecco's Modified Eagle Medium |
| DNA | Deoxyribonucleic Acid |
| DPBS | Dulbecco's Phosphate Buffered Saline |
| EDS | Energy Dispersive Spectroscopy |
| EIS | Electrochemical Impedance Spectroscopy |
| FBS | Fetal Bovine Serum |
| FDA | U.S. Food and Drug Administration |
| FP | Fractional Polarity |
| FTIR | Fourier transform infrared spectroscopy |

| | |
|---|---|
| HA | Hydroxy Apatite |
| HCP | Hexagonal Closed Packed |
| HMW | High Molecular Weight |
| HUVEC | Human Primary Umbilical Vein Endothelial Cells |
| IC | Integrated Circuits |
| ICP-MS | Inductively Coupled Mass Spectroscopy |
| ISO | International Organization for Standardization |
| LMW | Low Molecular weight |
| MALPB | Maleic anhydride-g-liquid polybutadiene |
| MP | Mechanical Polishing |
| MZC | Magnesium-Zinc-Calcium |
| MZC | Magnesium -Zinc-Calcium |
| NSF | Nephrogenic Systemic Fibrosis |
| PBS | Phosphate Buffer Saline |
| PC | Polymer Coated |
| PCL | Poly (caprolactone) |
| PDLA | Poly(D-lactide), |
| PEI | Polyether imide |
| PEO | Plasma Electrolytic Oxidation |
| PGA | Poly (glycolic acid) |
| PGCL | poly(glycolide-co-ε-caprolactone) |
| PLA | Poly (lactic acid) |

| | |
|---|---|
| PLGA | Poly(lactic-co-glycolic acid) |
| PLLA | Poly (l-lactic acid) |
| PTCA | Percutaneous Transluminal Coronary Angioplasty |
| PTMC | Poly(trimethylene carbonate) |
| PVA | Polyvinyl acetate |
| PVDF | Polyvinylidene difluoride |
| RE | Rare Earth |
| RF | Radio Frequency |
| RNA | Ribonucleic Acid |
| Rpm | Revolutions Per Minute |
| SBF | Simulated Body Fluid |
| SEM | Scanning Electron Microscopy |
| SFE | Surface Free Energy |
| SRB | Sulforhodamine B Assay |
| SS | Stainless Steel |
| XPS | X-ray Photoelectron Spectroscopy |
| XRD | X-ray Diffraction |

NOMENCLATURE

| | |
|---|---|
| A | Aluminum |
| Al | Angstrom |
| $A^o$ | Cysteine |
| C | Capacitance Double Layer |
| $C_{dl}$ | Copper |
| Cu | Dispersion |
| D | Corrosion Potential |
| $E_{corr}$ | Equivalent Weight |
| EW | Iron |
| Fe | Fractional Polarity |
| FP | Gibbs Free Energy |
| G | Hydrogen bond |
| H | Hydrogen |
| $H_2$ | Sulphuric Acid |
| $H_2SO_4$ | Hydrofloric acid |
| HF | Corrosion Current |
| $I_{corr}$ | Potassium |
| K | Ostwald solubility coefficient |
| L | Molecular Mass |
| M | Magnesium |
| Mg | Magnesium Hydroxide |

| | |
|---|---|
| $Mg(OH)_2$ | Magnesium Oxide |
| MgO | Sodium Chloride |
| NaCl | Nitinol |
| NiTi | Oxygen |
| O | Celsius |
| $^{o}C$ | Polar |
| P | Phosphorous |
| P | Glutamine |
| Q | Charge Transfer Resistance |
| $R_{ct}$ | Pilling-Bedworth Ratio |
| RPB | Solution Resistance |
| $R_s$ | Time |
| T | Molar Volume |
| V | Tryptophan |
| W | Weight Percentage |
| Wt % | Film Thickness |
| Y | Film Thickness |
| Y | Impedance (real) |
| Z’ | Impedance (imaginary) |
| Z” | Zinc |
| Zn | Contact Angle Between Solid and Liquid |
| $\theta_i$ | Wavelength |

| | |
|---|---|
| Λ | Micro meters |
| μm | Poisson's Ratio |
| N | Density |
| P | Surface Tension Contributed by Base (testing surface, s) |

# 1. INTRODUCTION

## 1.1 Research Background

The use of metals and other materials to repair the human body has been recorded for centuries, dating back several millennia [1]. Advances in biomaterials have enabled medical practitioners to replace diseased body parts or to assist in the healing process. While the former application requires biomaterial implants to stay in the body permanently, the latter application only requires that the implant remain in the body temporarily. In situations where a permanent implant is used for a temporary application, additional surgeries are required to remove these implants once the healing process is complete [2]. This removal process increases the cost and patient morbidity [2].

Biodegradable materials dissolve after the healing process is complete and therefore no additional surgeries are required for removal of these implants [2]. This eliminates the complications associated with long-term presence of implants in the body. However, once these materials degrade within the body, it is important that the degradation products are able to be metabolized or eliminated by the body, and are thus bio-absorbable. Polymers were the first materials to be used as commercial biodegradable and bio-absorbable implant materials. However, the use of these materials is limited by their low strength and radiopacity [3]. Metals have more desirable mechanical properties due to their relatively high strength and fracture toughness [2]. However, studies have shown that the majority of metals that are used as conventional surgical alloys, such as stainless steel, cobalt, chromium, and nickel produce corrosion products, which could be harmful to the human body [4].

Magnesium alloys as a new kind of biodegradable and bio-absorbable medical material, have attracted great attention recently for their good mechanical properties, biocompatibility, and fast corrosion rate in the physiological environment [5]. Magnesium has an advantage over other degradable biomaterials in that it can have lower mass for equal mechanical performance and can be better visualized in CT (computerized tomography) scans [6]. Furthermore, corrosion and degradation of magnesium lead to the formation of harmless corrosion products which are excreted during urination. Unlike other metals such as stainless steel and titanium alloys, the interface between the magnesium based implants and biological environment is dynamic. Also, magnesium is essential to human metabolism and is the fourth most abundant cation in the human body [7]. Magnesium is also a cofactor for many enzymes and stabilized structures of deoxyribonucleic acid (DNA) and ribonucleic acid (RNA) [7]. Accordingly, magnesium alloys which consist of trace elements that exist in the human body are promising candidates as temporary implant materials. Biodegradable magnesium alloys are being considered for several biomedical applications such as cardiovascular stents, bone fixation, and even stomach trauma repair.

On the other hand, the major limitation of magnesium is its low corrosion resistance which results in rapid release of degradation products. A high rate of degradation under physiological conditions can cause a reduction in the mechanical integrity of the implant before the healing process is complete.

Surface modification is therefore a promising approach to enhance the performance of magnesium based biomaterials [8]. In order to improve the surface properties to enable better and more expeditious adaptation to the physiological

surroundings, it is imperative to design and construct a surface to satisfy multiple clinical requirements such as mechanical strength, biocompatibility and degradation rate.

This research focuses on the surface modification of magnesium based biomaterials by surface treatment and polymer coating in order to improve corrosion resistance and biocompatibility. It is envisaged that the results obtained from this investigation would provide the academic community with insights for the utilization of bio-absorbable implants particularly for patients suffering from coronary artery diseases (CAD) such as atherosclerosis.

### 1.2 Coronary Artery Disease (CAD)

CAD is the leading cause of death in the United States and it accounts for almost 25 percent of deaths each year [9]. CAD is usually caused by atherosclerosis, a narrowing of the coronary arteries due to plaque formation (Figure 1.1). Plaque is generally formed when infiltrated cholesterol in the coronary artery accumulates with white blood cells that narrows an artery and hinders blood flow. In order to cover the plaque, the body triggers neointimal hyperplasia (scar tissue due to smooth muscle cell proliferation). However, the atherosclerotic plaque sometimes tears, exposing muscle tissue that stimulates clot formation (thrombosis) which in turn may obstruct blood flow and commence events that lead to heart attack that can damage or destroy a part of the heart muscle.

One of the most common invasive surgical method to successfully treat CAD is percutaneous transluminal coronary angioplasty (PTCA) [9, 10]. Angioplasty is a medical procedure in which a balloon mounted onto a catheter is used to open a narrowed or blocked coronary artery. Once the catheter is positioned in the narrowed blood vessel, a

balloon is repeatedly inflated and deflated to stretch or break open the blocked area. The major limitation of balloon angioplasty is arterial elastic recoil whereby the artery shrinks within minutes or hours after angioplasty and can result in up to 50 percent reduction in vessel diameter, especially at the location where there was no atherosclerosis prior to the angioplasty. In order to overcome artery recoil and improve long-term stability, coronary stents are implanted [11].

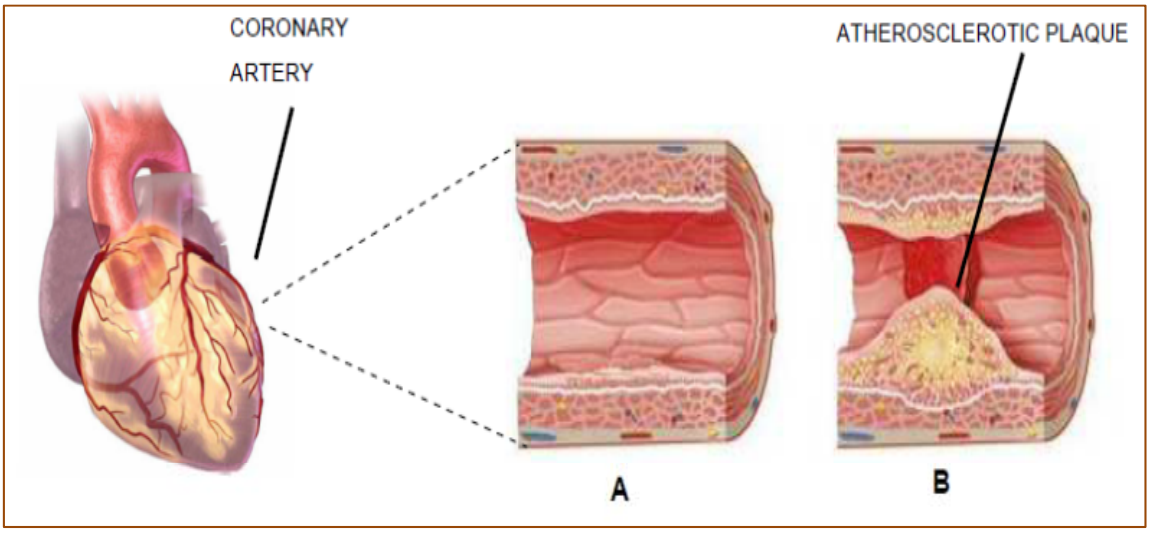


Figure 1.1: Atherosclerosis; A: Healthy coronary artery, B: Coronary artery with plaque

A coronary stent is an artificial support device that is placed in the coronary artery to keep the vessel open after treatment of coronary artery disease. The stent is usually a mesh tube that is available in various sizes to match the size of the artery and to hold it open after the blockage has been treated. Over 3 million patients worldwide use stents manufactured predominantly from stainless steel (SS316), whereas approximately 15 percent of patients use Nitinol (NiTi) or nickel-cobalt alloys [12].

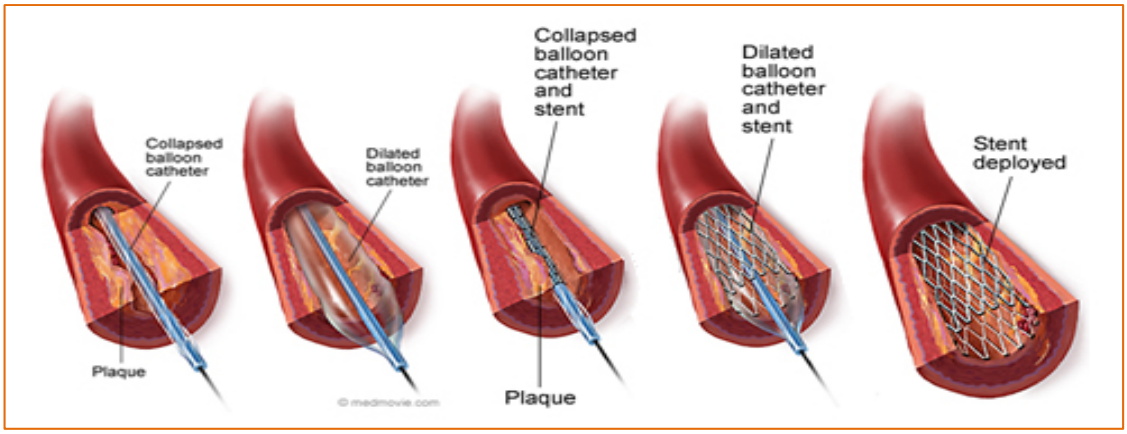


Figure 1.2: Stent deployment process via balloon angioplasty

Coronary stents developed to date can be grouped into three categories namely:

- Bare-metal stents (BMS)
- Drug-eluting stents (DES)
- Bio-absorbable stents (BS)

### 1.3 Bare-Metal Stents (BMS)

Bare metal first-generation stents are typically made of stainless steel or cobalt-chromium alloy. Although BMS were able to restore blood perfusion through the vessel, it was fraught with the occurrence of restenosis (excessive cell proliferation and thrombosis, or blood clot formation) in 20 to 30 percent of patients within the first six months of implantation [13]. Additionally, long-term endothelial dysfunction or chronic inflammatory reaction occurred with BMS due to continuous contact with surrounding tissue. The aforementioned problems contribute to late restenosis [14, 15] and in-stent restenosis (occurs between 3 to 6 months [16] after implantation). These limitations of BMS led to the development of Drug-eluting stents (DES).

### 1.4 Drug-Eluting Stents (DES)

Drug eluting stents (DES) are metal stents that are coated with three layers of polymers that contain antiproliferative drugs such as: paclitaxel, everolimus, sirolimus, zotarolimus that were previously used for other medical applications. However, new drugs are also being evaluated for coronary stent applications [17]. Antiproliferative drugs mainly prevent in-stent restenosis by inhibiting neointimal growth [18]. Once the therapeutic process is accomplished, there still remains the issue of the bare metal and the degraded polymer coating, which is prone to release debris that may cause inflammatory reactions [19]. Table 1.1 summarizes various DES under development [20]. The current U.S market is dominated by two DES: the Taxus by Boston Scientific Co. (BSC) and the Cypher by Johnson & Johnson Inc. (J&J).

Table 1.1: Various DES under development [20]

| Manufacturer | Trade name | Stent | Polymer | Drug |
|---|---|---|---|---|
| Abbot | ZoMaxx | Tantulum/SS | Durable | Zotarolimus |
| Boston Scientific | Taxus | SS | Durable | Taxus |
| Cordis (J & J) | Cypher | SS | Bio-absorbable | Everolimus |
| Terumo | Nobori | SS | Bio-absorbable | Biolimus-A9 |
| SS - Stainless Steel | | | | |

### 1.5 Biodegradable Stents (BS)

Permanent stents (BMS and DES) provide no advantage beyond the healing time however, their prolonged presence increases the possibility of thrombosis [21]. One of the possible solutions to these limitations is the usage of biodegradable stents. The main criterion of a biodegradable stent is to inhibit the obstruction of a vessel and vasoconstriction in the coronary artery for a period of 6 to 12 months. Once these stents

are fully absorbed, only the healed vessels are left behind with no residual prosthesis. This negates the formation of thrombus, inflammatory response in the artery and long-term antiplatelet therapy. In general, the usage of bio-absorbable stents avoid the need for a second operation for stent removal, which, besides being beneficial to the patient, reduces medical costs in the health system.

The need of biodegradable stent is particularly important for pediatric cases where there is continuous change in the body due to growth. Permanent implants would not match this continuous change of growth, due to which repeated surgery becomes necessary. The clinical characteristics of BS, BMS and DES are summarized in Table 1.2. This table shows that restenosis occurs in 5 – 10 percent of patients with implanted DES and BS as compared with 20-30 percent of patients with BMS. It should also be noted that the risk of late thrombosis and can be avoided if the BS is fully absorbed. This negates long-term antiplatelet therapy and other complications associated with vessel remodeling, CT and MRI imagery [22].

Table 1.2: Clinical characteristics of BMS, DES, and BS [22]

| | **BMS** | **DES** | **BS** |
|---|---|---|---|
| Restenosis | 20-30% | 5-10% | 5-10% |
| Acute thrombosis | *** | *** | *** |
| Late thrombosis | * | ** | 0, if fully absorbed |
| Vessel remodeling | 0 | 0 | ** |
| Vasomotion | 0 | 0 | ** |
| CT or MRI studies | 0 | 0 | ** |
| Side branch jail | 0 | 0 | ** |
| Strut fracture | * | * | 0, if fully absorbed |
| Need for dual antiplatelet | * | ** | 0, if fully absorbed |

| | | | |
|---|---|---|---|
| Precise need for balloon sizing | * | * | ***, less tolerance for over expansion |
| Strut thickness | ** | * | *** |
| Flexibility | ** | ** | *** |
| Hinder CABG in future | *** | *** | 0, if fully absorbed |
| Strut thickness (μm) | ~ 60-120 [23] | ~ 60-120 [23] | ~150 - 170 [24] |
| BMS = bare-metal stents, DES = drug-eluting stents, BAS = biodegradable stents | | | |
| *, **, *** indicate low to high likelihood of event or degree of characteristic | | | |

### 1.6 Biodegradable Stent Market

Since 2008, it has been projected that the unit volume shares of the biodegradable stent market has increased from 0.1 percent to 18 percent by the year 2017 as shown in Figure 1.3. Currently, DES dominates the coronary stent landscape worldwide. However, due to the aforementioned problems associated with the DES, the emergence of advanced materials and technologies have led to the development of the next generation absorbable/biodegradable stents. As quoted by Dr. Patrick Serruys at Cardiovascular Research Technologies (CRT) 2007, "Abolition of neointimal hyperplasia is no longer the ultimate goal. Development of more biocompatible and biodegradable stents facilitating adequate endothelialization is expected in the near future [25]."

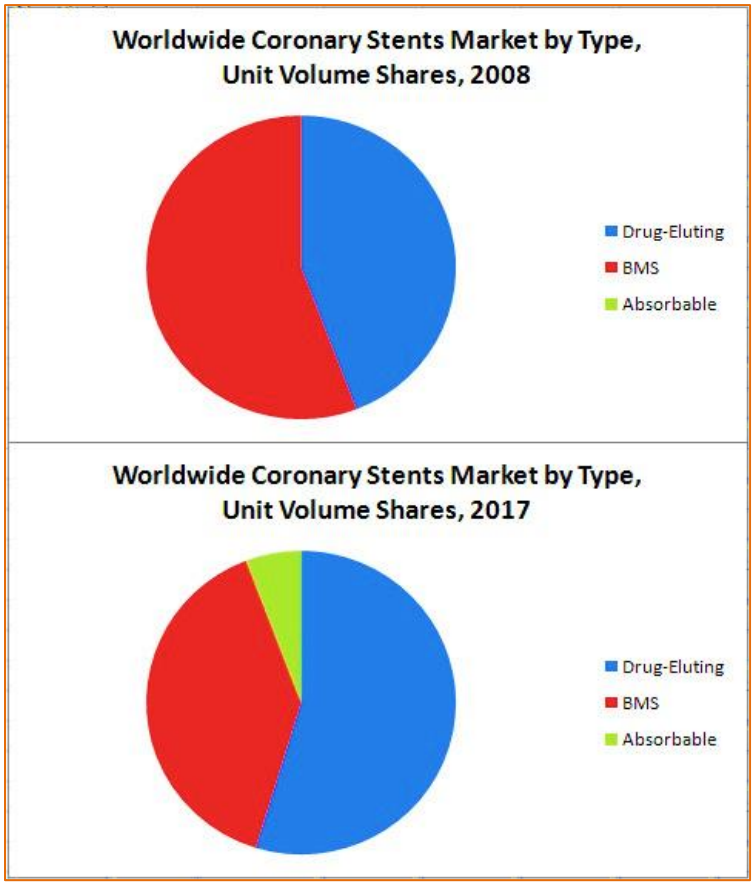


Figure 1.3: 2008 and 2017 market projection of unit volumes for the major types of coronary stents [26]

### 1.7 Types of Biodegradable Stents

Currently, both metallic and polymeric materials are utilized for manufacturing biodegradable stents. Biodegradable polymeric stents have the potential to serve as both local drug delivery systems [27-29] as well as to provide a physical barrier to the vessel wall thus preventing thrombus formation and intimal proliferation. These polymer stents have a limited mechanical performance and a recoil rate of approximately 20 percent and therefore, require thicker struts than their metallic counterparts that impede their profile and delivery capabilities, especially in small vessels [27-30]. Figure 1.4 shows the first absorbable stent implanted in humans. It was constructed from poly-L-lactic acid

(PLLA). In the absorption process, hydrolysis of bonds between repeating lactide units produced lactic acid that entered the Krebs/citric acid cycle (a series of chemical reactions used by all aerobic organisms to generate energy through the oxidation of acetate derived from carbohydrates, fats and proteins into carbon dioxide and chemical energy in the form of adenosine triphosphate (ATP)) and is metabolized to carbon dioxide and water [24].

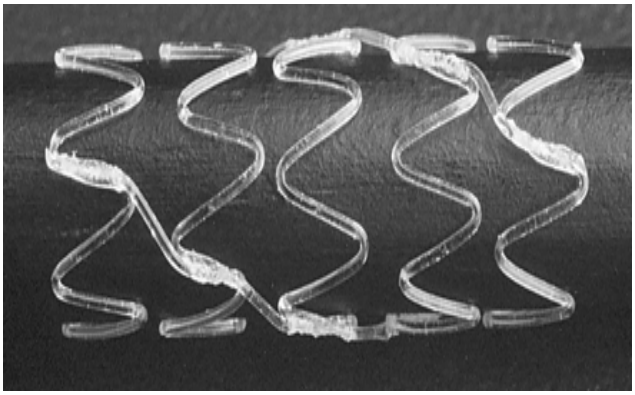

Figure 1.4: The expanded Igaki-Tamai bioabsorbable stent constructed from poly-L-lactic acid with zig-zag helical coil design and straight bridges of strut thickness 170 μm [24]

Metal biodegradable stents are intuitively attractive since they have the potential to perform comparatively with those manufactured from currently used alloys such as stainless steel. Alloys of magnesium and iron have exhibited better biocompatibility and mechanical properties for stent applications as compared to that of polymers [31]. However, less emphasis has been placed on the usage of iron as a biodegradable material [32] [33, 34] due to its slow degradation rate and toxicity when used in excess. On the other hand, magnesium alloys are more attractive because of their low thrombogenicity and well-known biocompatibility [35].

### 1.8 Advantages of Magnesium in Stent Technology

The first metallic bio-absorbable stent implanted in humans was the magnesium alloy stent studied in the Clinical Performance and Angiographic Results of Coronary Stenting with Absorbable Metal Stents trial [24]. Magnesium is an essential trace element that is non-carcinogenic [36] with a systemic toxicity of approximately 7 to 10 millimols per liter of serum [37]. $Mg^{2+}$ is also an important bivalent ion and a vital element involved in many metabolic and biological mechanisms [38, 39]. Additionally, magnesium alloy's low density, high specific strength, and excellent castability render them as appealing materials for stent applications [40]. An Mg alloy designed for cardiovascular stents should maintain its mechanical integrity for 3-6 months with mechanical properties such as, tensile yield strength (TYS) > 200 Mpa, ultimate tensile strength (UTS) > 300 MPa and tensile elongation > 15 - 18 percent. These mechanical properties are comparable to that of the most common implant materials 316 SS (TYS - 340 MPa, UTS - 670 MPa and tensile elongation – 48 percent) [41]; and with cobalt-chrome (TYS - 500 MPa, UTS - 1000 MPa and tensile elongation – 50 percent) [41]. The essential requirements for manufacturing biodegradable magnesium stents are described in Table 1.3.

Table 1.3: Primary manufacturing requirements for biodegradable Mg stents [42]

| Aspect | Description |
|---|---|
| Resorption | Mechanical integrity 3 to 6 months [43]<br>Full dissolution within 1 to 2 years [43] |
| Biocompatibility | Non-toxic, no inflammatory tissue response [43]<br>No harmful release and/or residence of particles [43] |
| Mechanical Properties | Tensile yield stress TYS > 200 Mpa [43]<br>Ultimate strength UTS > 300 MPa |

| | |
|---|---|
| | Tensile elongation > 15 - 18 % |
| Microstructure | Maximum grain size of 10 - 12.5 µm [44] |
| Hydrogen Evolution | Evolution < 10 µL $H^2$ $cm^{-2}$ $day^{-1}$ [38] |
| Corrosion Rate | Corrosion rate < 0.2 mm/year [45] |

Figure 1.4 exhibits the first biodegradable stent developed by Biotronik Company in Germany [24] that was laser cut from tubular magnesium and had sinusoidal in-phase hoops linked by straight bridges. It was balloon expandable with strut thickness of 165 µm. The coverage of arterial wall by the expanded stent was similar to that of conventional metallic stents (10 percent) [46] and the radial strength at implantation was similar to that of stainless steel stents [47]. Absorption occurred by surface erosion, such that the strut thickness decreased as the stent was absorbed. Clinical performance and angiographic imagery revealed that the implantation of the magnesium alloy stent in 63 patients resulted in no deaths, myocardial infarctions (heart attack), nor stent thrombosis, and the stent was no longer detectable by intravascular ultrasound (IVUS) after 2 months.

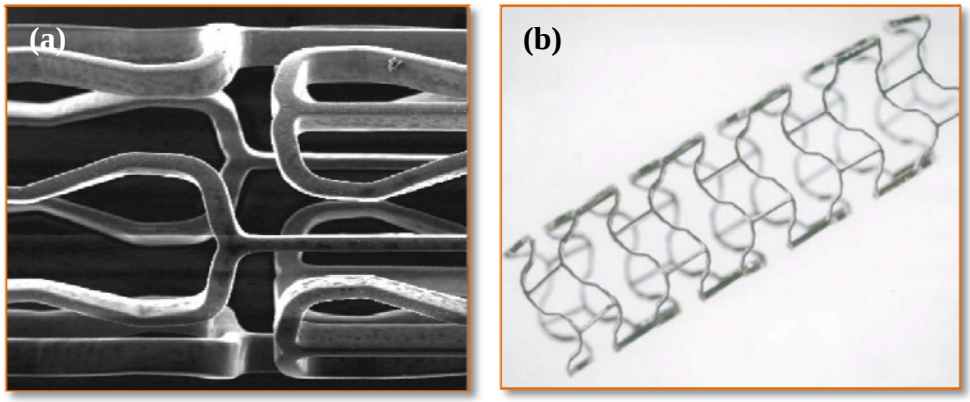


Figure 1.4: Biodegradable magnesium alloy stent developed by Biotronik Company (a) unexpanded and (b) expanded at different magnification [24]

## 1.9 Limitations of Magnesium in Stent Technology

Magnesium and its alloys offer a potential alternative to currently dominant metallic biomaterials (e.g. stainless steel, Nitinol, and cobalt-chrome alloys) for stent applications. However, their use as an implant is seriously limited due to their poor corrosion resistance in the physiological solutions. When magnesium with a purity of 99.9 percent is immersed in body simulating fluids, the pH of the solution increases from 7.4-7.6 to 10.5 [48] due to the release of hydroxyl ions as described in section 5.2, and the metal loses its mechanical integrity. Utilization of pure magnesium is therefore impractical because it dissolves before proper healing of the artery is achieved. Additionally, the increase in pH of the solution is accompanied by hydrogen evolution. Hence, a suitable degradation rate is the main determinant for future application of magnesium alloys for stent manufacture [49]. As shown in Figure 1.5, an optimal biodegradable stent should initially have a slow degradation rate (where the radial strength is maintained for 3-6 months) that ensures good mechanical integrity as well as biocompatibility, and delay the formation of degradation products. After this stage, the implant should degrade over time for 6 to 12 months as the tissue heals.

## 1.10 Solution to the Problem

There are generally two possible approaches to improve the corrosion resistance of magnesium:

1) Tailor the composition and microstructure including the grain size [50, 51] and texture [52] of the base material, through alloying [53];

2) Perform surface treatments or apply coatings [54], which produce protective ceramic/polymer/composite layers.

### 1.10.1 Alloying

Numerous attempts have been made to develop novel magnesium alloys for biomedical applications [35, 55-57], most of which contained aluminum (Al) and/or rare earth (RE) elements. Aluminum exposure has been reported to result in motor neuron degeneration, and is associated with dementia and Alzheimer's disease [58]. Furthermore, after administration of high amounts of RE elements, severe hepatotoxicity has been reported [59-61]. Therefore, biocompatible elements such as zinc and calcium have been suggested as alloying elements in order to retard magnesium's rapid rate of degradation [62]. Zinc and calcium are considered potential metals of alloying with magnesium as they are essential elements in the body and also play a prominent role in retarding the corrosion of magnesium [45].

**Zinc:** Zinc is one of the most abundant nutritionally essential elements in the human body. It accelerates the metabolism of cells. Typically, both zinc and magnesium displace hydrogen ions from aqueous solution in accordance to the following equations.

$$Mg\,(s) + 2\,H^{+}\,(aq) \rightarrow H_2\,(g) + Mg^{2+}\,(aq) \qquad (1.1)$$

$$Zn\,(s) + 2\,H^{+}\,(aq) \rightarrow H_2\,(g) + Zn^{2+}\,(aq) \qquad (1.2)$$

However, the addition of zinc to magnesium has been reported to decrease hydrogen evolution from the surface of the alloy during corrosion testing [63]. A metal can displace metal ions listed below it in the activity series, but not above. Therefore, when zinc is alloyed with magnesium which is more electropositive, it displaces zinc ions

in solution according to equation (3). This reaction competes with that of equation (1.1) which results in less hydrogen evolution.

$$Mg(s) + Zn^{2+}(aq) \rightarrow Zn(s) + Mg^{2+}(aq) \quad (1.3)$$

**Calcium:** Calcium is also one of the most nutritionally essential elements required in human metabolism. It provides the foundation for healthy teeth and bones helps in the development of muscle tissues and regulates blood pressure. It has been reported that the addition of calcium to magnesium effectively refined the grain size of the alloy [64]. Huntsman et al. reported that magnesium ($Mg^{2+}$) in the presence of calcium ions ($Ca^{2+}$), play a significant role in catalyzing the clotting of blood [65]. Optimum concentrations of Ca:Mg in blood serum have been shown to prolong blood clotting time [65].

### 1.10.2 Surface Modification

Since alloying alone does not provide sufficient corrosion resistance for the highly reactive magnesium during the initial implantation stage, attempts have been made to protect the surface by surface modification, either by surface treatment and/or surface coating. In the initial phase of implantation, a controlled degradation rate is desirable because the major criterion during that period is the strength of the stent to provide sufficient arterial support [66].

#### 1.10.2.1 Surface Treatment

Various surface treatments can be applied to retard corrosion of magnesium alloys and at the same time improve adhesion between a coating and the material's surface. Surface treatments such as acid etching [67], laser surface treatment [68], ion implantation [69] and anodization [70, 71] have been utilized for these purposes. In this

investigation, acid etching and anodization were adopted. Acid etching is described in section 2.2.2 and anodization is described in section 2.2.3.

#### 1.10.2.2 Surface Coating

In an effort to further provide protection against high initial degradation rates of magnesium alloys, specific coating techniques have been introduced [63, 72, 73]. As the corrosion of a metal surface is an electrochemical reaction between the metal and external agents (for example, oxygen and/or water), a surface coating can act as a barrier in preventing this reaction. Many studies on surface coatings revealed that organic coatings can enhance corrosion resistance of magnesium alloys. An ideal surface coating on biodegradable magnesium alloys should not only provide acceptable corrosion resistance, but also should promote bioactivity. A biodegradable polymer coating is a viable option [29–31] as it not only alters the degradation rate of magnesium, but also provides superior biocompatibility and biostability, thromoboresistance, antimicrobial action and dielectric strength [63, 72, 73]. Currently, many biodegradable polymers, such as poly (l-lactic acid) (PLLA), poly (caprolactone) (PCL), poly (lactic acid) (PLA) and poly (glycolic acid) (PGA) have been approved for cardiovascular applications [29–31] [74].

### 1.11 Research Objectives:

The current research focuses on the development of a polymer coated (PC) biodegradable magnesium alloy Mg-Zn-Ca (MZC) that has low degradation rate and is conducive to endothelialization with reduced thrombogenicity.

The following are the specific tasks of the current research:

1. Manufacture biodegradable PC MZC alloy.
2. Determine surface energy, morphology, surface chemistry of the bare metal sample (BM) and polymer coated sample via contact angle meter, scanning electron microscopy (SEM)/ energy dispersive spectroscopy (EDS), attenuated total reflectance fourier transform infrared spectroscopy (ATR- FTIR) and X-ray photoelectron spectroscopy (XPS).
3. Determine polymer/substrate adhesion strength using micro scratch tester and mechanical integrity via tensile testing with prolonged period of immersion time.
4. Determine *in-vitro* corrosion rates, polymer coating stability and hydrogen evolution via potentiodynamic polarization, electrochemical impedance spectroscopy (EIS) and immersion tests, respectively.
5. Assess biocompatibility and hemocompatibility via endothelial cell growth and *in-vitro* platelet adhesion studies on PC and bare MZC surfaces.

## 1.12 Research Significance

It is envisaged that the usage of biodegradable alloys and coatings for the manufacture of stents will obviate the need for repeat surgical procedures. Biodegradable magnesium alloys are composed of alloying elements that are essential in human metabolic and healing processes. The biocompatibility and corrosion rate of the MZC alloy are dependent on basic surface characteristics, such as elemental composition, nature and thickness of the oxide/polymer layer, surface morphology, surface charge and wettability that are modified by surface treatments and polymer coating. In this research,

strengthening of the magnesium alloy is achieved by incorporating primarily zinc [38] as well as calcium, thus enhancing corrosion resistance and mechanical properties of the MZC alloy [39, 40]. Furthermore, the application of a hydrophobic biodegradable co-polymer coating (poly glycolide-co-caprolactone (10:90)) is expected to delay the initial degradation rate of MZC. This co-polymer has been reported to be biocompatible with minimal acute inflammatory reaction of tissue [42].

# 2. LITERATURE REVIEW

As a part of this research, available literature that focused on the development of magnesium based alloys for cardio vascular applications has been reviewed. The selection of the magnesium alloy MZC [39, 40] [75] and the co-polymer PGCL for surface coating [42][76] was based on the recommendations provided by different studies. This section summarizes the findings and recommendations regarding the selection of these materials.

## 2.1 Alloy Selection

As discussed in the chapter 1, magnesium is one of the most suitable candidates for bio-absorbable stent application because of its degradation behavior and its assimilation in the human body. Unfortunately, pure magnesium has a very high corrosion rate (407 mm/year) and poor mechanical properties (yield strength and ultimate tensile strength) for stent applications [77]. However, the corrosion rate and mechanical properties of magnesium can be effectively improved by the appropriate addition of alloying elements [78] such as zinc and calcium. This has prompted a significant amount of research on the development of biodegradable alloys consisting mainly of magnesium in combination with other potential elements in various compositions [35, 55-57]. Numerous attempts have been devoted to explore novel magnesium alloys that have minimal toxicity [35, 55-57] and studies have shown that alloying with excessive concentrations of certain elements such as iron (Fe) results in acute toxicity and even death [79]; manganese induces neurotoxicity [74]; aluminum is induces degeneration of motor neurons causing dementia and Alzheimer's disease; whereas rare earth elements have been reported to

cause severe hepatotoxicity (chemical-driven liver damage) [59, 61, 80]. Therefore, the biocompatible elements, zinc and calcium [48, 74, 81-89] were used as alloying elements in an effort to impart corrosion resistance and retard magnesium degradation [62].

Calcium is a major component in human bone and is essential for chemical signaling in cells [81, 87]. But the alloyed Mg-Ca during degradation has high hydrogen release, which reduces cell viability [26, 37] and may also result in serious hemolysis (~ 66 percent) [33]. Hydrogen gas is released when $Mg^{2+}$ and $Ca^{2+}$ ions are released during degradation due to which there is an increase in the pH of the electrolyte from 7.5 to 10.0. To resolve this issue of pH increase, zinc which plays an effective role in reducing the hydrogen evolution (discussed in section 1.10.1) was used. Moreover, zinc is biocompatible as it is an essential element in the human body (component of many proteins) [85, 86] and it accelerates the metabolism of cells. Previous investigations demonstrated that magnesium alloyed with zinc and calcium exhibited excellent corrosion resistance [75] [90] degrades with a release of $Mg^{2+}$, $Zn^{2+}$ and $Ca^{2+}$ ions. These ions produce a passive layer comprised of calcium and magnesium phosphates and magnesium oxide which retard the corrosion rate of magnesium [64].

It was speculated that Mg-Zn-Ca alloys with a proper zinc and calcium content can exhibit a superior combination of mechanical properties, corrosion resistance and biocompatibility. For example, Huntsman et al. reported that $Mg^{2+}$ and $Ca^{2+}$ ions help in prolonging the blood clotting time [65] and reported an optimum amount of $Ca^{2+}$ that efficiently acts as a catalyst in the clotting of blood which prolongs thrombosis:

$$Ca^{2+} \leftrightarrow Mg^{2+} \rightarrow \text{clotting molecules} \rightarrow \text{prolongs thrombosis}$$

Figure 2.1 [65] depicts the optimal concentration (2:1) of $Mg^{2+}$ to $Ca^{2+}$ ions as a function of clotting time of human plasma. Gill et.al was able to obtain this optimum ion concentration when calcium weight percentage was maintained at 1 [91]. However, in casting of the alloy, a calcium concentration above one weight percent could be problematic due to hot tearing or sticking on the walls of vessels [92].

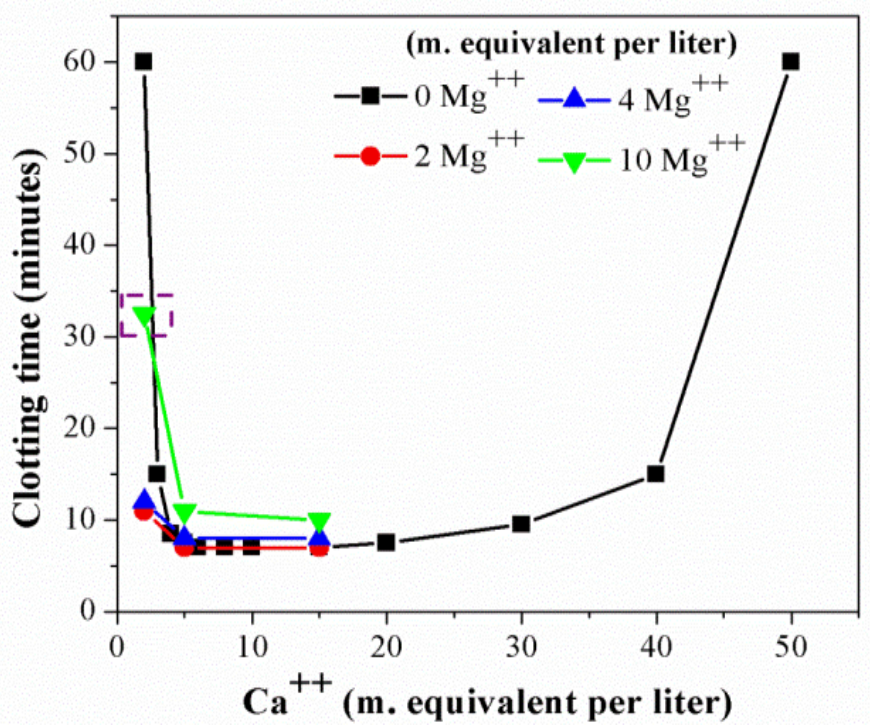


Figure 2.1: $Ca^{2+}$ and $Mg^{2+}$ concentration as a function of clotting time of human plasma [65].

Many researchers have worked on analyzing the optimum composition of zinc and calcium for improving the corrosion resistance of magnesium [75, 87, 90, 93]. Corrosion rates of various compositions of magnesium alloyed with zinc and calcium are mentioned in Table 2.1. The corrosion rates of these alloys were obtained after conducting potentiodynamic polarization or immersion tests in simulated body fluid (SBF). With one weight percent of zinc and less than one weight percent of calcium, Sun et al. obtained an

improved corrosion resistance of 0.11 mm/yr [75] whereas pure magnesium alloy has a corrosion rate of 407 mm/yr [77].

Table 2.1: Corrosion properties of pure magnesium and magnesium alloys

| Magnesium alloy | Electrolyte | Type of Measurement | In vitro corrosion rate (mm/year) | Refs. |
|---|---|---|---|---|
| Pure Mg (as-cast) | SBF | Electrochemical test | 407 | [77] |
| Pure Mg | SBF | Immersion test | 30 Days - 2.13 | [75] |
| Mg–4Zn–0.2Ca (as-cast) | | | 30 Days - 2.05 | |
| Mg–4Zn–0.2Ca (extruded) | | | 30 Days - 1.98 | |
| Mg-Zn-0.2Ca (Extruded) | SBF | Immersion test | 3.23 | |
| Mg-Zn-0.5Ca (Extruded) | | | 0.18 | |
| Mg-Zn-0.8Ca (Extruded) | | | 0.11 | |
| Mg–6Zn | SBF | Electrochemical test | 0.16 | [93] |
| | | Immersion test | 30 Days - 0.07 ± 0.02 | |
| Mg-1Ca (as-cast) | SBF | Electrochemical test | 12.56 | [87] |
| Mg-2Ca (as-cast) | | | 12.98 | |
| Mg-3Ca (as-cast) | | | 25.00 | |
| Mg-1Ca (as-rolled) | | | 1.63 | |
| Mg-1Ca (as-extruded) | | | 1.74 | |
| Mg–0.5Ca | Kokubo's SBF | Electrochemical test | 4.2 ± 0.24 | [90] |
| Mg–0.5Ca–1Zn | | | 4 ± 0.31 | |
| Mg–0.5Ca–3Zn | | | 5.3 ± 0.38 | |
| Mg–0.5Ca–9Zn | | | 10.6 ± 0.37 | |
| Mg–0.5Ca | | Immersion test | 14 Days - 1.85 | |
| Mg–0.5Ca–1Zn | | | 14 Days - 1.23 | |
| Mg–0.5Ca–3Zn | | | 14 Days - 1.80 | |

Considering the corrosion rates of magnesium alloys in Table 2.1 at various compositions of alloying elements (zinc and calcium) and considering the Ca:Mg ratio of Gill et al., the optimum magnesium alloy composition in the current research was selected to be Mg-1Zn-1Ca [92].

As discussed in section (1.10.2), alloying alone cannot provide protection against corrosion of magnesium implants during the initial implantation stage. Therefore, specific coating techniques have been applied to MZC to decrease the contact of metal with the biological environment and to control the degradation rate [54].

## 2.2 Surface Treatments

Generally before coating, an appropriate treatment process is required to effectively clean and activate the surface of the Mg alloy. This process produces a clean, dry and contaminant free surface capable of providing the maximum possible adhesive strength between the polymer coating and alloy surface. Surface treatment is therefore a very important step for the application of corrosion protective coatings since it has influence on the coating formation process, adhesion and impurities concentration on the alloy surface [94, 95]. Moreover, due to high surface alkalinity of Mg alloys, surface treatments prior to the application of an organic coating are necessary [96].

There are surface treatments to remove the contaminants or oxides on the top layer and there are others by which the oxide composition can be altered. Commonly used treatments include, acid etching and anodization, which is a chemical conversion coating. Anodization has been utilized in recent years to replace the existing oxide layer of magnesium alloys with a new and denser protective oxide layer.

## 2.3 Mechanical Polishing

Mechanical polishing (MP) is commonly used to remove impurities such as dirt and burred edges from magnesium sample surface [131] and is normally performed prior to acid etching and anodizing. The selection of MP depends on the type of material and the

specific surface characteristics required. MP requires the usage of silicon carbide (SiC) grit papers and diamond paste which changes the surface roughness of the sample. Coarse polished finishes, with roughness > 1 micron exhibited deep grooves where chloride ions can accumulate and initiate corrosion [132, 133]. In contrast, fine polished finishes with roughness < 0.5 micron exhibited smooth surface, with fewer sites for chloride ions attack. Honess et al. observed that the optimum surface roughness for corrosion resistance of MZC was 0.5 microns [132]. Anodization and acid etching should be performed immediately after conducting MP in order to limit oxide formation on the surface.

### 2.4 Acid Etching

Acid etching (AE) of magnesium alloys has been widely adopted [100] [101] to remove residual surface oxide/hydroxide layer and to create a new equipotentialized surface. The removal of Mg-oxides necessitates the usage of solutions that are neutral or acidic. Typical acid baths comprise chromic, nitric or sulphuric acids. Furthermore, surface roughness of the substrates can be noticeably increased by acid treatment [97]. Surface roughness of a substrate plays a critical role in determining the resulting coating qualities such as coating porosity, deposition rate and adhesion. Suitable surface roughness is essential for coating adhesion, owing to enhanced interlocking [97, 98]. Lui et al. proposed that the rougher the surface, the higher the deposition rate, which was attributed to more nucleation sites on the rougher surface [97] and beyond a certain level roughness, the porosity within the coating was not acceptable.

Etching provides surface pits which act as sites for mechanical interlocking to improve adhesion between the polymer coating and the magnesium alloy [52]. Gray-Munro [102] observed that acid etched AZ31 (Mg-3Al-1Zn) in simulated body fluid (SBF) solution produced a homogenous and dense films of $Mg_3(PO_4)_2$ coatings, which retarded corrosion of the alloy. Turhan et al. [103] reported that the corrosion resistance of AZ91D (Mg-9Al-1Zn) alloys could be greatly enhanced through the treatment of 2.5 percent sulphuric acid ($H_2SO_4$) solution. The distribution of α and β phases in magnesium alloys changed with increasing etching time and led to the increase of both $R_{ct}$ and faradaic inductance [103]. The impedance results of Zomorodian et al. evidenced that the polyether imide (PEI) coatings after acid etching with hydrofluoric acid (HF) provided good barrier properties to protect magnesium alloy for more than 3 months [100]. With poly (caprolactone) (PCL) as polymer coating and HF treated magnesium alloy, the increased formation of magnesium hydroxide ($Mg(OH)_2$) inhibited the corrosion rate for more than 2 months [101].This increase of corrosion resistance in different acid etched alloys was due to the interfacial interaction for better adhesion between the polymer and magnesium substrate.

### 2.4.1 Anodization

Anodization is a novel technique that had proven its efficacy in retarding corrosion of magnesium alloys [104]. It is an electrochemical process that mainly develops a passivation oxide layer, which is corrosion resistant in aqueous solutions. The oxide layer formed during anodization is stable, whereas the oxide layer formed due to atmospheric corrosion is thick and unstable in aqueous solutions [105-107]. The composition of the

oxide layer is complex and generally consists of two layers with thicknesses ranging from 10 to 50 μm [108], where the inner layer is thin and dense and the outer layer is thick and porous, usually requiring a sealing treatment. Anodized coating is hard (wear resistant) and porous (similar to bone microstructure) when compared to other conversions or fluoridated coatings [37]. The firmness of the surface oxide layer directly affects the biocompatibility of the implant as it acts as a barrier between the implant material and the electrolyte, which further confines to ion exchange and increases the implant stability [109]. Another advantage of anodization is that it can offer a very effective protection to magnesium implants during healing of the surgery area and the coating will break down after the surgery area is healed, thus enabling the implant to be dissolved gradually. Zhang et al. studied the corrosion response of anodized AZ91 in a 3 percent NaCl solution. The anodized AZ91 presented better impedance response comparatively to the untreated sample [108]. The anticorrosion mechanism of the anodized film covered with maleic anhydride-g-liquid polybutadiene (MALPB) was found to be associated with the barrier capability of slowing down the infiltration of the electrolyte inside the protective coatings composed of different layers; and the compact layer exhibited much more effective restriction of electrolyte infiltration than others [104].

### 2.5 Surface Coatings

Surface coatings for stent applications should possess good biocompatibility, bioactivity and antibiotic or local drug delivery capability. Additionally, these coatings should have a slow biodegradation rate so that they can potentially delay the corrosion of the MZC alloy and maintain its mechanical integrity over a longer timeframe. Generally,

coatings can be divided into two classes: conversion coatings and deposited coatings. Conversion coatings are in situ grown coatings which are oxides formed by the chemical or electrochemical reactions between the metal and the surrounding environment [99]. The produced layers are inorganic and show ceramic like character. Deposited coatings are formed by depositing thin films onto metal surfaces. Different deposition coating mechanisms such as PEO coatings [100], plating processes [54] and polymeric coatings [101-104] for corrosion protection of magnesium alloys are described in the literature. The conversion coatings that have ceramic nature are frequently used to reduce corrosion rate of magnesium in orthopedic implantation. Unfortunately, their usage is not suitable for cardiovascular stent applications because ceramics are not ductile enough to enable plastic deformation during expansion of the stents.

Biodegradable polymer coatings which not only possess better ductility but also render corrosion resistance are promising for stent applications [101-104] especially since anti-restenotic drugs can be incorporated in the polymer. This has led to the emergence of drug-eluting biodegradable stents [105].

### 2.6 Polymer Coatings

Polymer coatings that are thin and adherent to the magnesium surface have been utilized to effectively retard the corrosion rate of implants [101-104] with improved biocompatibility, performance and therapeutic effectiveness [72] [95] [106]. The selection of an appropriate polymer coating is crucial in determining the biocompatibility of the implant as the interface between its surface and the environment is critical in soliciting the appropriate immunological response [107]. A suitable polymer should

provide slow biodegradation that can potentially delay the corrosion of magnesium implant in order to maintain the latter mechanical integrity over a longer timeframe.

There are two kinds of polymers: permanent and biodegradable. Permanent polymers such as poly (ethylene-co-vinyl acetate), poly (n-butyl methacrylate) and poly (styrene-b-isobutylene-b-styrene) have been used as protective stent coatings by companies such as Cordis® and Boston Scientific®. Even though these permanent polymer coatings imparted good corrosion resistance, the presence of their debris in the vessel arterial wall influenced local responses and altered the processes involved in neointimal formation which provoked inflammatory responses in the body [108, 109] that increased beyond the first year of implantation.

The use of biodegradable polymers, as opposed to permanent polymers, in coronary stent technology has the advantages of a complete elution of drugs and reduced inflammatory response, with the potential for decreasing the risk of late complications such as stent strut uncovering, mal-apposition, endothelial dysfunction and thrombosis [110-115]. Biodegradable polymers can either be natural or synthetic. In general, synthetic polymers offer greater advantages than natural polymers and can be tailored to provide a wider range of properties [116]. Commonly used biodegradable polymers along with their selected physical and chemical characteristics, are listed in Table 2.2. These polymers have unique features such as controllability of mechanical properties, tailoring of degradation rates, and minimal toxicity and immune response that make them ideal for medical uses. As shown in the table 2.2, the co-polymer PLA/PGA (50/50) exhibits a degradation rate between 1-2 months which lies within the range required for bio-absorbable magnesium stent applications.

Table 2.2: Mechanical properties and degradation rates of synthetic biodegradable polymers [117, 118]

| Name | Degradation Time (months) | Tensile Strength (Mpa) | Tensile Elongation | Elastic Modulus (Gpa) |
|---|---|---|---|---|
| PLA* | 12-16 | 21-60 | 2.5-6 | 0.35-3.5 |
| PLLA* | >24 | 3-10 | 3-10 | 2.7-4.14 |
| PDLA* | 6-12 | 2-10 | 2-10 | 1.0-3.45 |
| PGA* | 6-12 | 1.5-20 | 1.5-20 | 6.0-7.0 |
| PCL* | >24 | 20.7-42 | 3000-1000 | 0.21-0.44 |
| PLA/PGA (50:50) | 1-2 | 2-10 | 2-10 | 1.0-4.34 |

*PLA - Poly (lactic acid), PLLA - Poly (l-lactic acid), PDLA – poly(D-lactide), PGA - Poly (glycolic acid), PCL - Poly (caprolactone)

Most commonly used polymers in stents applications have good biocompatibility and degrade by hydrolysis of the ester links followed by fragmentation and release of acids and oligomers that are nontoxic and can be absorbed or excreted during metabolism [119]. However, the tensile strength of these polymers is 1-2 orders magnitude less than that of metals.

Many researchers have utilized biodegradable polymer coatings to improve corrosion resistance of magnesium alloys [72] [106] [120] [121] (Table 2.3) and have reported a complicated corrosion mechanism that is dependent on the kind of polymer, its molecular weight, coating properties and corrosion environment. Table 2.3 exhibits that the dip coating technique is widely used to polymer coat magnesium alloys as compared with other techniques such as spin coating, spray coating, electro spinning and evaporation. It should be noted that corrosion rates of the magnesium alloys was dependent on coating thickness, porosity and molecular weight of the polymer. For example a thin coating of <

30 µm provided better corrosion resistance than the coatings of > 30 µm [120] [102, 103, 120]. This is attributed to the fact that trapped hydrogen gas underneath the thick polymers lead to swelling, deformation, and delamination of the polymer from the alloy surface [102]. Thus, thick polymer coatings can only initially provide partial protection to the alloy surface.

Table 2.3: Corrosion properties of various polymer coated magnesium alloys

| Mg Alloy (Wt%) | Surface Treatment | Polymer Mol Wt (g/mol) | Technique | Coating thickness (µm) | Corrosion rate | Electrolyte | Ref |
|---|---|---|---|---|---|---|---|
| Mg (99.95%) | MP** (9 µ) | PLLA* (50000) PLLA* (80000-10000) | Spin Coating | 0.34 0.97 | Immersion (10 days) 2.3 µm/day 1.63 µm/day | DMEM | [120] |
| | | PCL* (40000) PCL* (70000-10000) | Spin Coating | 0.30 0.93 | Immersion (10 days) 3.85 µm/day 3.15 µm/day | | |
| Mg-9Al-1Zn | MP** | PCL* (80,000) | Spray Coating | - | $E_{corr}$ High porosity: – 1.1 V Low porosity: – 1.4 V Immersion (2 months) High porosity - 6.22 mg Low porosity - 3.59 mg | SBF | [72] |
| AZ31B | Anodization | MALPB* (1020) | Dip Coating | 10 | $E_{corr}$: -1.19 V | 3.5% NaCl | [95] |
| AZ31 | Acid etching | PEI* | Dip Coating | 4 | $R_{ct}$: $1*10^6$ Ω $cm^2$ $4*10^4$ Ω $cm^2$ (after 80 days) | Hanks solution | [106] |
| AZ31 | MP** (5 µ) | PLGA* 50:50 (30,000-60,000) | Dip Coating | - | $E_{corr}$: -1.52 V | DMEM | [121] |
| | | PLGA* 75:25 (76,000-115,000) | | | $E_{corr}$: -1.44 V | | |
| | | PCL* (70,000-90,000) | | | $E_{corr}$: -1.50 V | | |

| Mg Alloy (Wt%) | Surface Treatment | Polymer Mol Wt (g/mol) | Technique | Coating thickness (µm) | Corrosion rate | Electrolyte | Ref |
|---|---|---|---|---|---|---|---|
| AZ31 | MP** (5 µ) | PLGA* - 30,000–60,000 | Dip Coating | ~1.6 - 41.8 | $E_{corr}$: -1.469 V | DMEM** | [102] |
| AZ31 | Acid Etching | PVDF* | Dip Coating | 2.5<br>8<br>13 | $R_{ct}$:<br>0.3 *$10^6$ Ω $cm^2$ (after 72 h)<br>17 *$10^6$ Ω $cm^2$ (after 72 h)<br>1523*$10^6$ Ω $cm^2$ (after 72 h) | NaCl** | [101] |
| Mg-1Zn-0.2Mn | MP** (1 µ) | PTMC* - 500,000 | Evaporation | 10 | $E_{corr}$ - -1.478 V<br>$R_{ct}$ - 363.2 k Ω | SBF** | [122] |
| | | PCL* – 100,000 | | 10 µm | $E_{corr}$: -1.604 V<br>$R_{ct}$ : 69.67 k Ω | | |
| Mg-6Zn | MP** (1200 SiC) | PLGA* 90:10 (140,000) | Dip Coating | 33 – 72 | $E_{corr}$: -1.36 to -1.44 V<br>Immersion test (144 hrs): 0.0323 to 0.0562 mg/$cm^2$/h | 0.9% NaCl** | [103] |
| Mg-9Al-1Mn | MP** (1 µ) | PLA* (148,000 - 110,000) | Dip Coating | 11.1 - 13.06 | $E_{corr}$: -1.18 V<br>Immersion Test (360 h) 0.765 mg/$cm^2$ | SBF** | [104] |
| | | | Electrospining | 30.4 | $E_{corr}$: -1.32 eV<br>Immersion Test (360h) 0.58 mg/$cm^2$ | | |
| Mg-9Al-1Mn | MP** (1 µ) | PVAc* | Dip coating | 40-60 | Ecorr - −0.6814 V<br>Immersion (21 days) - 18 ± 2.7 mg | SBF** | [123] |

* PCL - Poly (caprolactone), PLA - Poly (lactic acid), PLLA - Poly (l-lactic acid), MALPB - Maleic anhydride-g-liquid polybutadiene, PEI - Polyether imide, PLGA – Poly(lactic-co-glycolic acid), PVDF - Poly Polyvinylidene difluoride, PTMC - Poly(trimethylene carbonate) and PVA - Polyvinyl acetate

** MP – Mechanical Polishing, SBF - Simulated Body Fluid, DMEM - Dulbecco's Modified Eagle Medium, NaCl – Sodium Chloride

Many researchers in an effort to provide good polymer adhesion with decreased degradation rate have reported the effectiveness of low porosity and thin coatings in retarding the degradation rate of magnesium [72] [120]. Wong et al. revealed that low

porosity poly (caprolactone) (PCL) coating was more efficient in increasing the corrosion resistance of magnesium alloy as compared with a porous PCL coating [72].

In general low molecular weight (LMW) polymers result in a thin surface coating whereas high molecular weight (HMW) polymers lead to a thicker coating. [120]. LMW polymers that are less viscous than HMW polymers are effective in penetrating through surface defects, pores, cracks etc., and therefore create better adhesion between the polymer and magnesium substrate.

In addition to the above mentioned properties, the polymer should be hydrophobic. It has been reported that a hydrophobic surface minimizes platelet adhesion [124]. However, highly hydrophobic polymers are usually non-polar which mitigates adhesion with metal substrates. In such cases, metal substrates can be functionalized to facilitate adhesion of hydrophobic polymers. The metal can be coated with other polymers that can react with one of the corrosion products ($Mg(OH)_2$) forming polymer derivatives with higher polarity that can bind to the hydrophobic polymer.

Taking into consideration all of the aforementioned characteristics such as hydrophobicity, degradation rate, molecular weight, porosity and adhesion strength a novel hydrophobic co-polymer comprising of polycaprolactone (PCL) and polyglycolic acid (PGA) in the proportion of 90:10 were chosen as the bio-absorbable polymer coating in the current research. It should be noted that this co-polymer has been approved US Food and Drug Administration (FDA) and is used in various biomedical applications [125].

PCL is more hydrophobic (a desirable property for coating of MZC) than most polymers. However, its degradation rate of two to three years (see table 2.2) is impractical for bio-absorbable stent applications which require a degradation rate of 6-12 months. On the other hand, PGA has a degradation rate of 6-12 months. Therefore, co-polymerization of PCL with PGA can be utilized to adjust the degradation rate required without sacrificing biocompatibility [126]. This PGCL co-polymer was first used by Lee et al. [76] for vascular grafting which required a degradation period of a few months. Lee et al. showed that PGCL was very elastic in nature, making it interesting to achieve a desirable compliance in tubular constructs [76].

## 2.7 Coating Techniques

Polymer coating techniques are generally simple processes that are not energy intensive. The polymeric solution can be sprayed, brushed, dropped or poured on the substrate or the substrate can be dipped into the polymer. This is followed by a drying process which produces a film of varying thickness [127, 128]. Some commonly used techniques for polymer coating are described in Table 2.4.

Table 2.4: Advantages and disadvantages of coating methods commonly used in industries

| Coating method | Advantages | Disadvantages |
|---|---|---|
| Dip-coating | Simplicity, suitable for substrates with different shapes | Thickness variation during drying |
| Spray coating | Simplicity, suitable for any kind of substrate | Poor film control, requires solution with very specific properties |
| Curtain coating | Speed and control | Break of curtain is possible, too much waste of solution |
| Spin-coating | Excellent film thickness control, very low waste of solution | Limited to flat substrates, too sensible to substrate surface roughness |

Among these techniques, the dip coating is the most suitable for laboratory studies for practical reasons. It consists of simply dipping an article in the solution, keeping it there for a specific period of time for wetting of the surface and withdrawal for drying. The main advantage of dip-coating is that it can coat the entire surface of relatively complex shapes. It also enables the control of coating thicknesses (in the range of 1-100 μm) which is accomplished by varying the viscosity of the solution [129, 130]. One disadvantage of dip coating is the non-uniformity of coating thickness along the vertical axis which occurs as a result of gravitational forces during the drying process [128, 130].

# 3. SURFACE MODIFICATION METHODS

The current research is focused on minimizing the initial corrosion rate of MZC by surface treating (acid etching and anodization) and polymer coating with PGCL. This chapter describes the methods and materials utilized for modifying the surface of the MZC alloy.

## 3.1 MZC Alloy

The MZC alloy was manufactured in an ARC furnace by ACI Alloys, Inc. where ingots were cast in a water-cooled copper mold. The MZC ingot was heat treated at 350 $^{o}$C in the furnace and then water quenched. Table 3.1 displays the nominal and analyzed compositions of the MZC alloy.

Table 3.1: Nominal and analyzed compositions of MZC in weight percentage (Wt %)

| Elements | Composition (Wt %) | |
|---|---|---|
| | Nominal | Analyzed |
| Mg | Balance | Balance |
| Zn | 1 | 0.77 |
| Ca | 1 | 1.19 |
| O | NA | 7.49 |

A schematic representation of the methods used for the sample preparation of the MZC alloy is shown in Figure 3.1.

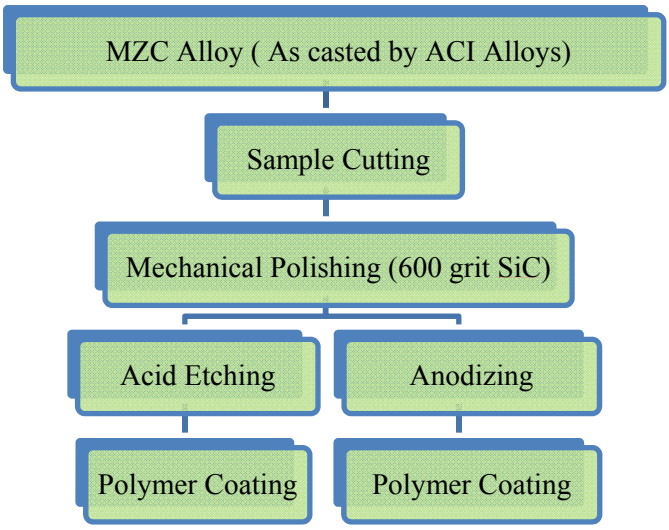


Figure 3.1: Schematic representation of MZC sample preparation

### 3.2 Sample Cutting

The MZC ingot was cut into cubes of dimensions 10.5mm x 10.5m x 2mm using a linear precision saw (ISOMET 4000).

### 3.3 Surface Treatments

In order to determine the suitable surface treatments that offer good polymer coating adhesion as well as corrosion resistance, two surface treatments: (a) acid etching and (b) anodization were adopted. Surface characteristics of acid etched and anodized samples such as surface morphology, roughness, wettability and surface chemistry were compared with those of mechanically polished samples.

### 3.4 Mechanical Polishing (MP)

Each cubed MZC alloy was subjected to mechanical polishing with 600 grit silicon carbide (SiC) abrasive paper (Buehler). This selection of 600 grit SiC abrasive paper for mechanical polishing was based on previous study designed to optimize biocompatibility

and corrosion resistance of bare metal MZC as well as PGCL coated MZC. The details of this optimization processes is described in the section entitled, “Experiments to determine optimum surface roughness in mechanical polishing” in Appendix A.

During mechanical polishing water was avoided and ethanol was used as lubricant (Sigma-Aldrich). Water based solutions were not used during sample preparation of MZC alloy in order to prevent the hydrolysis of the MZC alloy. Hydrolysis of magnesium results in the release of hydrogen gas which initiates crevice corrosion in the alloy.

### 3.5 Acid Etching (AE)

The mechanically polished samples were etched for 30 seconds at room temperature using acetic glycol etchant (water 19 mL, ethylene glycol 60 mL, acetic acid 20 mL and $HNO_3$ 1 mL). After etching, the samples were rinsed with distilled water for 30 seconds and air dried. This selection of etching time was decided based on the preliminary study conducted to optimize the corrosion resistance and hemocompatibility. The details of this optimization processes is described in the section entitled, “Optimum acid etching time selection for treating MZC sample” in Appendix B.

### 3.6 Anodization

In this study, mechanically polished samples were anodized by Electrobright® (Macungie, PA, USA). The electrolytes used during the process were organic acids and high chain alcohol. Because of the proprietary nature of the process, no further information on the electrolytes used has been disclosed by Electrobright®.

Figure 3.2 shows the typical anodizing setup, where the specimen acts as anode while the steel plate acts as the cathode [131]. In general, anodizing is high voltage

process which utilizes spark discharges to convert the magnesium surface into a ceramic oxide [70]. Technically, anodization of an alloy surface can be performed in an electrolyte via current or voltage control. In the case of voltage control, the current drops with treatment time as the insulating oxide film grows. In the case of constant current, the voltage increases with treatment time to maintain the applied current density while the oxide film grows.

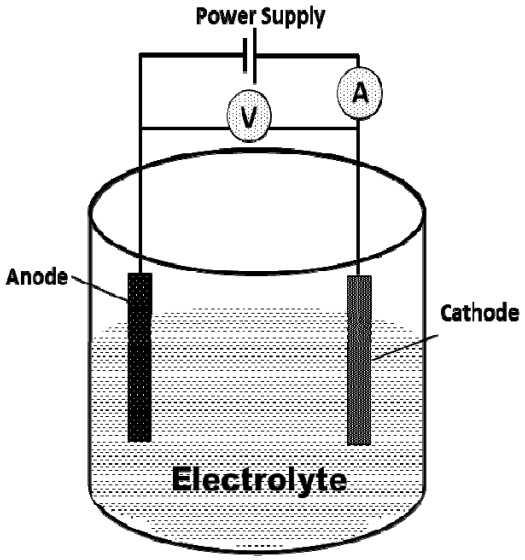


Figure 3.2: Typical anodizing setup

### 3.7 Polymer Coating

The polymer solution for coating MZC samples was prepared by dissolving PGCL in Dichloromethane (DCM) at room temperature. PGCL to Dichloromethane (DCM) concentration ratio was chosen to be 10 percent (weight by volume). Polymer coating on MZC alloy was performed by utilizing dip coating technique where samples were pre-heated at 180 °C for 10 minutes to eliminate entrapped air and moisture from the surface. Samples were dip coated in PGCL (90:10) utilizing the dip coating setup as

shown in the Figure 3.3, where the dipping and withdrawal rate was controlled using a DC motor and function generator. The samples were then immersed into the polymer solution for 20 seconds to allow wetting of the surface and were vertically dried in a vacuum oven (10 mbar) at 37 °C for 24 hours.

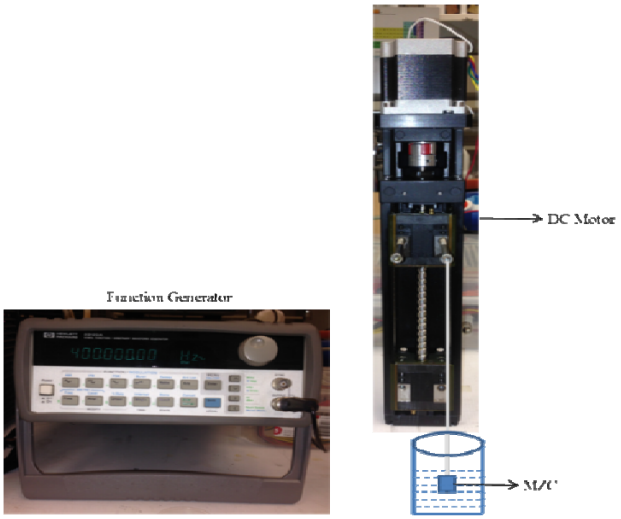


Figure 3.3: Typical dip coating setup

### 3.8 Reagents

Phosphate Buffered Saline (PBS), a reagent grade chemical conforming to the specifications of the Committee on Analytical Reagents namely, American Chemical Society, was used as the standard test solution for corrosion analysis. PBS (Sigma Aldrich) was used as an electrolyte for corrosion studies at concentrations typically found in human blood [110]. Ethyl alcohol (99.9 percent) and chromic acid were also purchased from Sigma Aldrich. MZC samples were ultrasonically cleaned in ethyl alcohol for 5 minutes, prior to conducting each test. Oxides from the samples attained were removed by immersing them in 180 g/l of chromic acid for 20 min. Table 3.2 shows the chemical composition of PBS solution with a pH of 7.2 is used in this investigation.

Table 3.2: Chemical composition of PBS solution in g/L

| NaCl | $Na_2HPO_4$ | $NaHCO_3$ | KCl | $KH_2PO_4$ | $MgSiO_4$ | $7H_2O$ | $CaCl_2$ |
|---|---|---|---|---|---|---|---|
| 8.0 | 0.06 | 0.35 | 0.4 | 0.06 | 0.2 | | 0.14 |

# 4. SURFACE CHARACTERIZATION

Surface characteristics such as surface morphology, roughness, chemistry and wettability of a material that can occur up to a few microns deep, often control their chemical and in some cases, mechanical properties. Hence, the analysis of these properties was of extreme importance because they influence coating adhesion and corrosion behavior in biological media. A schematic of surface characterization techniques that were employed in the current research is shown in Figure 4.1. The importance of each surface parameter is described in the following sections.

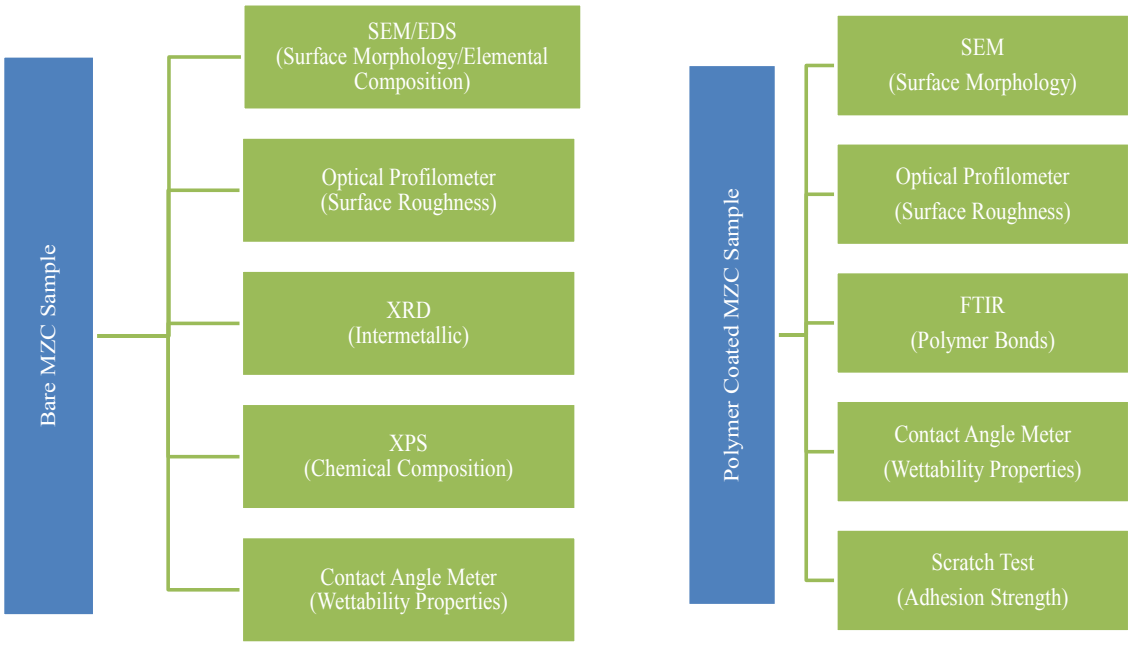


Figure 4.1: Surface characterization techniques performed in the current research

## 4.1 Surface Morphology

A scanning Electron Microscope (SEM), JEOL JSM 5900LV with an acceleration voltage ranging from 5 to 10 kV equipped with Energy Dispersive Spectrometer (EDS) was used to provide surface morphology and elemental analysis. Each MZC sample was sputter coated with gold for 2 minutes due to the presence of oxide and polymer coating.

Sputtering enhances the conductivity of non-conductive samples and prevents charging of the samples in conventional SEM mode, where high vacuum and high voltages are utilized. Charging of the surfaces of bare and PGCL coated MZC is due to the presence of lighter (low atomic number) elements such as oxygen, carbon and hydrogen. These lighter elements have very few interactions with the SEM's electron beam which yields poor contrast.

### 4.1.1 Surface Treated MZC

Figure 4.2 shows the SEM photomicrographs of surface treated MZC: mechanically polished, acid etched and anodized. The insets in Figure 4.2 are the SEM photomicrographs obtained at low voltages.

The surface of mechanically polished MZC (Figure 4.2 (a) consisted predominantly of α-magnesium phase. The inset in the Figure 4.2 (a) shows that the mechanically polished surface in addition to α- magnesium phase also revealed grain boundaries and uniformly dispersed white spherical precipitates (~ 5 μm). These two phases, predominantly α-magnesium matrix and grain boundaries were also observed by Zhang et al. in as-casted Mg-Zn alloys [85]. Additionally, the sample surface in Figure 4.2 revealed a large number of artifacts/lines that were created during mechanical polishing.

Surface etching of MZC removed the artifacts/lines created by mechanical polishing as evidenced by reduced white spherical precipitates shown in Figure 4.2 (b). Similar morphology was found by Gray et al. (2002) where acid etching of magnesium alloys removed the gross scale produced during the manufacturing process and the native oxide layer was replaced with a more passive oxide layer on magnesium alloy surface [54].

Furthermore, cracks and pores shown in Figure 4.2 (b) inset after acid etching were stress induced by continuous dissolution of metal ions from the surface of MZC.

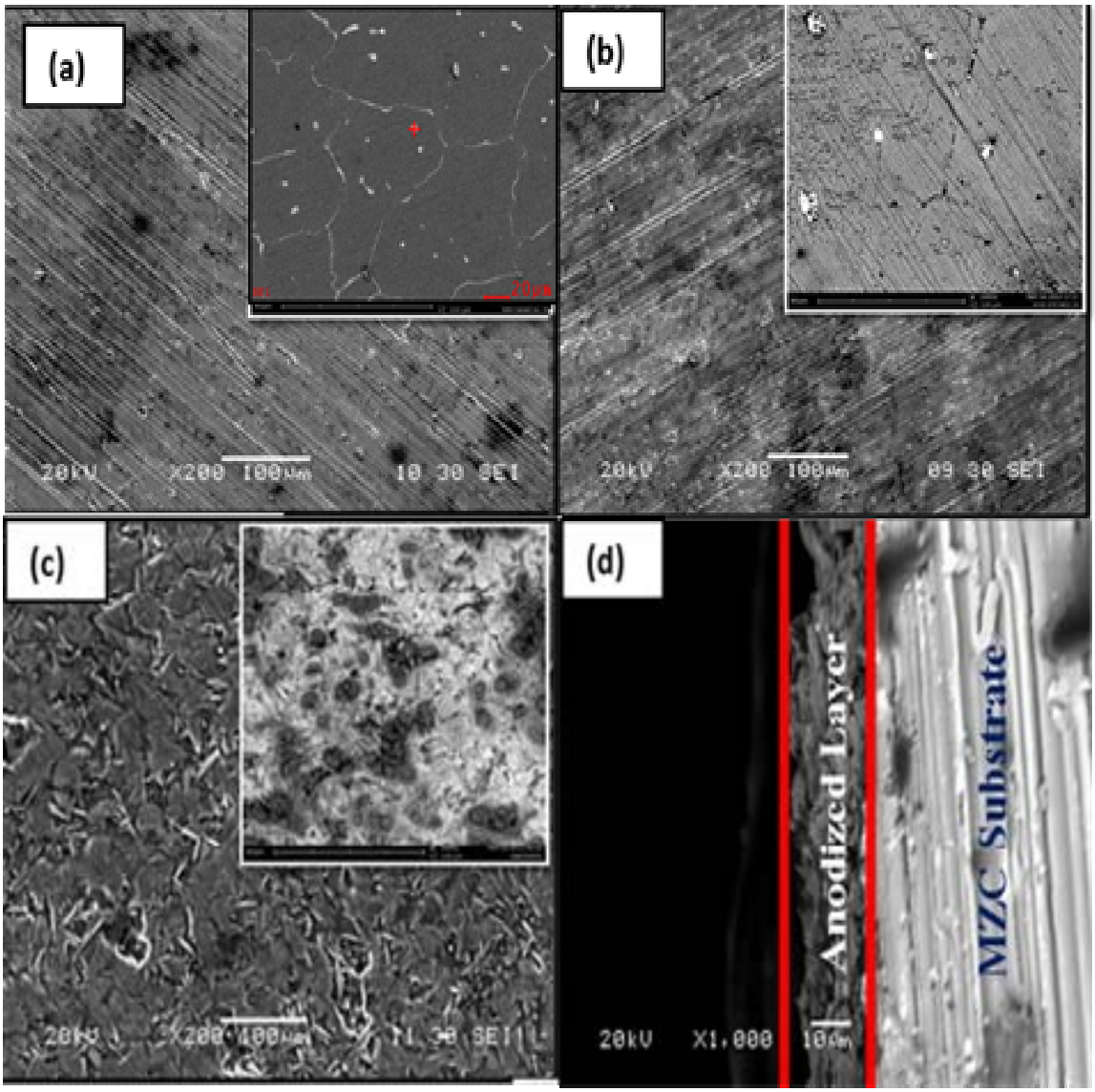


Figure 4.2: SEM photomicrographs of (a) mechanically polished (b) acid etched (c) anodized (d) cross-section of anodized MZC

The surface and cross sectional morphologies of the anodized MZC are shown in Figure 4.2 (c) and (d) respectively. Similar to the acid etched sample, the surface of anodized sample (Figure 4.2 (a)) exhibited a large number of pores and micro cracks.

Manavbasi et al. also reported the formation of an anodized film on the surface of Mg-3Al-1Zn that was uneven and had a large pore size distribution which is attributed to the spark formation on the surface of the alloy with increased current density [132]. Sparking is associated with the high temperatures that are generated in the anodic film as a result of the electrical resistance of the pores [70]. Zhu et al. reported that the micro cracks were formed due to thermal stress resulting from rapid cooling of the oxides by the electrolyte which served as a coolant [133]. Additionally, a cross sectional view of the anodized MZC revealed an oxide thickness of approximately 10 - 15 μm (Figure 4.2 (d)).

### 4.1.2 Polymer Coated MZC

Figure 4.3 (a) and (b) illustrate the surface morphology of PGCL coated MZC. Irrespective of the surface treatment employed on the MZC substrate, there was no significant difference in the morphology of the PGCL coating. An interconnected network of pores with varying diameters was produced on the surface of PGCL coated MZC. Pore phase formation occurs as a result of vapor-induced phase separation triggered by the combination of a highly volatile solvent (Dichloromethane (DCM)) and high humidity [104, 134]. The average micro-pore size was about 3.78 ± 1.66 μm. A similar network structure was reported by Zheng et al. who described polymer-poor and polymer-rich phases on the Mg alloy surface [135].

The thickness of the PGCL coating on MZC (Figure 4.3 (c)) was estimated to be < 10 microns from the cross sectional view of the SEM photomicrographs. However, the actual thickness of the PGCL coating was calculated by measuring the weight, surface

area, density of the MZC before and after PGCL coating which will be discussed in section (4.2).

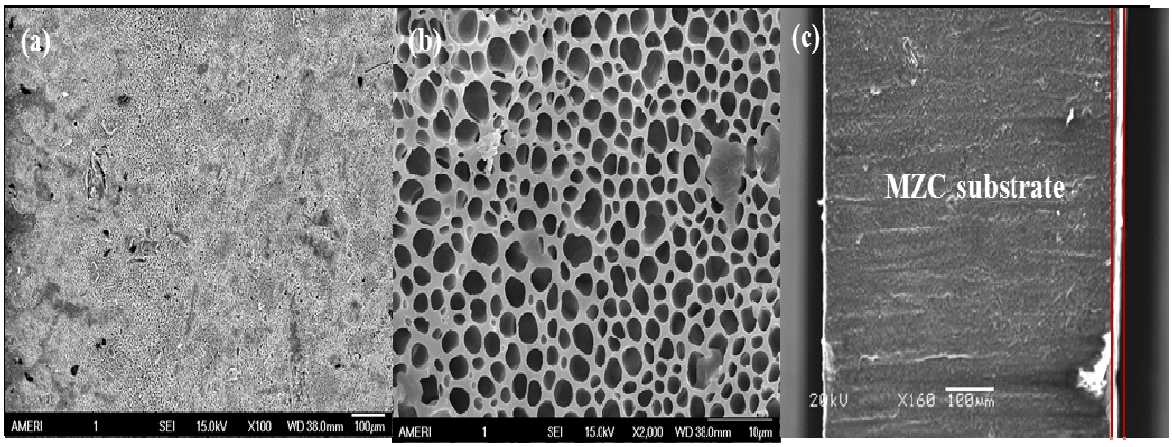


Figure 4.3: SEM photomicrographs: (a) and (b) polymer coating (c) cross sectional view

**4.2 Elemental Composition Analysis**

Energy Dispersive Spectrometer (EDS) analysis of bare MZC revealed a primary α-magnesium phase that was approximately 100% magnesium. Additionally, the alloy displayed grain boundaries and precipitates consisting of alloying elements (Zn and Ca) along with oxygen and magnesium. Grain boundary segregation of alloying elements occurred during manufacture of MZC. Initially, Zn and Ca were completely dispersed in the molten matrix but become segregated from the α-Mg phase during solidification and report to the grain boundaries and/or to precipitates on the surface of the MZC [85]. Li et al. (2008) also noticed similar α-Mg phase with grain boundaries and precipitates that has $Mg_2Ca$ phase in Mg-Ca alloy [87].

EDS analysis of acid etched MZC surface revealed low concentrations of oxygen (3.94 wt %) that was attributed to the removal of gross oxides and precipitates from the surface of MZC as is discussed in section 2.2.2.).

EDS analysis of anodized MZC revealed a higher concentration of oxygen (15.08 wt %) as compared to mechanically polished and acid etched MZC surfaces. This is to be expected, since anodization is normally employed to produce a thick and dense oxide.

Table 4.1: Elemental composition by EDS analyses of surface pretreated MZC

| Element | O | Mg | Ca | Zn |
|---|---|---|---|---|
| | Wt% | | | |
| Mechanically polished (MP) | - | 100 | - | - |
| Grain boundary and spherical particles (MP) | 5.24 | 64.24 | 16.27 | 14.25 |
| Acid etched (AE) | - | 100 | - | - |
| Spherical particles (AE) | 3.94 | 75.49 | 11.06 | 9.51 |
| Anodized coating | 15.08 | 82.59 | 1.27 | 1.07 |
| Anodized substrate | 6.85 | 68.07 | 10.99 | 14.09 |

### 4.3 Phase Analysis

X-ray Diffractometry (XRD) is a non-destructive technique used to identify and characterize microstructure phases on the surface of materials. The identification of these phases contributed to the analysis of the corrosion resistance and to a lesser extent the mechanical properties of MZC. In the current research, a Siemens 5000 D, XRD with Cu-Kα radiation (wavelength, $\lambda = 1.54$ $A^o$) operating at 35 mA and 40 kV with a scan rate of 0.01 $^o$/sec over a 2 theta from 20-90 $^o$, was used to determine the microstructure phases. A DIFFRAC$^{plus}$ EVA software (Bruker, Madison, WI, USA) was utilized to analyze the XRD spectra.

Various phases of MZC were identified as shown in the XRD spectra in Figure 4.4. The α- magnesium phase as well as stable intermetallic compounds such as $Mg_2Ca$, $CaZn_2$, $MgZn_2$ and $Ca_2Mg_6Zn_3$ were common to all surface treated samples

(mechanically polished, acid etched and anodized). However, $Mg_2Ca$ and $Ca_2Mg_6Zn_3$ the intermetallic compounds were more prominent on the surface of acid etched and anodized MZC. It should be noted that the presence of intermetallic compound such as $Ca_2Mg_6Zn_3$ in Mg alloys assists in enhancing their strength and toughness [64, 136]. Additionally, it was reported by Tao et al. (2008) that the secondary phases in the form of fine precipitates of $Mg_2Ca$ dispersed within the grains [93] played an important role in improving the corrosion resistance of the Mg-Zn-Ca alloy [90].

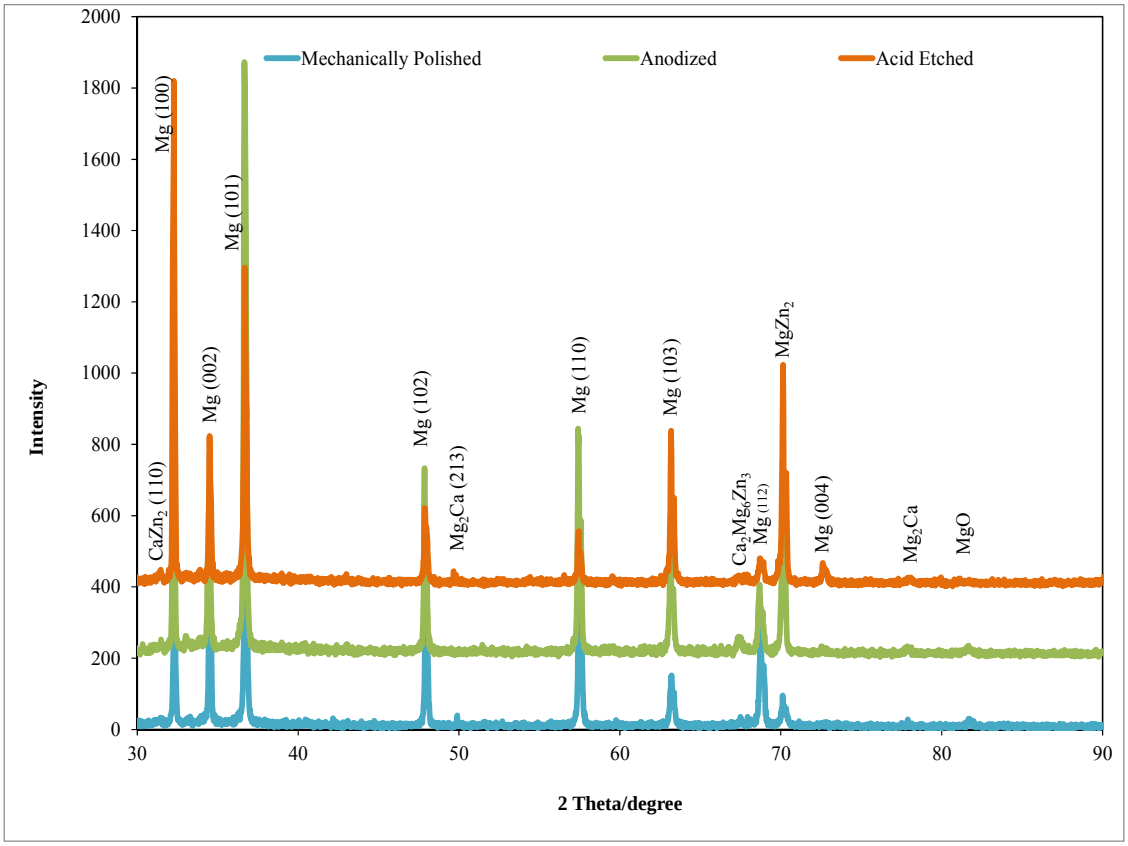


Figure 4.4: XRD spectra of surface treated MZC

## 4.4 Chemical Composition Analysis

X-ray photoelectron spectroscopy (XPS) is a surface characterization technique that provides both qualitative and quantitative surface chemistry of materials. In the present

research, a PHI Quantera scanning XPS microprobe employing 50 W monochromatic Al Kα X-ray radiation at 55 eV energy was utilized to obtain wide energy survey spectra (large area analysis mode - 200 μm diameter) to determine the elements present on the surface. High resolution O-1s, Mg-2s, Ca-2p and Zn-$2p^3$ spectra were acquired in order to determine their chemical states and concentrations. Sputter depth profiles were obtained using parameters of: 1kv1x1, 10 min, and 10 cycles.

### 4.4.1 Mechanically Polished MZC

The depth profile in Figure 4.5 (a) illustrates that Zn and O decrease with sputtering time whereas, Ca and Mg increase. The Montage plots of O–1s in Figure 4.5 (b) revealed two peaks at intensities 530.5 and 531.5 eV which correspond to MgO [34] and $Mg(OH)_2$ [1, 3] respectively. Montage plots of Mg-2s in Figure 4.5 (c) revealed component strong peak at a binding energy of 88.6 eV which corresponds to metallic magnesium. Additionally, the Montage plots in Figure 4.5 (e) revealed metallic Zn peak at a binding energy of 1021 -1022 eV. In the case of Ca, two peaks were observed at binding energies of 346.57 eV and ~353.6 eV as shown in Figure 4.5 (d). James et al. reported that the peak at higher binding energy (353-357 eV) was due to the plasmon loss due to the interaction between the photoelectron and other electrons. The peak at a binding energy of 346.57 eV corresponded to metallic Ca [137].

### 4.4.2 Acid Etched MZC

Similar to mechanical polishing, acid etched MZC's depth profile in Figure 4.6 (a) illustrates that Zn and O decrease with sputtering time whereas, Ca and Mg increase. Furthermore, the Montage plots of acid etched MZC in Figures 4.6 (b, d and e) similar to

mechanically polished MZC's revealed peaks of MgO (530.5 eV), $Mg(OH)_2$ (531.5 eV) metallic Zn (1021 -1022 eV) peak, metallic Ca peak (346.57 eV) and plasmon loss peak (~353.6 eV). However, Montage plots of Mg-2s in Figure 4.6 (c) revealed two peaks, strong peak of metallic magnesium at a binding energy of 88.6 eV and another less intense peak of magnesium oxide at a binding energy of 90.8 eV. This shows higher amount of oxides in the acid etched MZC when compared to mechanically polished MZC.

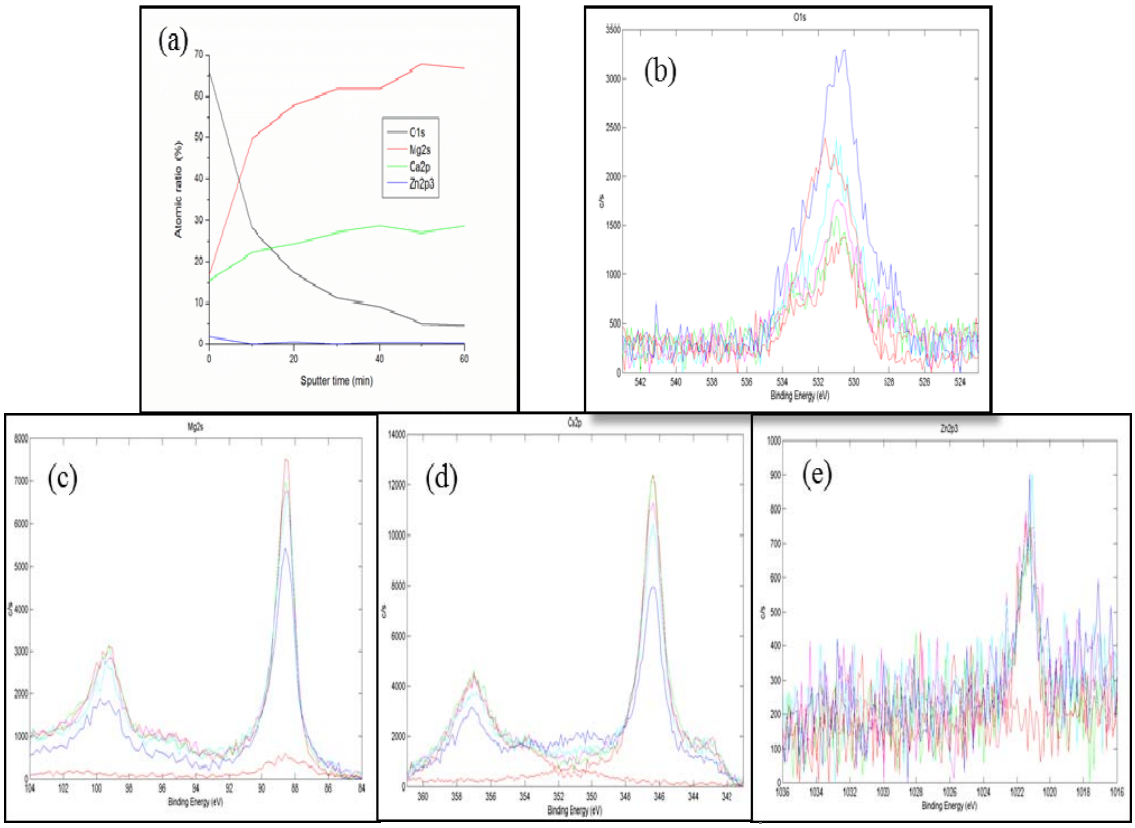


Figure 4.5: Depth profile (a) and Montage plots of (b) O, (c) Mg, (d) Ca and (e) Zn of mechanically polished MZC

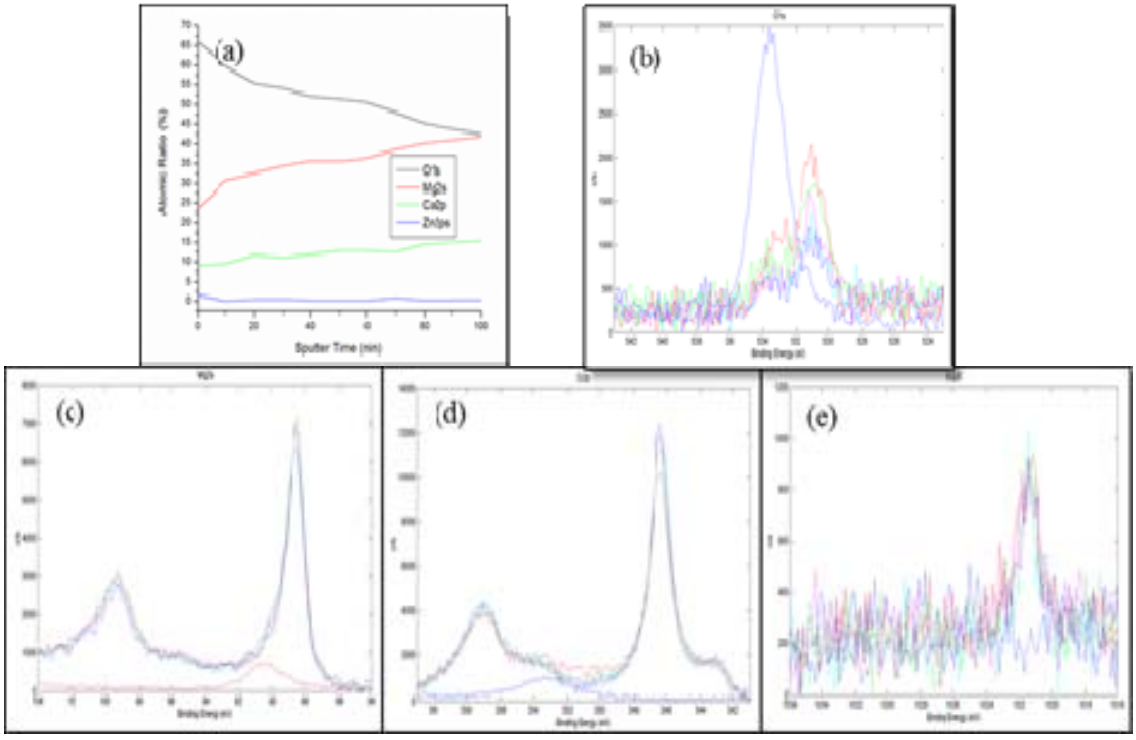


Figure 4.6: Depth profile (a) and Montage plots of (b) O, (c) Mg, (d) Ca and (e) Zn of acid etched MZC sample

### 4.4.3 Anodized MZC

Similar to mechanical polishing, anodized MZC's depth profile in Figure 4.7 (a) illustrates that Zn and O decrease with sputtering time whereas, Ca and Mg increase. Furthermore, the Montage plots of anodized MZC in Figures 4.7 (b, d and e) similar to mechanically polished MZC's revealed peaks of MgO (530.5 eV), $Mg(OH)_2$ (531.5 eV) metallic Zn (1021 -1022 eV) peak, metallic Ca peak (346.57 eV) and plasmon loss peak (~353.6 eV). However, Montage plots of Mg-2s in Figure 4.7 (c) revealed two peaks, less intense peak of metallic magnesium at a binding energy of 88.6 eV and strong peak of magnesium oxide at a binding energy of 90.8 eV. This shows higher amount of oxides in the acid etched MZC when compared to mechanically polished and acid etched MZC.

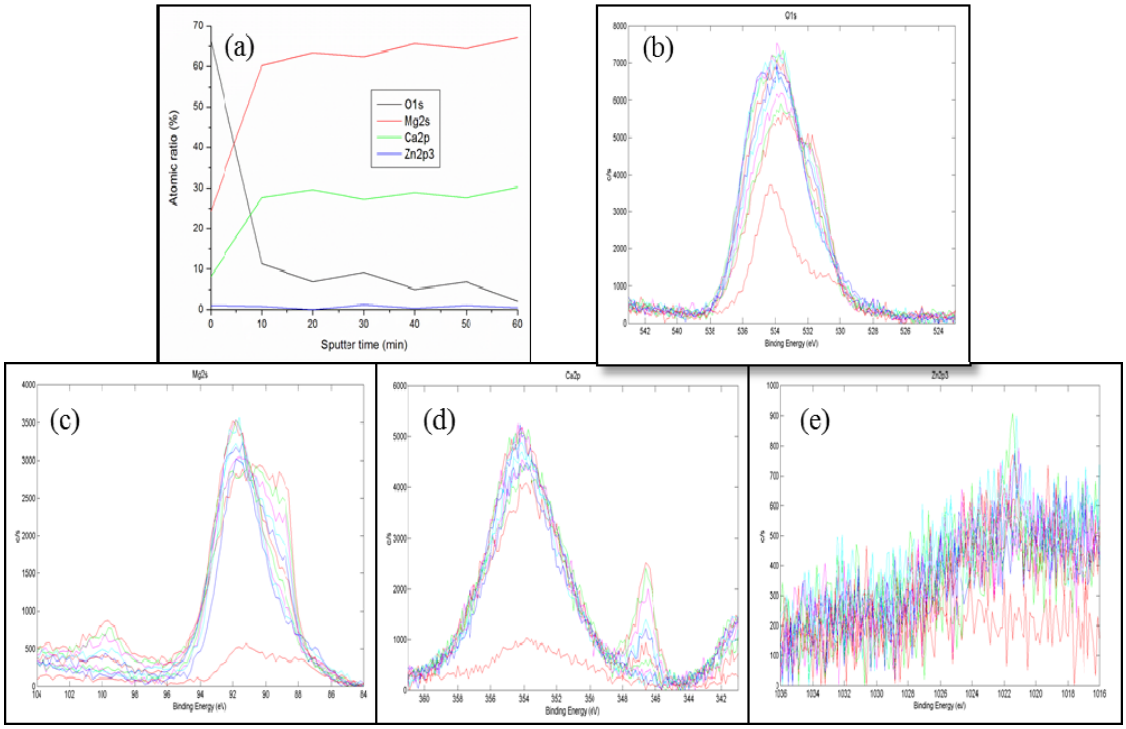


Figure 4.7: Depth profile (a) and Montage plots of (b) O, (c) Mg, (d) Ca and (e) Zn of anodized MZC sample

Depth profile analysis of MZC alloys in Table 4.2 shows that the surface elements such as O, Mg, Zn and Ca were always inevitable, with decreased Zn and O with sputtering time whereas, Ca and Mg increased. The oxygen profile exhibited a peak close to the surface and then decreased sharply showing that the surface of the MZC had a protective oxide layer. However, for anodized MZC, the oxide peak showed a different trend of almost a flat curve, which proves that the anodized sample had a thicker oxide layer.

Table 4.2: Depth profiles of (a) mechanical polished (b) acid etched and (c) anodized MZC samples

| Sputtering Time (Mins) | MP (At %) | | | | AE (At %) | | | | Anodized (At %) | | | |
|---|---|---|---|---|---|---|---|---|---|---|---|---|
| | O | Mg | Ca | Zn | O | Mg | Ca | Zn | O | Mg | Ca | Zn |
| **0** | 66.0 | 16.7 | 15.4 | 1.8 | 66.5 | 24.3 | 8.2 | 1.1 | 65.9 | 23.5 | 9 | 1.6 |
| **10** | 28.1 | 49.6 | 22.2 | 0 | 11.4 | 60.2 | 27.6 | 0.8 | 59.8 | 30.8 | 9.5 | 0 |
| **20** | 17.3 | 57.8 | 24.3 | 0.5 | 6.9 | 63.5 | 29.6 | 0 | 55.3 | 32.6 | 11.7 | 0.4 |
| **30** | 11.2 | 61.7 | 27.0 | 0 | 5.3 | 62.4 | 27.2 | 1.2 | 54.0 | 34.5 | 11.1 | 0.5 |
| **40** | 9.2 | 61.7 | 28.7 | 0.4 | 5.0 | 65.7 | 28.9 | 0.4 | 52.2 | 35.7 | 11.9 | 0.2 |
| **50** | 4.9 | 67.8 | 26.9 | 0.4 | 2.9 | 64.4 | 27.6 | 1.1 | 51.5 | 35.6 | 12.8 | 0.1 |
| **60** | 4.5 | 66.6 | 28.6 | 0.2 | 2 | 67.3 | 30.2 | 0.5 | 50.7 | 36.4 | 12.8 | 0.1 |
| **70** | 1.5 | - | - | - | - | - | - | - | 47.9 | 38.6 | 12.5 | 0.9 |
| **80** | - | - | - | - | - | - | - | - | 45.1 | 40.2 | 14.5 | 0.2 |
| **90** | - | - | - | - | - | - | - | - | 43.7 | 40.9 | 15.1 | 0.3 |
| **100** | - | - | - | - | - | - | - | - | 42.5 | 41.9 | 15.5 | 0.2 |

### 4.5 Surface Roughness Analysis

Optical profilometry is a non-contact interferometric-based method for characterizing surface topography. A typical optical profilometry analysis provides 2D and 3D images of the surface, roughness statistics and feature dimensions. In the current research, a PS50 optical profilometer (Nanovea, Irvine, CA) was used to determine the surface roughness of the samples and the images were processed through Scanning Probe Image Processor (SPIP) version 5.1 (Image Metrology, Denmark).

Figures 4.8 illustrate the surface roughness values of the MZC. These images indicate that the roughness of acid etched (~ 644 nm) and anodized (~ 564 nm) samples were greater than that of the mechanically polished MZC (~ 525 nm). Even though Liu et al reported increase in the surface roughness after acid etching [138] and Wang et al. reported an increase in roughness for anodized magnesium alloy [95], there was no significant increase in the surface roughness observed after surface treatments. This slight

variation in roughness after surface treatments was attributed to the formation of pores and cracks on the surface [95]. In general, pores and cracks act as cross linking sites to create good adhesion between the polymer and magnesium substrate, which increases the corrosion resistance of the magnesium alloy [95].

Additionally, optical profilometry was performed on the PGCL coated MZC which revealed no statistically different roughness between the bare metal and polymer coated MZC. It was reported that polymer coating results in a decrease in roughness due to sealing of pores and cracks [95, 121].

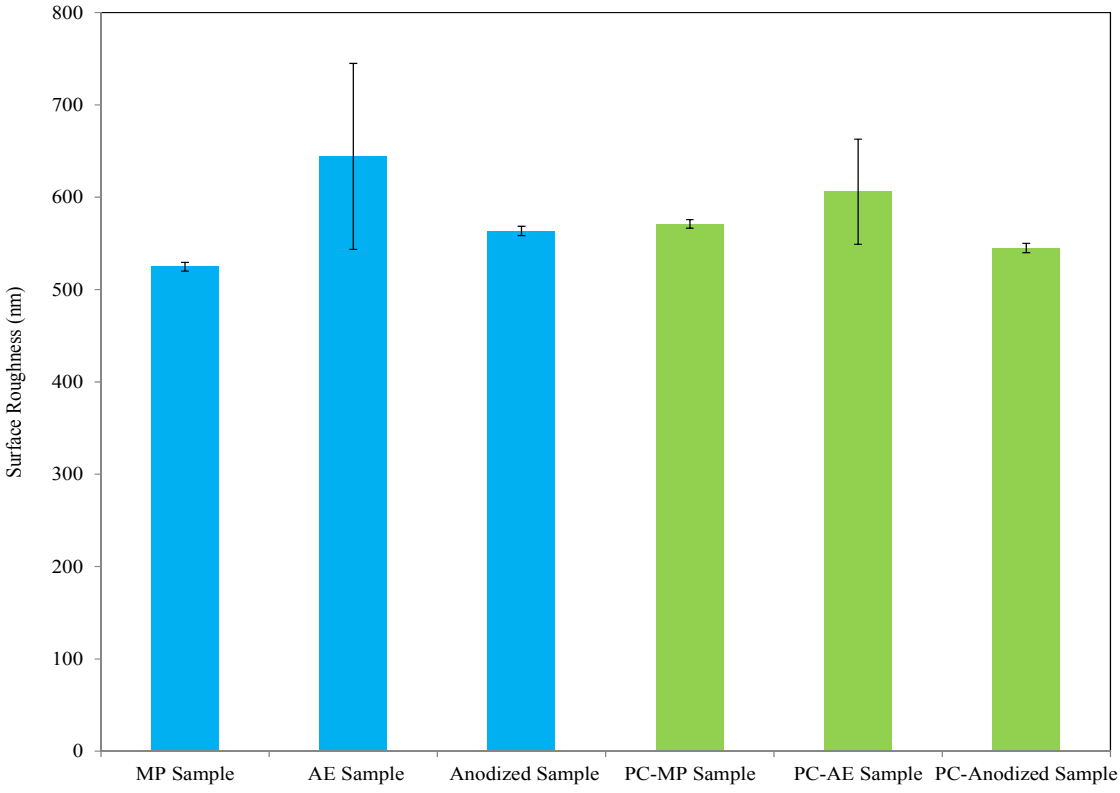

Figure 4.8: Surface roughness of MP, AE and anodized MZCs – a comparative study (mean ± SD, n = 5)

### 4.6 Polymer Coating Thickness Assessment

The thickness of the coatings was calculated using the formula 4.1 [102] where the sample dimensions (length, breadth and width) and the weight of the MZC were measured before and after coating the alloy with PGCL. The density of MZC alloy (1.76 g/mL) was provided by the manufacturer.

$$Thickness\ (\mu m) = \frac{Weight\ gain\ (g)}{density\ \frac{g}{cm^3} * surface\ area\ (cm^2)} * 10^4 \qquad 4.1$$

Figure 4.9 shows the calculated thickness of the polymer on mechanically polished, acid etched and anodized MZC samples. The thickness (~ 1 - 1.5 micron) of the polymer coating on anodized and mechanically polished MZC was less than that on acid etched MZC (~ 4.5 microns). Liu et.al reported that a thicker polymer coating is produced on rough magnesium surfaces due to the presence of higher number of nucleation sites [138]. It was also reported that a thin and less porous coating provided better adhesion due to enhanced interlocking between the polymer and the Mg substrate [98, 138].

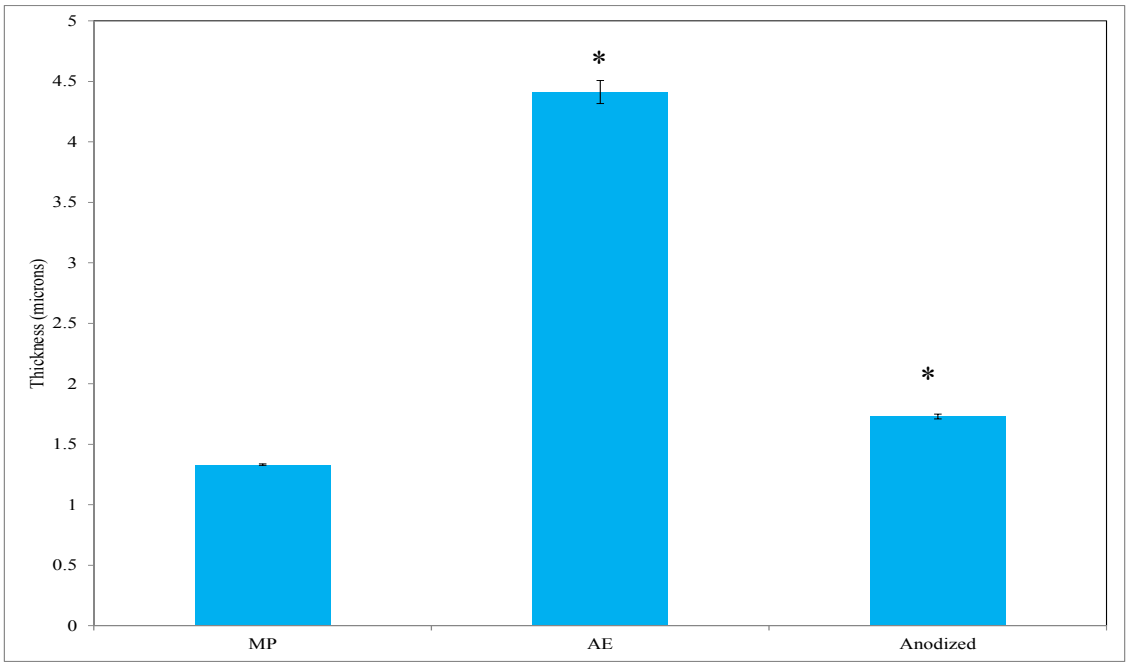


Figure 4.9: Polymer coating thickness of MP, AE and anodized MZC – comparative study (mean ± SD, n = 3)

Note: * refers to $p < 0.05$ indicating values are significantly different from MP MZC in one-way ANOVA analysis

### 4.7 Characterization of Polymer Bonds

Fourier transform infrared spectroscopy (FTIR) was utilized to characterize the PGCL bonds on the surface of MZC. A Jasco 4100 spectrometer equipped with an ATR-PRO450-S accessory was utilized with a reflectance angle of 80 degrees, 2048 scans at a resolution of 4 $cm^{-1}$ and in the frequency range of 300 $cm^{-1}$ and 5000 $cm^{-1}$. The chemical structure of the PGCL after copolymerization reaction is shown in Figure 4.11.

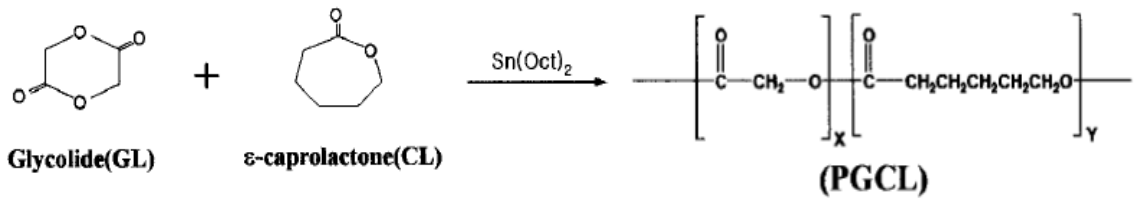

Figure 4.10: Chemical structure of PGCL after co-polymerization reaction

Figure 4.11 shows the FTIR spectra of PGCL and PGCL on surface treated MZC. The following are typical bonds identified in PGCL spectra: C-H bond vibrations (600-900 $cm^{-1}$), C=O stretching vibrations (1735- 1750 $cm^{-1}$), O-H stretch vibrations (3610–3670 $cm^{-1}$), C-C stretches (1100–1300 $cm^{-1}$) and aromatic C=C (1500 $cm^{-1}$) [124].

The FTIR spectra of PGCL obtained in this research displayed the following bonds in the respective band ranges: $CH_2$ stretching vibrations in the range of 2800 - 3000 $cm^{-1}$, C=O stretching vibrations at 1720 $cm^{-1}$, C-O and C-O-C stretching vibrations in the range of 1050 - 1250 $cm^{-1}$, and deformational $CH_2$ vibrations in the range 1300 - 1500 $cm^{-1}$. These bonds are characteristic of aliphatic polyesters [139].

The FTIR analysis in table 4.3 shows vibrational stretching of OH with intermolecular hydrogen bonding at 3610 - 3670 $cm^{-1}$. This hydrogen bonding is attributed to the electrostatic attraction between the hydroxides on the surface of MZC and the oxygen from PGCL as schematically illustrated in Figure 4.14.

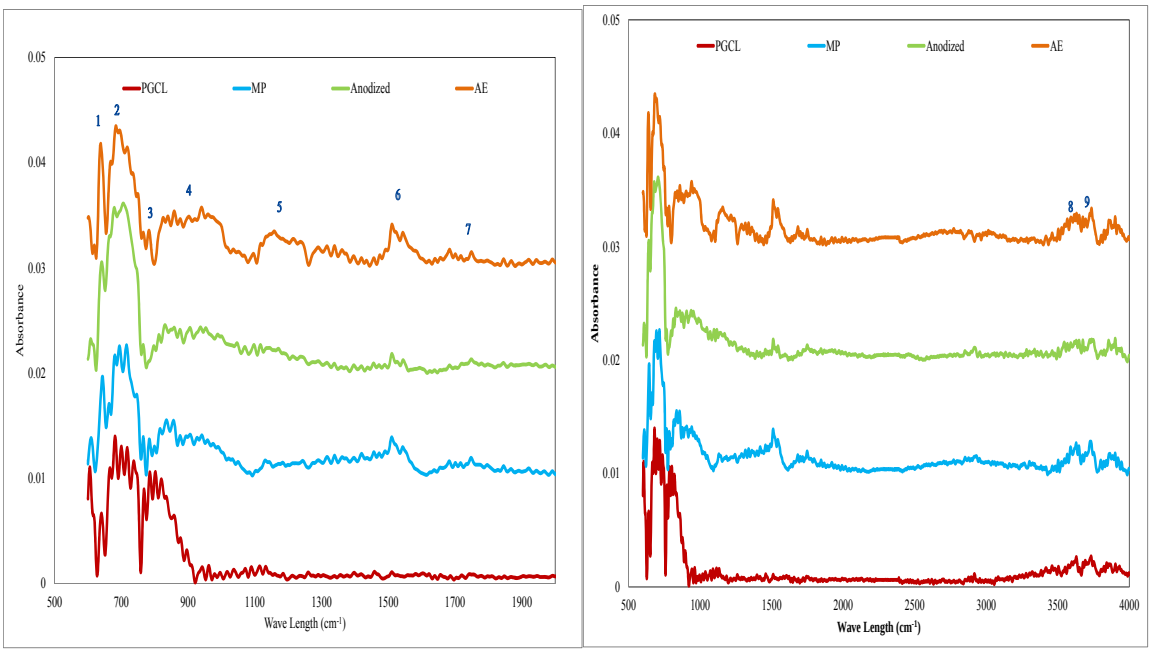


Figure 4.11: FTIR-ATR spectra of PGCL before and after polymer coating on surface modified MZC

Table 4.3 also indicates the formation of aromatic C═C bonds at 1500 $cm^{-1}$ and C-O-C at 1100–1300$cm^{-1}$ after MZC was coated with PGCL. The formation of C═C may be attributed to the electrostatic interaction between oxides on MZC and hydrogen in PGCL whereas, C-O-C bond formation may be attributed to the oxidation of polyester bonds in PGCL that create oxygenated groups. Pamula et al. reported that NaOH surface treatment of PGCL resulted in the formation of C=O, C-O and C-O-C oxygenated groups, which increased surface polarity and hydrophilicity [139]. The electrostatic interactions between MZC and PGCL that result in hydrogen bonding and the formation of C=C and C-O-C bonds are further discussed in section 8.7.

Table 4.3: FTIR bond stretching modes of PGCL and PGCL on surface treated MZC

| S.No | Peak Appearance | Bond | PGCL | MP | Anodized | AE |
|---|---|---|---|---|---|---|

| | | | | | | |
|---|---|---|---|---|---|---|
| 1 | 600-650 $cm^{-1}$ | Acetylenic C-H bend | ✓ | ✓ | ✓ | ✓ |
| 2 | 690–710 $cm^{-1}$ | C-H bend (monosubstituted benzene) | ✓ | ✓ | ✓ | ✓ |
| 3 | 750–800 $cm^{-1}$ | C-H bend (meta-disub. Benzene) | ✓ | ✓ | ✓ | ✓ |
| 4 | 800–840 $cm^{-1}$ | C-H bend (trisubstituted alkenes) | ✓ | ✓ | ✓ | ✓ |
| | 900 $cm^{-1}$ | C-H bend (monosubstituted alkenes) | ✓ | ✓ | ✓ | ✓ |
| | 990 $cm^{-1}$ | | | | | |
| 5 | 1100–1300$cm^{-1}$ | C-C stretch (ketones) | - | ✓ | ✓ | ✓ |
| | | C-O-C stretch (ethers) | | | | |
| 6 | 1500 $cm^{-1}$ | aromatic C═C | - | ✓ | ✓ | ✓ |
| 7 | 1735-1750 $cm^{-1}$ | C=O stretch | ✓ | ✓ | ✓ | ✓ |
| 8,9 | 3610–3670 $cm^{-1}$ | O─H stretchs (alcohols) | ✓ | ✓ | ✓ | ✓ |

### 4.8 Polymer Adhesion Strength

Scratch tests were performed to characterize the surface mechanical properties of thin films and coatings, e.g. adhesion, fracture and deformation. Polymer adhesion on the samples was tested using a Scratch Tester (CSM instrument SA) as shown in Figure 4.12. A cube-corner diamond tip (C-B37) was used throughout the test to provide scratch on the PGCL/MZC surface starting from the right to the left. A 2.5 mm scratch was made on each sample with a sliding velocity of 0.7 mm/min employing a progressive load from 0.3mN to 120mN.

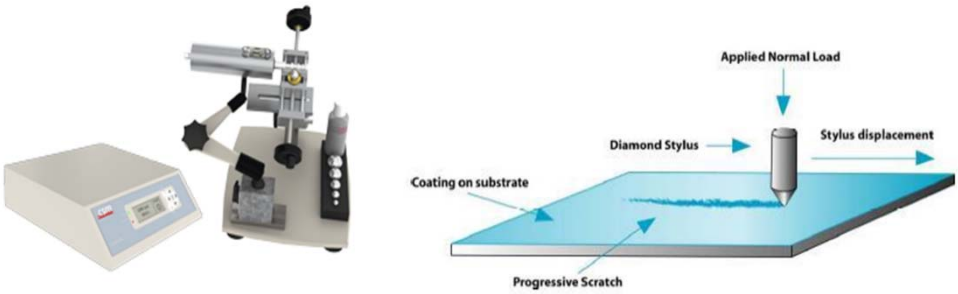


Figure 4.12: (a) Scratch tester (CSM instrument SA) (b) Schematic presentation of the scratch progression on the polymer coated sample

SEM-images of mechanically polished (a), acid etched (b) and anodized (c) MZC are shown in Figure 4.14. These SEM images assist in estimating the critical length and critical load applied to delaminate the PGCL coating from the MZC substrate. The critical length is defined as the distance from where the diamond tip touches the PGCL to the point at which it penetrates down to the MZC substrate. The critical load is defined as the magnitude of the load where the diamond tip penetrates through the PGCL down to the MZC substrate (depicted in the red circle of Figure 4.13). The adhesion strength between the PGCL and MZC substrate is directly proportional to the critical load.

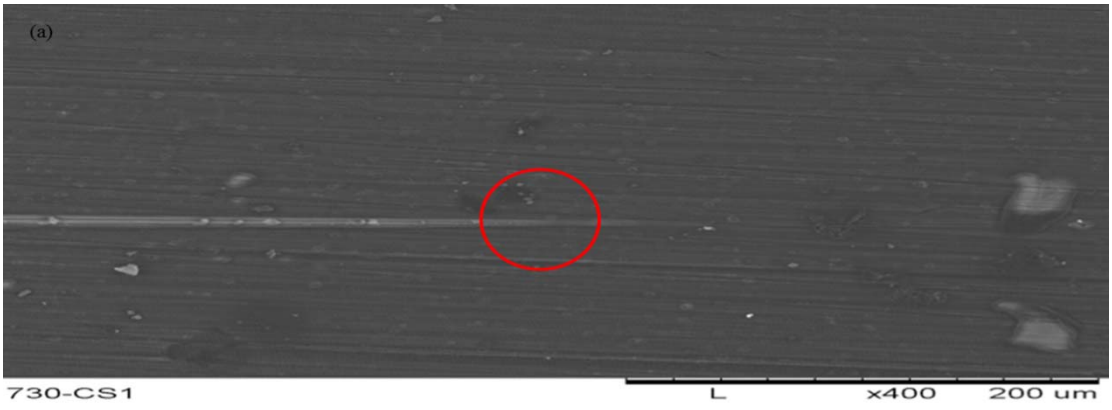

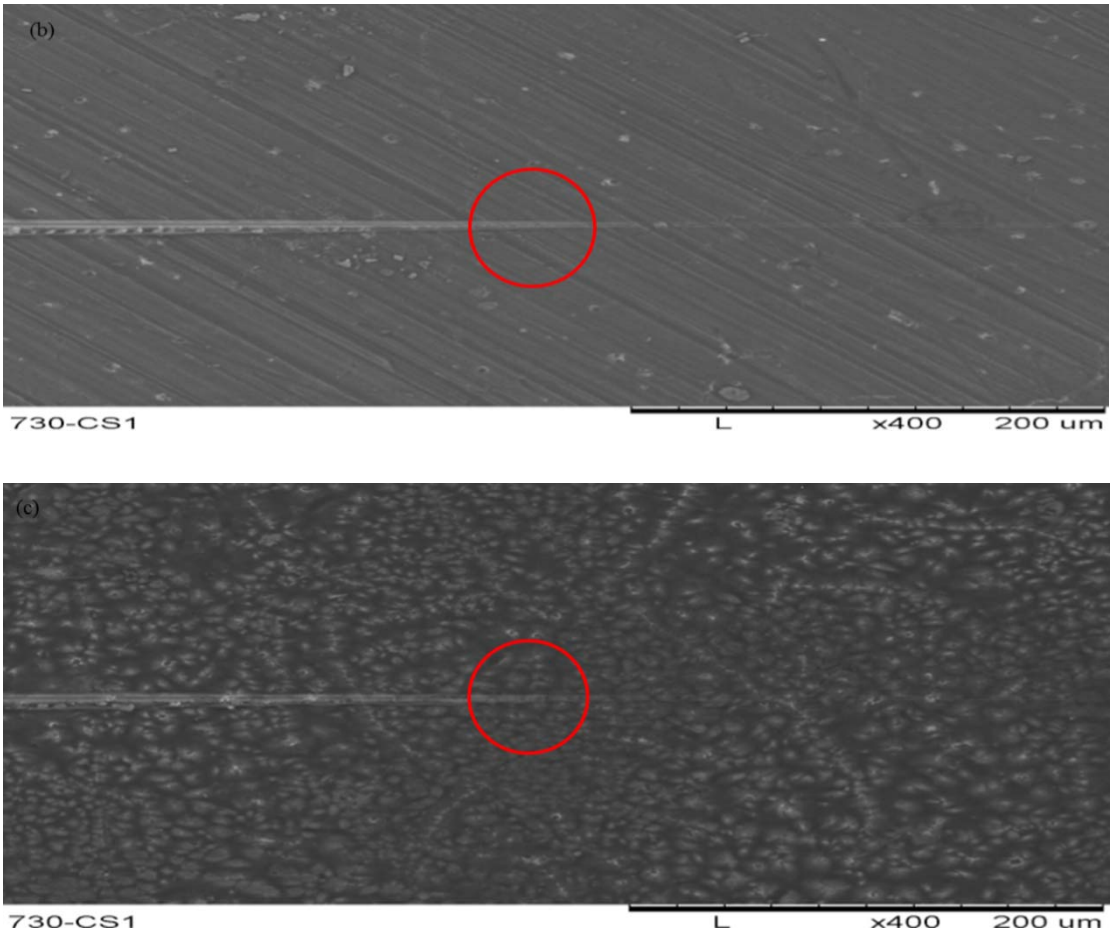


Figure 4.13: MZC alloy samples at x400 magnification: (a) MP, (b) AE and (c) anodized.

Table 4.4 shows that the critical loads applied on mechanically polished, acid etched and anodized MZCs were 12.5 mN, 12.1 mN and 12.7 mN respectively. It can be concluded that anodization may provide greatest adhesion between PGCL and MZC, since the latter had the highest critical load.

Table 4.4: Summary of the critical loads of the samples

| **Sample** | **Critical load** | |
|---|---|---|
| | **Length (mm)** | **Load (mN)** |
| Mechanically polished | 0.25 | 12.5 |
| Acid etched | 0.24 | 12.1 |

| | | |
|---|---|---|
| Anodized | 0.26 | 12.7 |

It should be noted that the adhesion between PGCL and anodized MZC is dependent on other parameters such as surface morphology, chemistry and roughness. Nevertheless, the surface morphology of anodized MZC revealed the presence of numerous cracks and pores that are known to serve as nucleation sites necessary for better adhesion. Additionally, XPS analysis of anodized MZC revealed a surface consisting primarily of oxides and hydroxides that were less prominent on mechanically polished and acid etched MZC. These hydroxides on the surface of MZC are presumed to create hydrogen bonding with PGCL as depicted in Figure 4.15 which results in strong adhesion.

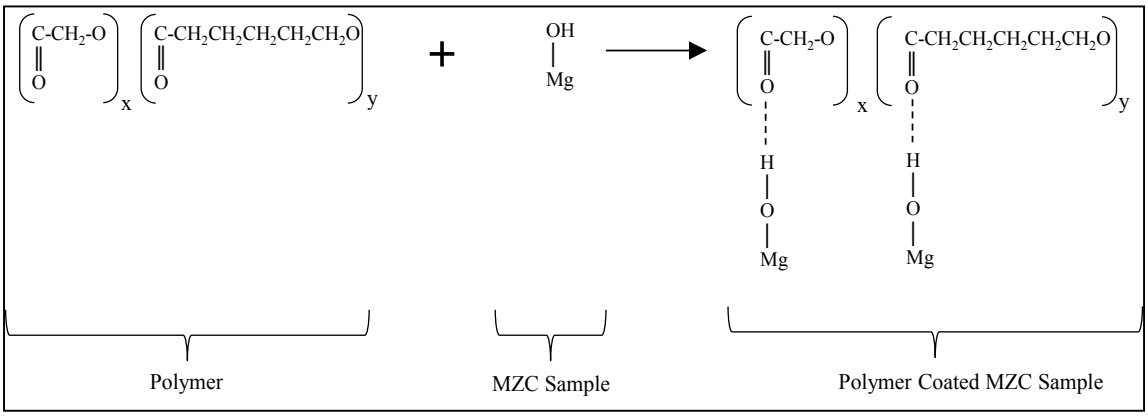


Figure 4.14: PGCL polymer and MZC sample bonds

### 4.9 Wettability Analysis

Contact angles were measured using a Kyowa contact angle meter model DM-CE1 (Figure 4.15 a) and adopting the sessile drop method. Three different solvents were employed: mildly polar (distilled water), neutral (ethylene glycol) and highly polar

(diiodomethane). Ten tests per solvent were performed on each specimen at locations separated by sufficient spacing (~ 0.5 mm) to prevent the potential influence of previous tests. Figure 4.16 (b) shows the contact angle formed by a liquid droplet resting on a solid substrate. According to Young-Dupre, the equation to measure contact angle $\theta$ can be expressed as [140]:

$$\gamma_{lv} \cos\theta = \gamma_{sv} - \gamma_{sl} \quad 4.2$$

where, $\gamma_{sv}$ is the surface energy of the solid, $\gamma_{sl}$ is the solid liquid interfacial energy, $\gamma_{lv}$ is the surface energy of the liquid and $\theta$ is the contact angle.

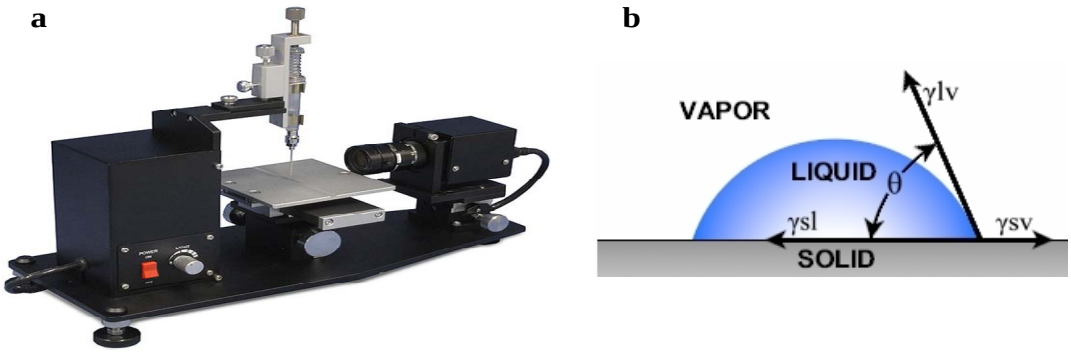


Figure 4.15: (a) Kyowa contact angle meter, DM-CE1 and (b) Schematic presentation of o liquid drop on a solid surface representing interfacial forces and contact angle.

FAMAS analysis software was used to evaluate the surface free energy (SFE) parameters of samples using the Lifshitz-van der Waals (LW) acid-base interaction and Kitazaki-Hata theory. Surface free energy was calculated using:

$$\gamma^{total} = \gamma^{d} + \gamma^{p} + \gamma^{h} \quad 4.3$$

where, $\gamma^{total}$ is the total SFE, $\gamma^{d}$ is SFE dispersion component, $\gamma^{p}$ is SFE polar component and $\gamma^{h}$ is SFE hydrogen bond component.

According to the energy interchange model of acid and base using water, the following energy balanced equation is established [141]:

$$\gamma_i(1 + cos\theta_i) = 2\left(\sqrt{\gamma_i^d \gamma_s^d} + \sqrt{\gamma_i^+ \gamma_s^-} + \sqrt{\gamma_i^+ \gamma_s^-}\right) \quad 4.4$$

where,

$$\gamma_i = \gamma_i^d + 2\sqrt{\gamma_i^+ \gamma_i^-} \quad 4.5$$

and,

$$\gamma_S = \gamma_s^d + 2\sqrt{\gamma_s^+ \gamma_s^-} \quad 4.6$$

Equation 4.4 characterizes a solid surface in terms of its surface free energy components, i.e., $\gamma_S^{LW}$, $\gamma_S^+$, and $\gamma_S^-$ that are determined from contact angles of three different liquids of known properties (in terms of $\gamma_L^+$, $\gamma_L^-$, $\gamma_L^{LW}$). Distilled water, ethylene glycol and diiodomethane were used in the sessile droplet contact angle measurements on the surface of MZC. This provided three equations with three unknowns, which were solved to obtain the values of $\gamma_S^{LW}$, $\gamma_S^+$, and $\gamma_S^-$.

| | |
|---|---|
| Where, | $\theta_i$ contact angle between solid and liquid |
| $\gamma_i$ surface tension of testing drop | $\gamma_s$ surface tension of solid sample |
| $\gamma_i^d$ dispersion portion of surface tension (testing drop, i) | $\gamma_s^d$ dispersion portion of surface tension (testing surface, s) Also referred to as $\gamma_S^{LW}$ Lifshitz-vander Waals component |
| $\gamma_i^+$ surface tension contribution by acid (testing drop, i) | $\gamma_s^+$ surface tension contribution by acid (testing surface, s) |

| | |
|---|---|
| $\gamma_i^-$ surface tension contributed by base (testing drop, i) | $\gamma_s^-$ surface tension contributed by base (testing surface, s) |

### 4.9.1 Wettability of Surface Treated MZC

The biocompatibility of an implant depends on its wettability and surface free energy which is obtained by measurement of its contact angle [141]. However, the contact angle of various solvents on a solid material is dependent on its surface characteristics which are influenced by surface treatments. Figure 4.16 displays contact angle, interfacial energy and work of adhesion measurement with distilled water (polar solvent) on surface treated MZC. The contact angle measured for mechanically polished, acid etched and anodized MZC were $80^\circ$, $65^\circ$ and $115^\circ$ respectively which indicates that anodization resulted in increased hydrophobicity ($> 90^\circ$) which has been reported to result in reduced platelet adsorption and subsequent reduced thrombogenicity [142].

Distilled water, ethylene glycol and diiodomethane were utilized for contact angle measurements on MZC. The interfacial interactions between solid and liquid are controlled by the interfacial surface tensions between two phases expressed by Young Dupres equation (4.2). The interfacial free energy for mechanically polished, acid etched and anodized MZC with distilled water were 35 mJ/m$^2$, 2.1 mJ/m$^2$ and 51 mJ/m$^2$ respectively, as compared with 44.8 mJ/m$^2$, 51.4 mJ/m$^2$ and 42.8 mJ/m$^2$ respectively for PGCL coated MZC as described in section 4.14.2. Again it should be noted that bare anodized MZC possessed the highest interfacial free energy (51 mJ/m$^2$) which decreased to 42.8 mJ/m$^2$ when coated by PGCL. It is proposed that polar parts of the polymer interact with water and this interaction mainly contributes to the interfacial free energy of the polymer coated MZC (decreased to that of polymer water interfacial energy), even

though the MZC itself has a high surface free energy. On the other hand, the low interfacial free energy of bare MP and AE MZC increased to that of the polymer water interfacial energy.

Posonnet et al. reported that an optimal interfacial free energy range of 30 - 50 $mJ/m^2$ is conducive for biocompatibility [143]. Andrade et al. [144] revealed that interfacial free energy is a more representative parameter to correlate biocompatibility than work of adhesion between the surface and the water. Nevertheless, the work of adhesion obtained in this investigation for mechanically polished, acid etched and anodized MZC was 95 $mJ/m^2$, 115 $mJ/m^2$ and 60 $mJ/m^2$ respectively which are inversely proportionally to interfacial energy.

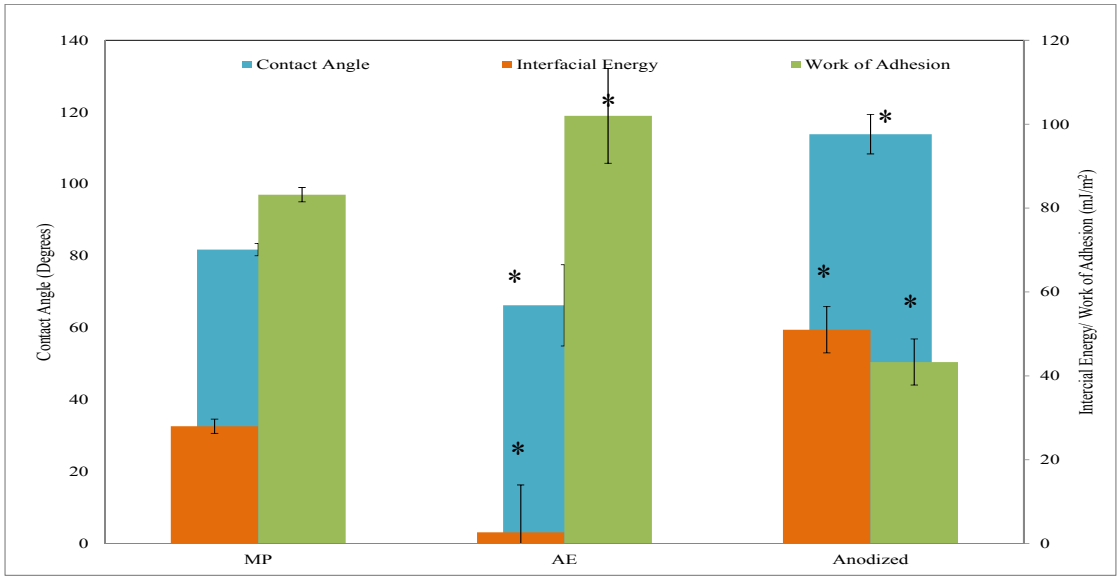


Figure 4.16: Acid-Base theory - contact angle, interfacial free energy and work of adhesion components for surface treated MZC (mean ± SD, n = 10)

Note: * refers to $p < 0.05$ indicating values are significantly different from MP MZC in one-way ANOVA analysis

Surface treated MZC exhibited high electron donor (basic) character as shown in Table 4.6. This is due to the presence of hydroxides as was previously discussed in section 4.13. In general, best cell adhesion, growth and spreading rate were recorded on polar and positively charged surfaces [145]. However, it was reported by Chang et al. that the surfaces grafted with neutral amide and hydroxyl groups also showed good Chinese hamster ovary (CHO) cell adhesion [145]. Thevenot et al. reported that negatively charged surface facilitates adsorption of proteins which promote cell adhesion, growth and responses [146]. Ponsonnet et al. (2003) observed similar acidic and basic characteristics for titanium and titanium alloys and reported good cell health [147].

Table 4.6: Acid-Base, average values of surface free energy components ($mJ/m^2$) for mechanically polished MZC

| Samples | Lifshitz-van der Waals (LW) $mJ/m^2$ | Acidic (Electron Acceptor) + | Basic (Electron Donor) - | Total mJ/m2 |
|---|---|---|---|---|
| Anodized | 21.5 | 0 | 0 | 21.5 ± 1.7 |
| MP | 38.4 | 0 | 6.3 | 44.7 ± 11.8 |
| AE | 30.8 | 0.1 | 23.2 | 54.1 ± 5.5 |

Lifshitz-van der Waals (LW) interaction is the sum of the attractive or repulsive forces between molecules and surfaces as well as other intermolecular forces. They differ from covalent and ionic bonding in that they are caused by correlations in the fluctuating polarizations of nearby particles (a consequence of quantum dynamics [148]). Van der Waals forces are relatively weak compared to covalent and ionic bonds but may play a role in PGCL/MZC adhesion. Table 4.6 shows the values of Lifshitz-vander Waals ($\gamma_S^{LW}$) component where the anodized MZC had the lowest contact angle. Giese et.al

reported that the values of $\gamma_S^{LW}$ decrease as the contact angle increases [148] as was found in this research. He further reported that surface treatment exposes more basal planes. Slow electron transfer kinetics has been reported on the basal plane of materials such as graphite and graphene as compared to kinetics at edges [149, 150]. Therefore, the creation of new basal surfaces after surface treatment caused a decrease in Lifshitz-van der Waals values and hence, a decrease in the value of $\gamma_S$. This suggests that anodization of MZC exposed more basal planes than acid etching and mechanical polishing.

Surface free energy (SFE) corresponds to the energy of the interface between the surface and water. It is well-known that a high energy metal surface in contact with air is covered with various layers, each leading to a decrease of the real surface free energy of the surface. The first layer may be an oxide or a sulphide on the metal, followed by strong polar bonds, such as water or $OH^-$ adsorption (water or alcohol interacts strongly with the –OH groups), the final layer having a relatively low surface free energy [147]. Studies have shown that cellular adhesion and cell activity were favorable on materials with low surface free energy within the range (20-50 $mJ/m^2$) [147, 151]. Gopinath et al. (2006) reported that high surface energy (57 $mJ/m^2$) increased the risk of thrombogenicity [152].

Figure 4.17 shows the dispersive, polar and hydrogen components that contribute to the total surface free energy of MZC by the Kitazaki-Hata method. The total surface free energy of mechanically polished, acid etched and anodized MZCs was 38 $mJ/m^2$, 33 $mJ/m^2$ and 23 $mJ/m^2$ respectively. It should be noted that the surface free energy obtained by the acid-base method for anodized MZCs was 21.5 $mJ/m^2$. This was attributed to the

exposal of basal planes as a result of anodization as well as the formation of a thick and dense oxide/hydroxide layer that lowered the surface energy of the MZC.

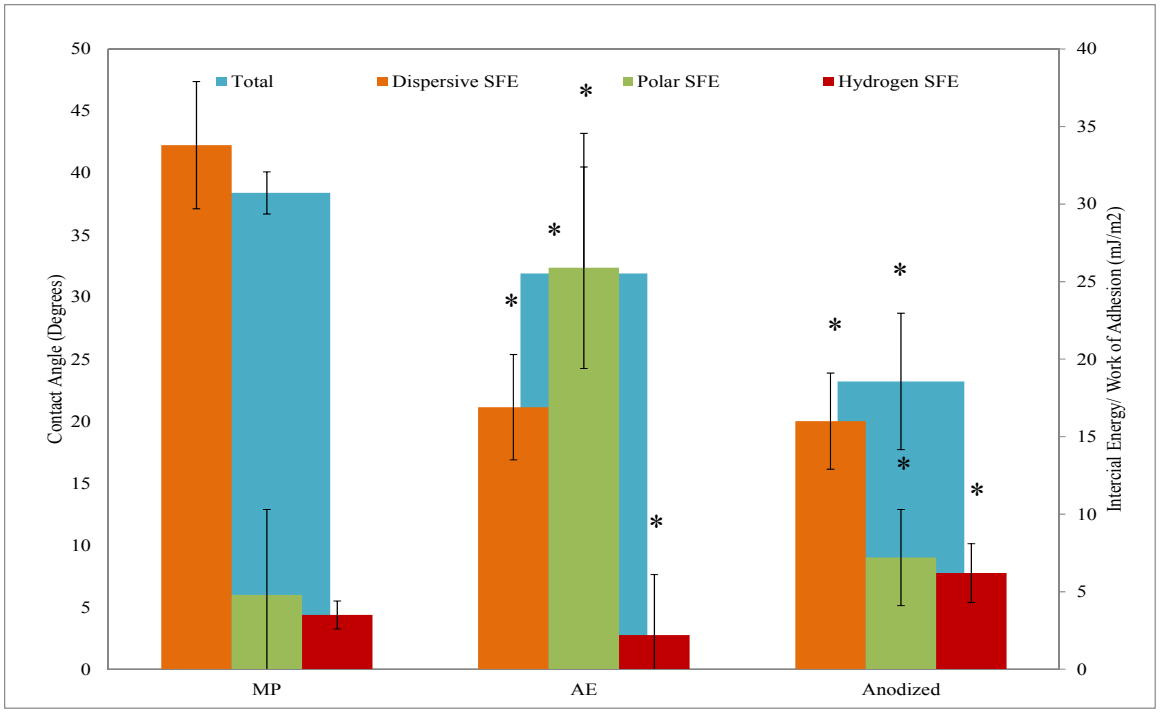


Figure 4.17: Kitazaki-Hata surface free energy components of surface treated MZC (mean ± SD, n = 10)

Note: * refers to $p < 0.05$ indicating values are significantly different from MP MZC in one-way ANOVA analysis

Fractional polarity of the surface treated MZC was calculated using the following equation that utilizes polar and dispersive components of SFE.

$$FP = \text{polar} / \text{dispersion} + \text{polar}$$

The FP of mechanically polished, acid etched and anodized MZC was 0.1, 0.6 and 0.3 respectively. An FP less than 0.3 has been reported to be favorable for good cellular

adhesion and fibroblast proliferation [147]. The relation between surface charge and cellular adhesion revealed that adhesion strength over a range of charge densities were influenced by electrical potential-dependent adhesion maxima, suggesting that surface treatment and alloying for optimum adherence may be possible. In this investigation, anodized and mechanically polished MZC possessed better cell adhesion properties than acid etched.

### 4.9.2 Wettability of PGCL Coated MZC

Figure 4.18 displays contact angle, interfacial energy and work of adhesion measurement with distilled water (polar solvent) on PGCL coated MZC. The contact angle measured for PGCL coated mechanically polished, acid etched and anodized MZC were 112°, 109° and 103° respectively with no statistical significant difference. It should be noted that all the PGCL coated MZC surfaces were hydrophobic (contact angle > 90°) whereas the bare metals, except for anodized MZC were hydrophilic (contact angle < 90°). Manoharan et.al reported that hydrophobicity is conducive to reduced platelet adhesion and subsequently can lead to reduced thrombogenicity [153].

The interfacial free energy of PGCL coated mechanically polished, acid etched and anodized MZCs was 44.8 $mJ/m^2$, 51.4 $mJ/m^2$ and 42.8 $mJ/m^2$ respectively. As previously mentioned the bare anodized MZC possessed the highest interfacial free energy (51 $mJ/m^2$) which decreased to 42.8 $mJ/m^2$ when coated by PGCL. On the other hand, the low interfacial free energy of bare MP (95 $mJ/m^2$) and AE (115 $mJ/m^2$) MZC increased to 44.8 $mJ/m^2$ and 51.4 $mJ/m^2$ respectively which are dependent on the polymer water interfacial energy. It is proposed that polar parts of the polymer interact

with water and this interaction mainly contributes to the interfacial free energy of the polymer coated MZC (decreased to that of polymer water interfacial energy), even though the MZC itself has a high surface free energy.

Posonnet et al. reported that an optimal interfacial free energy range of 30 - 50 $mJ/m^2$ is conducive for biocompatibility [143]. Andrade et al. [144] revealed that interfacial free energy is a more representative parameter to correlate biocompatibility than work of adhesion between the surface and the water. Nevertheless, the work of adhesion obtained in this investigation for mechanically polished, acid etched and anodized MZC was 45.7 $mJ/m^2$, 102 $mJ/m^2$ and 49.2 $mJ/m^2$ respectively which are inversely proportionally to interfacial energy.

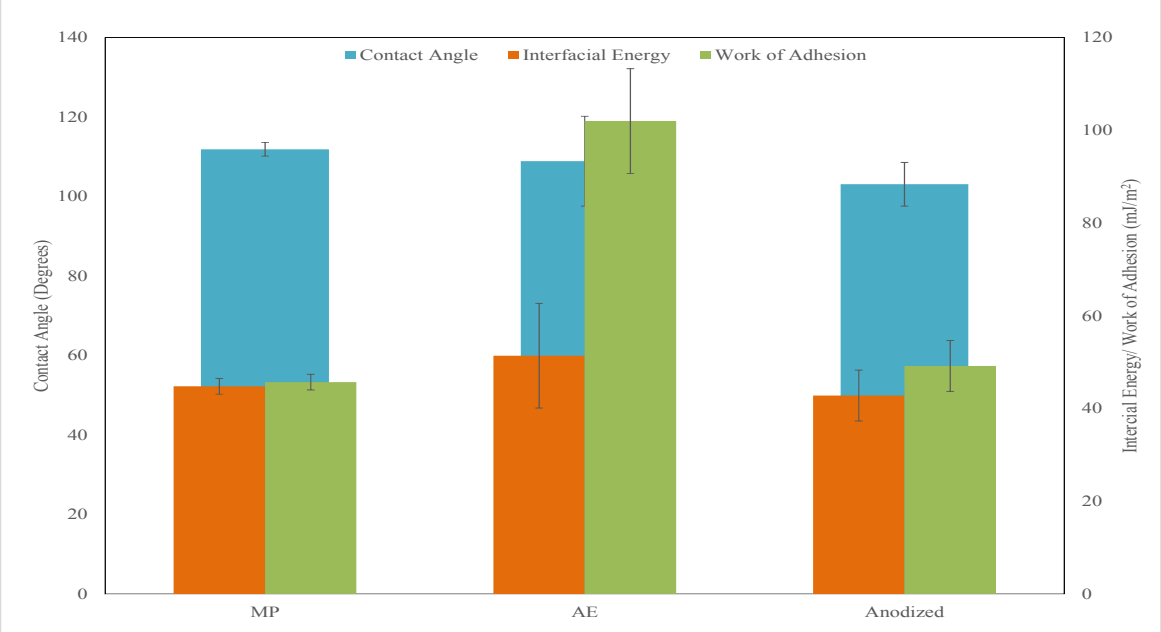


Figure 4.18: Acid-Base theory contact angle, interfacial free energy and work of adhesion components for polymer coated MZC (mean ± SD, n = 10)

PGCL coated anodized MZC exhibited high electron donor (basic) character as shown in Table 4.7. It should be noted that all of the surface free energy properties were

dependent on the polymer water interfacial interaction because of similar vander Walls and total SFE.

Table 4.7: Acid-Base surface free energy components of polymer coated MZC

| PC MZC | Lifshitz-van der Waals (LW) | Acidic (Electron Acceptor) + | Basic (Electron Donor) - | Total mJ/m2 |
|---|---|---|---|---|
| MP | 27.7 | 0 | 0.4 | 28.1 ± 3.2 |
| AE | 27.8 | 0 | 0 | 27.8 ± 8.6 |
| Anodized | 26.2 | 0 | 0.7 | 26.9 ± 1.8 |

Figure 4.19 shows the dispersive, polar and hydrogen components that contribute to the total surface free energy of PGCL coated MZC by the Kitazaki-Hata method. The total surface free energy of PGCL coated mechanically polished, acid etched and anodized MZCs was was 30.6 mJ/m$^2$, 51.4 mJ/m$^2$ and 27.7 mJ/m$^2$ respectively. It should be noted that PGCL coated anodized MZC possessed the lowest surface free energy when compared to acid etched and mechanically polished. Again, this was attributed to the exposure of basal planes on the bare metal, formation of a thick and dense oxide/hydroxide layer and hydrogen bonding between the hydroxides on the surface of MZC and the oxygen from PGCL as schematically illustrated in Figure 4.15.

The FP of the PGCL coated mechanically polished, acid etched and anodized MZ was 0.27, 0.6 and 0.13 respectively. As previously mentioned, an FP less than 0.3 has been reported to be favorable for good cellular adhesion and fibroblast proliferation [147].

The results obtained from contact angle measurements suggest that coating of anodized and mechanically polished MZC with PGCL could potentially result in a

biomaterial that would provide favorable cell viability as is further described in section (6.2.3).

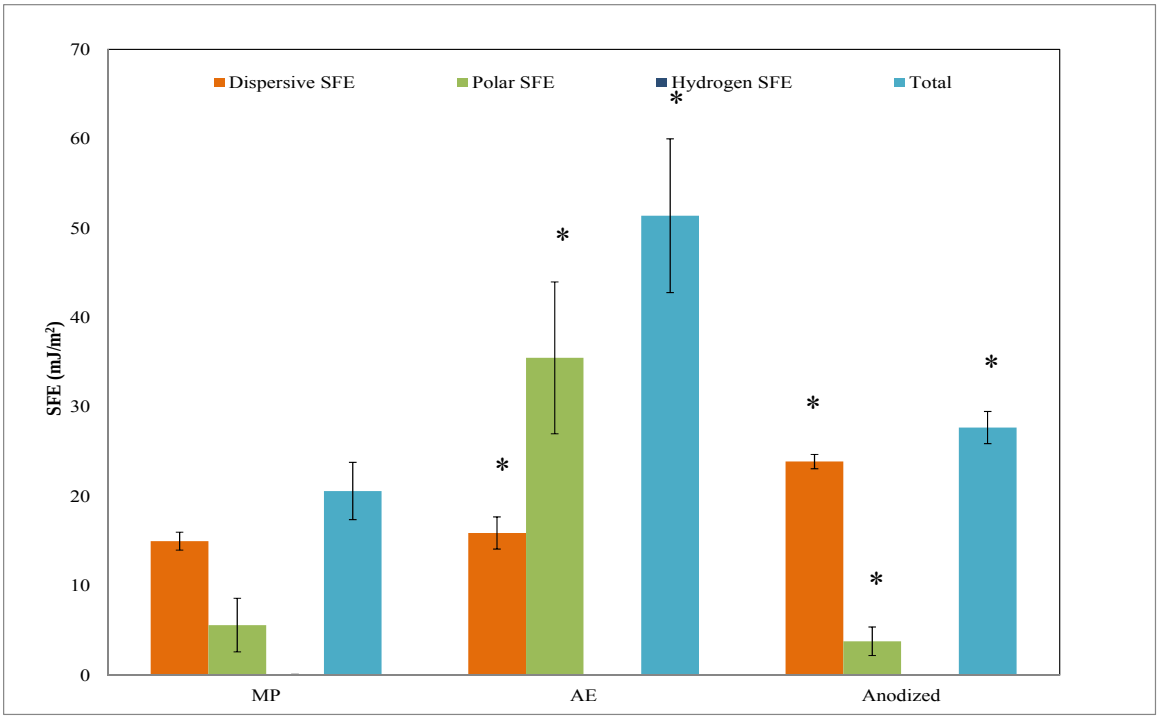


Figure 4.19: Kitazaki-Hata surface free energy components of polymer coated MZC (mean ± SD, n = 10)

Note: * refers to $p < 0.05$ indicating values are significantly different from MP MZC in one-way ANOVA analysis

# 5. CORROSION STUDIES

Corrosion is a diffusion controlled process that occurs between anodic and cathodic sites that are connected by an electrolyte. Generally, corrosion is unwanted in engineering and science applications. But in the case of biodegradable implants, corrosion phenomenon can revolutionize the biomedical industry if the material's degradation rate can be controlled [154]. For example, biodegradable magnesium has a very high corrosion rate of 407 mm/year [77]. However, it is required that biodegradable magnesium for stent applications should have a corrosion rate less than 0.2 mm/year [45], should maintain its mechanical integrity for 3-6 months and fully dissolute in 1- 2 years [43]. In order to reduce the corrosion rate of magnesium, a MZC alloy with a corrosion rate of 2.9 mm/yr [155] was selected in this study. Additionally, to maintain the alloy's mechanical integrity, surface treatments (acid etching and anodizing) and PGCL coating were performed to reduce the alloy's initial degradation rate.

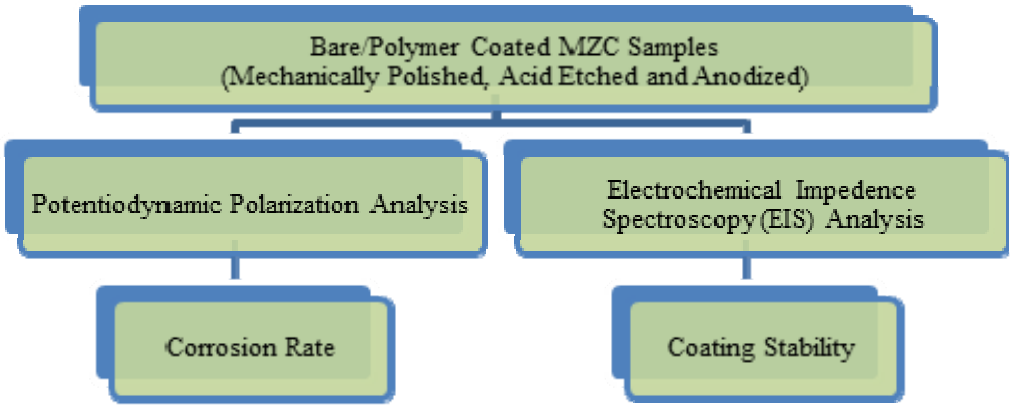


Figure 5.1: Schematic of corrosion tests

This chapter describes the corrosion studies performed in the current research to analyze the relative corrosion rates and degradation phenomena of the PGCL coated and

surface treated MZC. A schematic of the corrosion studies performed are displayed in Figure.5.1.

### 5.1 What is Corrosion?

Corrosion in general is the degradation of a material due to its interaction with the surrounding environment [156]. All materials are susceptible to corrosion, especially metals in which the corrosion occurs by an oxidation reaction and the surface of the metal will be oxidized by the surroundings. Corrosion normally occurs at a rate determined by equilibrium between opposing electrochemical reactions. An anodic reaction occurs when the metal is oxidized releasing electrons into the metal. A cathodic reaction, in which a solution species (often $O_2$ or $H^+$) consumes the electrons released from the metal. When these two reactions are in equilibrium, the flow of electrons from each reaction is balanced, and no net electron flow (electrical current) occurs. The two reactions can take place on one metal or on two dissimilar metals (or metal sites) that are electrically connected.

Magnesium when exposed to the environment develops a thick amorphous layer composed of magnesium hydroxide ($Mg(OH)_2$) on the surface, the rate of formation of which is dependent on the type of surrounding environment. For example, in atmospheric air the formation of $Mg(OH)_2$ is slow (around 0.01 mm/yr), relative to that in salt water (around 0.30 mm/yr) [157]. Therefore, an understanding of the degradation behavior of MZC in simulated biological environment is vital since such fluids contain chlorides that are highly aggressive.

## 5.2 Corrosion of Magnesium in Biological Environment

Body fluids are primarily composed of water but contain dissolved oxygen, proteins and electrolytic ions such as chlorides and hydroxides, which provide a highly corrosive environment for magnesium. Magnesium under standard conditions has an electrode potential of -2.37 V which makes it susceptible to corrosion. Thus, magnesium oxidizes at anodic sites by releasing $Mg^{2+}$ ions into the fluid according to equation (5.1). Then, water is reduced at cathodic sites by consuming the electrons released from magnesium and hydrogen gas is released according to equation (5.2). Furthermore, the production of $OH^-$ increases the pH of the solution, which favors the formation of a magnesium hydroxide layer. The overall corrosion of magnesium can be expressed by equation (5.3).

$$2Mg\ (s) \rightarrow Mg_2 + (aq) + 2e^- \qquad \text{(Oxidation - Anodic Reaction)} \qquad (5.1)$$

$$2H_2O\ (aq) + 2e^- \rightarrow H_2\ (g) + 2OH^-\ (aq) \qquad \text{(Reduction - Cathodic Reaction)} \qquad (5.2)$$

$$Mg\ (s) + 2H_2O\ (l) \rightarrow Mg\ (OH)_2\ (s) + H_2\ (g) \qquad \text{(Overall Reaction)} \qquad (5.3)$$

$$Mg^{2+}\ (aq) + 2OH^-\ (aq) \rightarrow Mg\ (OH)_2\ (s) \qquad (5.4)$$

The $Mg(OH)_2$ layer formed on the metal surface is slightly soluble and reacts with chloride ions to form highly soluble magnesium chloride and $OH^-$ ions [39] according to equation (5.5) which increases the pH.

$$Mg\ (OH)_2\ (s) + 2Cl^-(aq) \rightarrow MgCl_2 + 2OH^- \qquad (5.5)$$

Additionally, magnesium chloride can also be produced when chloride ions diffuse through hydroxide layer and reach the metal substrate according to equation (5.6).

$$Mg\ (s) + 2Cl^-(aq) \rightarrow MgCl_2 + 2e^- \qquad (5.6)$$

However, when the hydroxide layer fully covers the metal surface; it acts as a passive layer and prevents further migration of ionic species to and from the metal substrate and limits the occurrence of equation (5.6). Nevertheless, chloride ions may breakdown the $Mg(OH)_2$ layer and result in dissolution of the magnesium substrate according to equation (5.5) releasing $Mg^{2+}$ into the fluid. Hydrogen gas is released by the reduction of water according to equation (5.2).

Magnesium chloride undergoes hydrolysis (5.7) liberating hydrochloric acid (HCl) that can corrode the metal surface. However, the acid produced may be neutralized by hydroxyl ions released from equations (5.2) and (5.5).

$$MgCl_2 + 2H_2O\ (l) \rightarrow Mg\ (OH)_2\ (s) + 2HCl \qquad (5.7)$$

Witte et al. reported that patients equipped with stents made of magnesium alloy experienced rapid formation of subcutaneous hydrogen gas bubbles within the first week of surgery, which subsequently disappeared after 2 to 3 weeks [63]. Song et al. postulated that humans can tolerate a hydrogen evolution rate of 0.01 $ml/cm^2/day$ and that this rate does not constitute a serious threat [62]. Thus, if the corrosion rate of Mg alloys can be controlled so that the rate of hydrogen evolution is in the range 0.01 $ml/cm^2/day$, then the formation of subcutaneous hydrogen gas bubbles may not pose a threat. In an effort to reduce the hydrogen gas release as well as to control pH, zinc was added as an alloying element in the current research as discussed in section 1.10.1.

### 5.3 Types of Biological Corrosion

An important property of the oxide/hydroxide layer on Mg alloys is its ability to maintain its mechanical integrity and remain un-delaminated or ruptured under stress. A

rupture or delamination of the passivating oxide/hydroxide may expose the substrate to body fluids which will result in corrosion. The clinical implication of corrosion therefore, is the loss of mechanical strength which may result in ultimate failure of the alloy. Typical types of corrosion that Mg alloys are subjected to are described below.

### 5.3.1 Galvanic Corrosion

As discussed in section 5.2, magnesium is highly reactive due to its very low electrochemical potential. Therefore, the presence of metallic phases in magnesium alloys increase the potential of galvanic corrosion [158]. Galvanic corrosion is an electrochemical process in which one metal that has lower electrode potential corrodes preferentially to another when both metals are in electrical contact. Magnesium with its low electrode potential is susceptible to galvanic attack which leads to severe localized corrosion next to a cathodic second phase that is comprised of zinc and other alloying elements of higher electrode potential [96]. Song et al. reported the formation of large pits next to the Mg-Zn-Y-Zr cathodic second phase in a wrought alloy [159]. Cathodes can be external metals (more noble than magnesium such as Ni, Fe and Cu) in contact with magnesium, or may be internal as secondary phases or impurity phases. Metals such as Al, Zn, Cd, and Sn that are less noble than Ni, Fe and Cu are much less damaging. The further apart metals and secondary phases are in the galvanic series, the greater is the tendency for galvanic corrosion to occur.

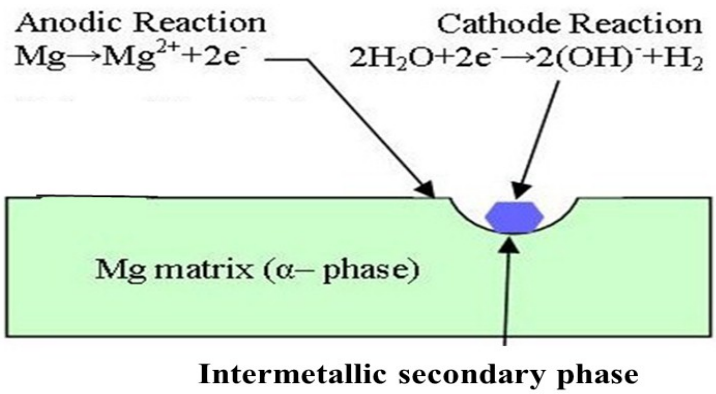


Figure 5.2: Schematic of galvanic corrosion as a result of internal cathodic secondary phase

In the case of MZC, the secondary phase ($CaZn_2$) acts as the internal cathode (Figure 5.2) [96]. Although the electrode potential of calcium (- 2.87 V) is more active than magnesium (- 2.37 V), it is over shadowed by two moles of Zn (-0.76 V) in the intermetallic secondary phase resulting in an overall electrode potential of – 1.46 V which is more noble than that of magnesium. Hence, the intermetallic serves as the cathode and magnesium corrodes preferentially.

### 5.3.2 Granular Corrosion

In many metal alloys, inter-granular corrosion occurs due to the presence of impurities and inclusions which segregate at the grain boundary during solidification. As previously discussed, galvanic reactions occur between the metal matrix and various impurities and inclusions depending on their galvanic potential (difference in reduction potential in the galvanic series). The ensuing galvanic corrosion at the grain boundary may exceed that of the metal matrix in the grains [160]. Figure 5.3 depicts the typical

morphology of a magnesium alloy, where the grain boundaries are depleted due to intergranular corrosion.

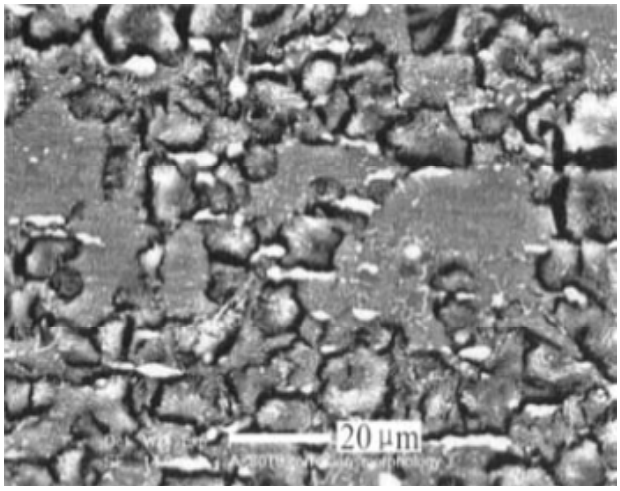


Figure 5.3: Intergranular corrosion morphology of magnesium alloy [160]

### 5.3.3 Pitting Corrosion

Pitting corrosion is most common in magnesium alloys as compared with other types of corrosion. Pitting is an autocatalytic process i.e. the corrosion processes within the pit produce conditions, which are necessary for the continuing activity of the pit. In this process, rapid dissolution occurs within the pit and oxygen reduction takes place on adjacent surfaces. Rapid dissolution produces an excess of positive charges, which attracts chloride ions to maintain electro-neutrality. Both chloride and hydrogen ions produce hydrochloric acid, which further stimulate the dissolution of the metal and the process accelerates with time. Extremely low concentration of the oxygen is available within the pit, so no oxygen reduction occurs. Oxygen reduction on the adjacent passivated surfaces tends to suppress corrosion, and in that way pits cathodically protects the rest of the alloy surface [161].

Figure 5.4 depicts the schematic illustration of localized corrosion with pits which damage the protective surface oxide layer. The pits are small, highly corrosive and continue to grow downwards, perforating the metal matrix [161]. The surface pits are difficult to see due to the presence of corrosion products. After initial nucleation at the surface, the presence of impurities in the magnesium alloy's microstructure often assist in further corrosion due to the galvanic differences in the materials [161, 162]. The environment within the pit is very aggressive, with chlorides from the body fluids and $Mg^{2+}$ ions from anodic dissolution greatly aggravating the corrosion.

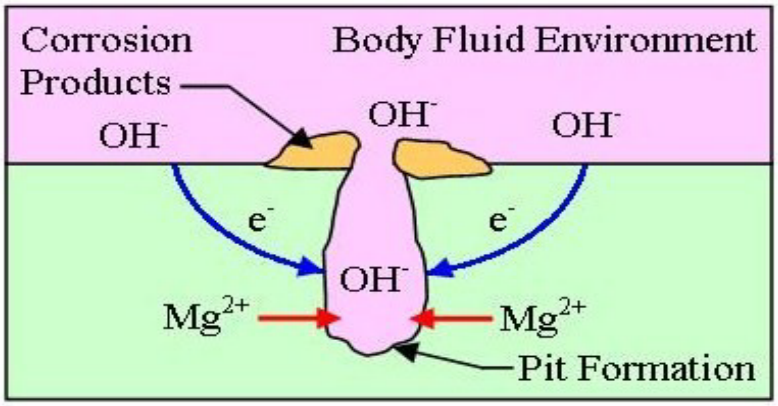


Figure 5.4: Schematic of pitting corrosion occurring on magnesium

In addition, the mouth of the pit is small and prevents any dilution of the pit contents, which adds to accelerating autocatalytic growth of the pit. During this process, electrons flowing from the pit cause the surface surrounding the pit entrance to be cathode-protected which further weakens the protective oxide layer. Once pitting starts, the magnesium alloy can be totally penetrated within a relatively short period of time and in the case of a biomedical implant, its mechanical properties could be greatly reduced to the point of failure. Another problem associated with pitting arises from localized increase in stress produced by the pit, which has the potential to form cracks [163].

### 5.3.4 Crevice Corrosion

Crevice corrosion is based on a similar mechanism to pitting corrosion, but occurs in stagnant areas where fluid diffusion is limited. In crevice corrosion, an increase in the concentration of chloride ions, low pH and low oxygen concentration results in a breakdown of the passivation layer. This creates conditions that increase the solubility of the metal oxide film. Elimination of oxygen within a crevice and the presence of a cathodic area outside the crevice with a high concentration of oxygen can lead to the development of an anodic area within the crevice and consequently to crevice corrosion. In fact, the difference in oxygen concentration between anodic and cathodic areas leads to crevice corrosion as shown in Figure 5.5. Because there is no sensitivity to difference in oxygen concentration in the corrosion of magnesium, crevice corrosion does not appear in magnesium alloys [158] [96]. Special type of crevice corrosion is filiform corrosion.

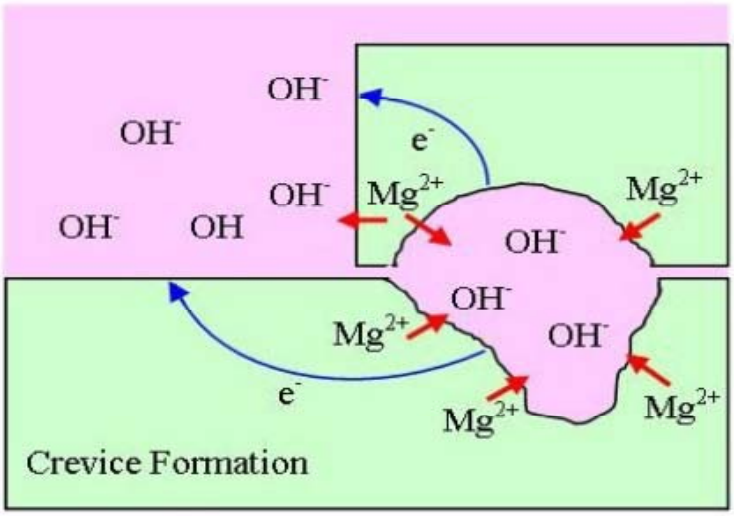


Figure 5.5: Schematic of crevice corrosion of Mg in a body fluid environment [96]

### 5.3.5 Filiform corrosion

Filiform corrosion that is commonly known as "localized" and is normally linked to magnesium and aluminum alloys that utilize an organic form of coating. However, it can

also occur on other coated metals such as steel, iron and zinc. It is caused by active galvanic cells across the metal surface. Its head is anodic, whereas the tail is cathodic. Filiform corrosion initiates corrosion pits. It is typically associated with metal surfaces having an applied protective coating and it is not common for uncoated magnesium alloys [162] [163]. However, few researchers observed filiform corrosion for magnesium alloys such as AZ91 (Mg-9Al-1Zn) and AZ31 [19] [164].

### 5.3.6 Stress Corrosion Cracking

It has been reported by Song et.al that stress corrosion cracking (SCC) may occur in magnesium-based implants in a load bearing applications – such as coronary stents under the loading of blood vessel and blood flow, plates and screws for orthopedic fixation under the loading of body weight and movement [165]. SCC occurs when magnesium alloys are exposed to tensile stress and certain environmental conditions whereby cracks develop that would not occur in the absence of either of those controlling parameters. In general, it has been accepted that hydrogen plays a major role in the stress-corrosion cracking (SCC) behavior of magnesium alloys. Based on the assumption of hydrogen over-voltage, Winzer et al. suggested that the hydrogen fugacity at the surface of magnesium could be many orders of magnitude higher than that for steel exposed to an aqueous environment [166]. Thus, internal blisters and cracks develop when hydrogen accumulates in localized areas which lead to failure at stress levels far below the yield strength.

The progress of SCC is influenced by the strain rate of implant loading cycles and the presence of hydrogen gas produced by the corrosion process [161]. As previously

described in section (5.2), chloride ions in the body fluid can ultimately lead to a breakdown of surface oxide/hydroxide layer exposing the underlining Mg substrate. The resulting hydrogen diffuses into the stressed zone where the crack initiation occurs. The crack advances due to pressure built up of hydrogen [162-164]. SCC initiated cracks propagate rapidly and extend between the grains throughout the metal matrix [165]. Fracture and failure of the implant will occur when the SCC is below the normal operating stress of the implant.

The threshold of stress for SCC is defined as the stress below which cracking does not occur, and is a function of alloy composition, structure, environmental conditions, including solution composition, potential and temperature. A better definition of threshold of stress for SCC is the stress above which total failure occurs, since some crack systems initiate below the threshold but cease to propagate after some growth. Strain rate, however, appears to be the determination factor as far as crack propagation is concerned and not so much the severity of stress. So that when the strain rate at the crack tip falls below some critical value, crack propagation ceases [166].

### 5.4 Methods of Measuring Corrosion Rate

Electrochemical techniques are ideal for the study of the corrosion processes because it provides accelerated corrosion rates as oppose to conventional weight loss/gain method that requires an extended period of time for measurements. In electrochemical studies, a metal sample of a known surface area is used to model a redox reaction occurring on the surface of a metal immersed in an electrolyte. The potential between the metal and a reference electrode is varied using a potentiostat and the current flowing through a

counter electrode is measured as a function of potential. The corrosion rate is governed by Faradays law equation [167, 168]:

$$Q = \frac{nFW}{M} \tag{5.8}$$

where, Q is the total current (coulombs), n is the number of electrons involved in the electrochemical reaction, W is the weight of the metal (grams), M is the Molecular weight (grams) and F is the Faraday's constant (96,486.7 coulombs/mole).

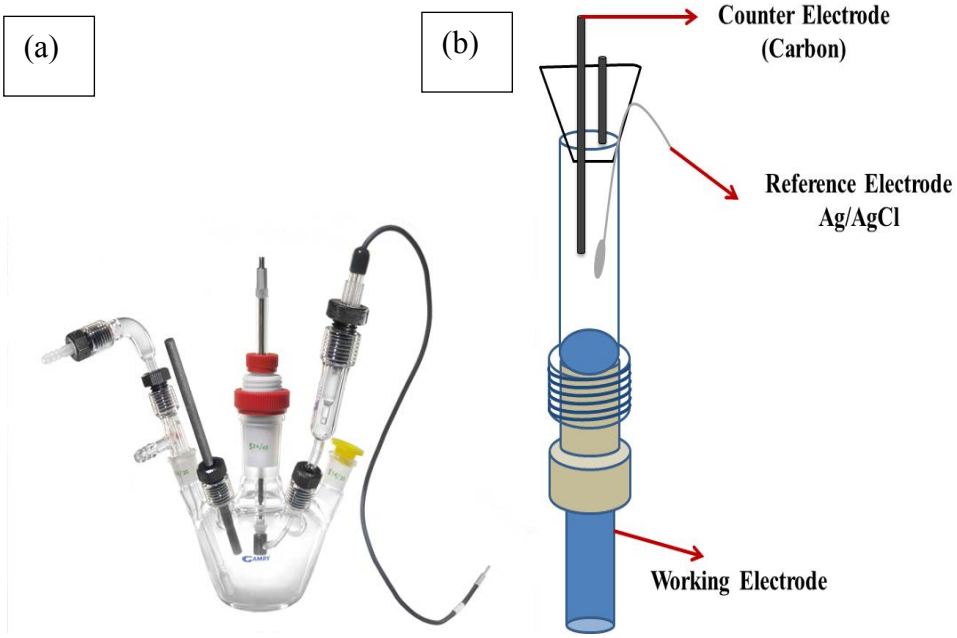


Figure 5.6: (a) Typical three electrode cell arrangement and (b) schematic of potentiostat corrosion cell arrangement designed for current research

A widely applied electrochemical method for the determination of corrosion rate is potentiodynamic polarization technique. However, electrochemical impedance spectroscopy (EIS) has been found to be suitable for assessing the stability of coatings on metals [169, 170].

In general, electrochemical methods utilize a typical three electrode (working, counter and reference electrodes) corrosion cell, inter-phased with a potentiostat to study the electrochemical behavior of metal and the stability of the coating. As shown in the Figure 5.6, the metal serves as the working electrode whereas; carbon or platinum as the counter electrodes and calomel or silver/silver chloride as reference electrodes. A Phosphate Buffer Saline solution (PBS) is used as the electrolyte.

### 5.4.1 Potentiodynamic Polarization Method

In the current research, potentiodynamic polarization tests were performed in accordance with ASTM G 102-89 at 37 °C employing a GAMRY potentiostat (G-750) to assess the corrosion behavior of MZC. During this test, the MZC (working electrode) was subjected to accelerated corrosion in PBS that was purged with nitrogen until the rest potential was relatively constant. The potential between working electrode (carbon) and the reference electrode (Ag/AgCl) was increased in positive direction at a scan rate of 1.0 mV/s. The current flowing between the working electrode and counter electrode was measured on a high impedance ammeter. The data obtained from cathodic and anodic polarization measurements was plotted with the current density ($A/cm^2$) on the x axis (logarithmic axis) and the potential (V) on the y axis (linear axis) as shown in Figure 5.7. A Tafel fit was employed to analyze these polarization curves by extrapolating the tangent (Tafel slopes) of the cathodic and anodic curves to $E_{corr}$. Figure 5.7 displays the tafel slopes and the corrosion current ($i_{corr}$) that were obtained by interception of the curves.

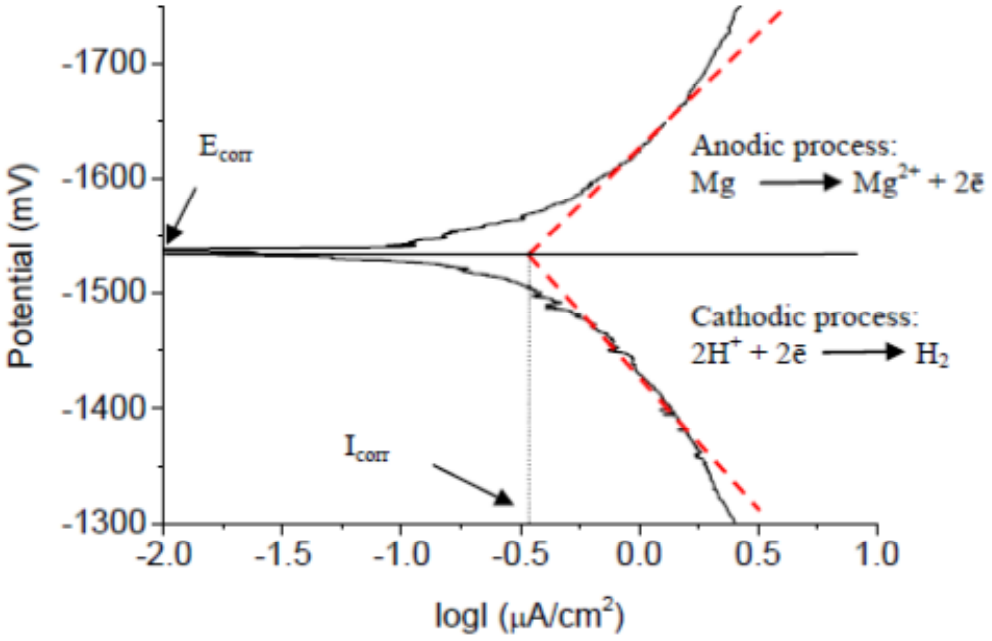


Figure 5.7: Schematic description of the Tafel plots

After the determination of the corrosion current ($i_{corr}$), the corrosion rate (CR) was determined by utilizing Faraday's law (5.8). The corrosion rate (W/t) was calculated by incorporating the charge (Q = I T) and the Faraday's constant in (5.8):

$$CR = \frac{I_{corr}.K.EW}{\rho.A} \tag{5.9}$$

where, $I_{corr}$ is the corrosion current (amps), K is a constant for the corrosion rate (3272 mm/amp.cm.year), EW is the equivalent weight in grams/equivalent, A is the sample area (0.28 $cm^2$) and ρ is the density ($g/cm^3$) of the alloys. The sample area of the MZC exposed to the electrolyte corresponded to the diameter of the O-ring assembly that was used to secure the working electrode and the glass cylinder shown in Figure 5.7.

### 5.4.1.1 Potentiodynamic Polarization Test Analysis

The potentiodynamic polarization curves obtained for surface treated MZC are shown in Figure 5.8. The jagged anodic curves were indicative of continuous breakdown (pitting corrosion) and passivation of surface treated MZC [91, 155].

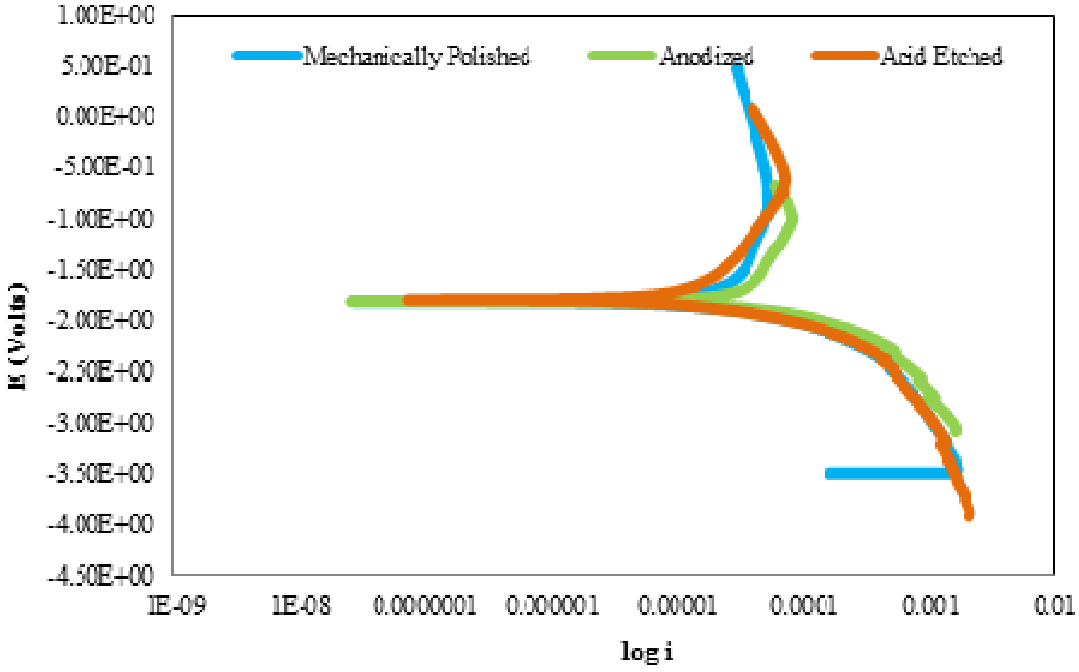


Figure 5.8: Potentiodynamic polarization curves of surface treated MZC in PBS at 37 $^{o}$C

Utilizing the data obtained from Tafel slopes, the corrosion rates were calculated using the equation 5.9. The corrosion potential ($E_{corr}$) and corrosion current density ($i_{corr}$) characterize the corrosion resistance of MZC [171]. Table 5.1 provides the $E_{corr}$, $I_{corr}$ and calculated corrosion rates of surface treated MZC. In general, a high corrosion potential and a low corrosion current density are indicative of good corrosion resistance [172].

Table 5.1 shows that the anodized MZC had better corrosion resistance with a high corrosion potential of -1.71 V and low corrosion current density of 2.54E-05 μA, when compared to mechanically polished (-1.85 V and 5.84E-05 μA) and acid etched (-1.86 V and 5.84E-05 μA) MZC.

The corrosion rate of anodized MZC (5.81 mm/year) was three times lower than that of acid etched MZC (17.3 mm/year). This is attributed to the presence of a dense oxide/hydroxide layer which passivated the surface of anodized MZC. All three surface treatments led to the formation of the protective oxide/hydroxide layer. According to Hwang et al., the low corrosion rate of anodized MZC was primarily due to a thicker passivating layer than that produced by MP and AE [173]. This observation was confirmed by EDS and XPS analysis of surface treated MZC described in sections 4.2 and 4.3 where a higher oxide/hydroxide composition was detected on the surface of anodized samples. This indicated that modification of the existing oxide layer on MZC by anodization enhanced its corrosive resistance more so than acid etching and mechanically

Table 5.1: Average potentiodynamic polarization data of surface treated MZC

| Sample | $E_{corr}$ (V) | $I_{corr}$ (μA) | Corrosion rate (mm/year) |
|---|---|---|---|
| **MP** | -1.85 | 5.84E-05 | 13.4 |
| **AE** | -1.86 | 7.57E-05 | 17.3 |
| **Anodized** | -1.71 | 2.54E-05 | 5.8 |

Figure 5.9 shows the potentiodynamic polarization curves of surface treated MZC that was coated with PGCL. It can be seen that the PGCL coated acid etched MZC was most susceptible to corrosion (lowest $E_{corr}$) and had the highest corrosion rate (higher

$I_{corr}$). Additionally, PGCL coated anodized MZC was least susceptible to corrosion (highest $E_{corr}$) and had the least corrosion rate (0.13 mm/yr).

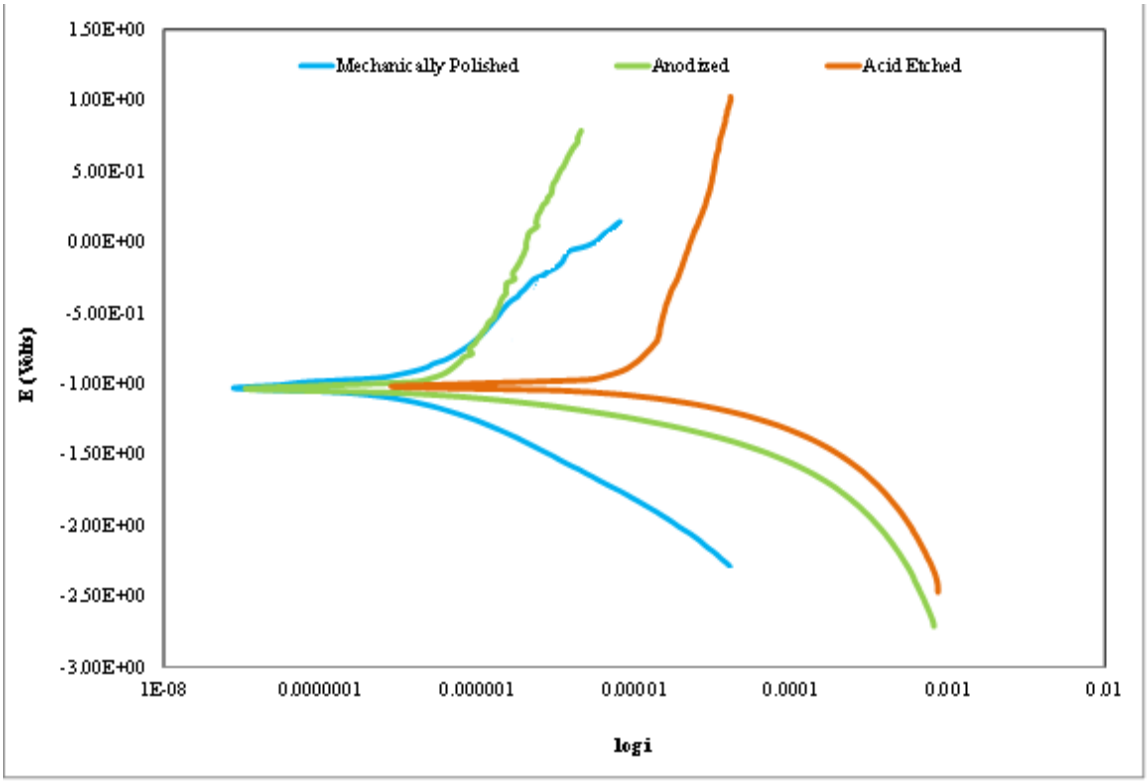


Figure 5.9: Potentiodynamic polarization curves of PGCL coated MZC in PBS at 37 $^{o}$C.

Table 5.2 summarizes the corrosion potential, current density and corrosion rates of the surface treated MZC coated with PGCL where it can be seen that PGCL coated anodized MZC was more corrosion resistant (0.13 mm/yr) which is 1 order of magnitude greater than that of PGCL coated mechanically polished MZC (1.4 mm/yr).

Table 5.2: Average potentiodynamic polarization data of PGCL coated MZC

| Sample | Ecorr (V) | Icorr (µA) | Corrosion rate (mm/year) |
|---|---|---|---|
| **MP** | -1.54 | 6.13E-06 | 1.4 |

| | | | |
|---|---|---|---|
| **AE** | -1.42 | 2.22E-06 | 0.5 |
| **Anodized** | -1.02 | 5.63E-07 | 0.13 |

The histogram in Figure 5.10 compares the corrosion rates of bare metal surface treated MZC and that of their PGCL coated counterparts where it can be observed that PGCL coating significantly reduced the corrosion rate. This was attributed to the combined effect of the PGCL coating and dense oxide/hydroxide layer that served as a protective barrier between the electrolyte and the MZC substrate. A similar reduction in corrosion rate ( mm/yr to mm/yr) was reported by Wang et al. who coated MgZnMn alloy with PCL[122].

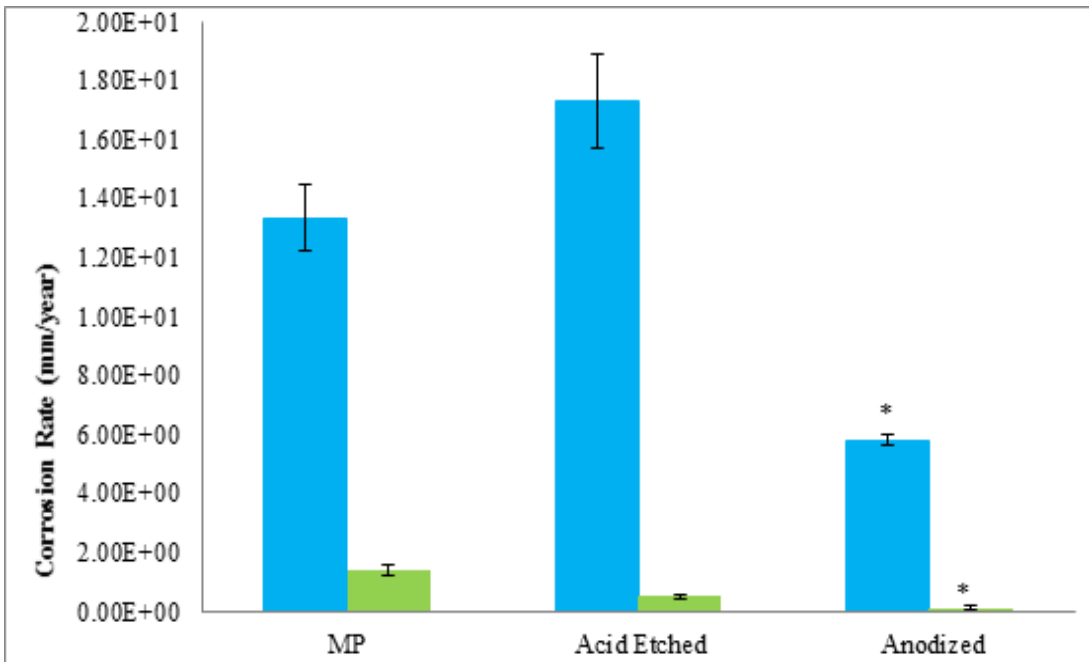


Figure 5.10: Histographic representation of corrosion rates (bare metals and PGCL coated MZC) (mean ± SD, n = 3)

Note: * refers to $p < 0.05$ indicating values are significantly different from mechanically polished MZC in one-way ANOVA analysis

#### 5.4.1.2 Surface Morphology after Corrosion

The surface morphology of surface treated and polymer coated MZC after corrosion was observed by SEM. The photomicrographs of Figure 5.11 revealed isolated white regions with cracks embedded in the gray surface that are characteristic morphology associated with the corrosion of magnesium [121]. The cracks were formed due to the dehydration of the layer after drying under ambient conditions [21]. For example, the mechanically polished and anodized MZC were composed primarily of grey matrix with cracks and white regions that were distributed over the surface. EDS analysis depicted the presence of Mg, O, and P at the grey areas, implying that this region contains magnesium phosphates and $MgO/Mg(OH)_2$. However, the white regions revealed the presence of Mg, Ca, P, O, and C elements which implied the formation of hydroxyapatite (HA). It was reported by Bakhsheshi et. al., that these products serve as a protective layer which protects the metal substrate from the aggressive solution, thus enhancing corrosion resistance [90]. Additionally, the acid etched MZC exhibited lamellar structures with high concentrations of Mg and Ca. Zhang et al., reported that these lamellar eutectic structures consisted of the $Mg_2Ca$ phase that was primarily responsible for decreasing corrosion resistance of the alloy [170]. This is due to the fact that electrode potential of calcium (- 2.87 V) in the secondary phase ($Mg_2Ca$) leads to a cumulative electrode potential of – 2.54 V which is less than that of magnesium (- 2.37 V). Subsequently, the difference in galvanic potential leads to galvanic corrosion. Zhang et. al., reported a faster rate of corrosion as a result of inter-diffusion of O and Ca via the $Mg_2Ca$ phase [170].

The SEM photomicrographs of Figure 5.11(b) revealed a highly textured surface comprised of laminar $Mg_2Ca$ as result of acid etching whereas the surface of anodized MZC was less textured and exhibited white regions of HA (Figure 5.11(c)). The high corrosion rate of acid etched MZC and the low corrosion rate of anodized MZC corroborate with their surface chemistry, as the secondary phase on the former induces a higher corrosion rate, whereas HA serves as a passivating layer on the latter. Song et al., reported that in the event of failure or breakdown of anodized coating, it will be non-toxic to the human body and the degradation mainly occurs at the damaged area [57].

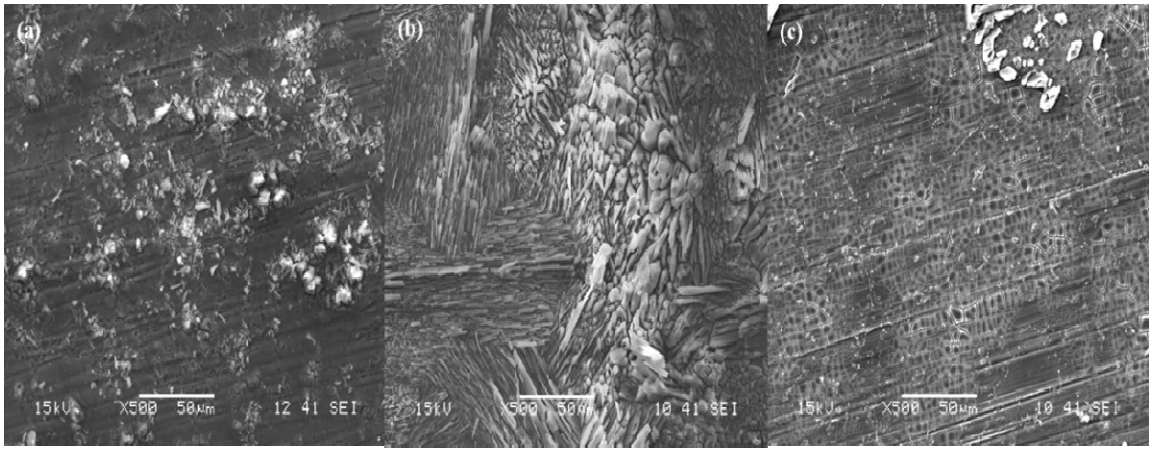


Figure 5.11: SEM photomicrographs of surface treated MZC after corrosion

Figure 5.12 shows the SEM photomicrographs of the surface treated MZC coated with PGCL after corrosion in PBS. The mechanically polished PGCL coated MZC surface in Figure 5.12 (a) revealed that the polymer became delaminated as a result of corrosion. The acid etched PGCL coated MZC revealed bulging of the polymer coating which may be a precursor to delamination that occurred on the mechanically polished MZC. The anodized PGCL coated MZC revealed a polymer coating that was more intact than those on mechanically polished and acid etched MZC. However, there was evidence

of localized defects on the PGCL coating of anodized MZC. Nevertheless, those defects appeared not to have seriously influenced the integrity of the polymer because the anodized MZC coated with PGCL had the lowest corrosion rate as discussed in section (5.4.1.1).

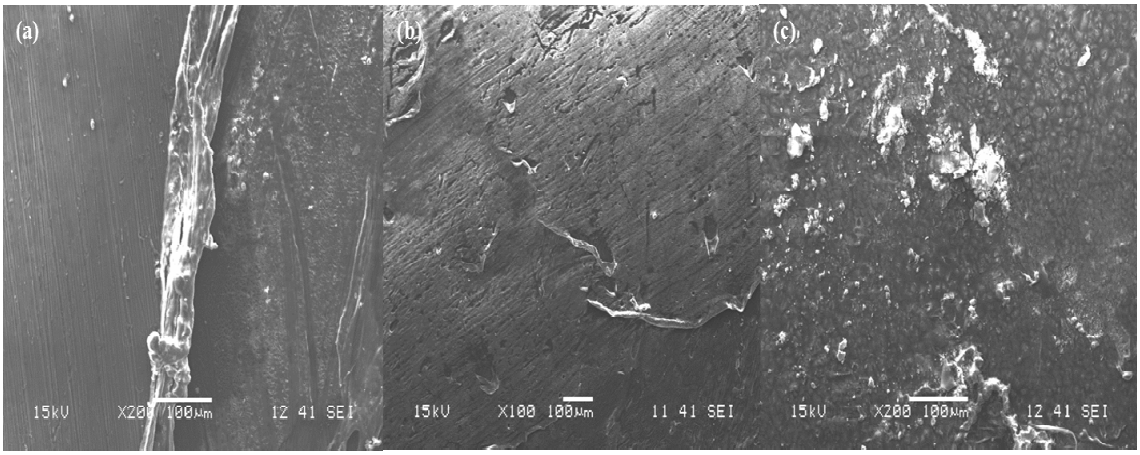


Figure 5.12: SEM photomicrographs of polymer coated MZC samples after corrosion in PBS at 37 $^{o}$C

### 5.5 Electrochemical Impedance Spectroscopy Method

The common approach to study the corrosion performance of a coated magnesium alloy is to investigate the coating stability and the determination when it starts losing its protective properties. After losing coating stability, the corrosion rate would be the same as that of an uncoated metal. One of the most used techniques to investigate the stability of coatings in corrosive environments is the electrochemical impedance spectroscopy (EIS). The impedance (Z) has the same physical meaning as the resistance (R), with the difference that it varies with the frequency (ω) of the applied potential.

While in polarization methods a direct current potential is applied at a constant rate, in impedance measurements a sinusoidal potential variation is applied at different

frequencies ranging from $10^5$ to $10^{-2}$ Hz. This method allows the determination of various contributing of electrical elements such as charge transfer resistance, coating resistance and capacitor resistance to the overall sample resistance (impedance). The determination of these electrical elements can be carried out by simulating the impedance spectra using different circuit models [170, 174, 175].

Figure 5.13 (a) and (b) show two impedance curves of polymer coated magnesium alloy. The spectrum that correlates total impedance with the applied frequency is called Bode plot (Figure 5.13 (a)), while the one which correlates the real and imaginary parts of Z is called Nyquist plot (Figure 5.13 (b)). A plateau in the Bode plot represents a resistance (Z = R when Z does not change with frequency) while the portion of the curve with slope of -1 represents the impedance of a capacitor (the impedance of a capacitor is mathematically defined as: log Z = -log (w) + k, where k is a constant of the material).

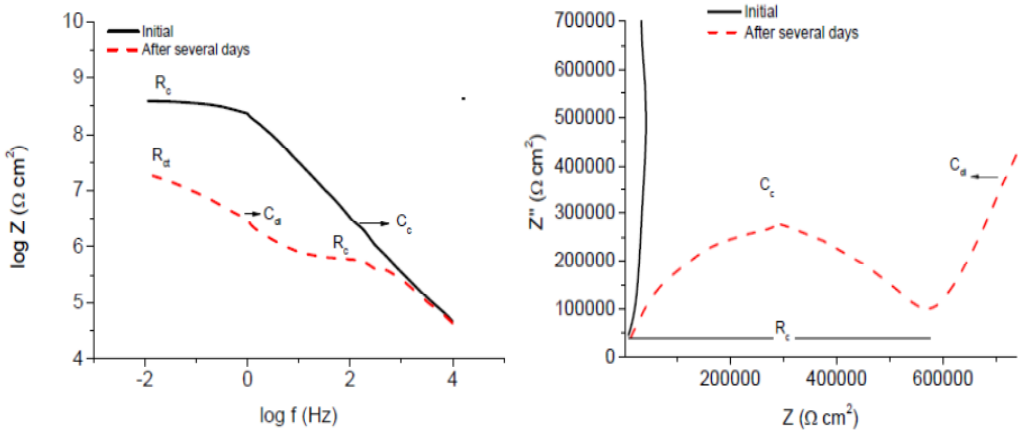


Figure 5.13: Examples of EIS spectra showing (a) the Bode plot and (b) the Nyquist plot

### 5.5.1 Electrochemical Impedance Spectroscopy (EIS) Analysis

The common approach to study the corrosion performance of a coated magnesium alloy is to investigate the coating stability and to determine the conditions and period over which the coating loses its protective properties. It is anticipated that after a coating losses its stability, the rate of corrosion of a coated metal should approach that of the uncoated substrate.

In electrochemical impedance spectroscopy (EIS), the response of an electrode to alternating potential signals of varying frequency (AC voltage) is interpreted on the basis of circuit models of the electrode/electrolyte interface [176]. EIS was used to determine polarization resistance and to model the corrosion process by fitting impedance data with corresponding equivalent circuits (Figure 5.14). The modeling procedure uses electrical circuits built from components such as resistors and capacitors to represent the electrochemical behavior of the coating and the metal substrate. EIS is known to be very useful to evaluate electrochemical performance of coatings, batteries, etc. [141].

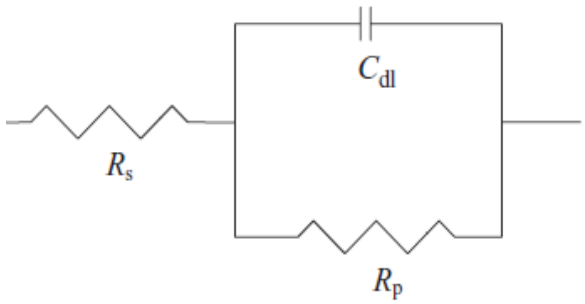


Figure 5.14: Equivalent circuit model used to represent a simple electrochemical interface undergoing corrosion in the absence of diffusion control. Rs – Solution resistance, Rp – polarization resistance, Cdl – capacitance of double layer

In EIS, the impedance of the corroding metal (working electrode) due to an applied sinusoidal potential change (AC voltage) is analyzed as a function of frequency ω. At each frequency, the resulting sinusoidal current waveform and the applied potential are out of phase by phase angle (θ), whereas the current amplitude is inversely proportional to the impedance of the interface [177]. The electrochemical impedance, Z (ω), is the frequency-dependent proportionality factor in the relationship between the voltage signal and the current response,

$$Z(\omega) = E(\omega) / i(\omega) \tag{5.10}$$

where, E is the voltage signal, $E = E_0 \sin(\omega t)$; i is the current density, $i = i_0 \sin(\omega t + \theta)$; Z is the impedance (ohm - $cm^2$); and t is the time (seconds) [176].

Impedance is a complex number that is described by the frequency-dependent modulus, $|Z|$, and the phase angle, θ, or, alternatively, by the real component, $Z'$, and the imaginary component, $Z''$ [177]. In electrochemical impedance analysis, three different types of plots are commonly used. Figure 5.15 depicts the Nyquist plot which shows complex plane $Z''$ vs. $Z'$ and the capacitive arc provides an estimate of corrosion resistance of the material, in terms of its relative diameter, which is directly proportional to the charge transfer resistance or polarization resistance ($R_p$). Thus, an increase in semicircle diameter corresponds to an increase in corrosion resistance [178].

Figure 5.16 depicts the two different Bode plots, showing the impedance magnitude (log Z) vs. log frequency (log f) and the phase angle vs. log frequency [176].

Since real electrochemical processes hardly show pure capacitance, during EIS analysis, the non-ideal response of the corrosion system is represented by a Cc to obtain accurate impedance values [179]. Bryan H et al. [180] has shown that Cc behavior can be attributed to the distribution of physical properties of coatings in a direction normal to the electrode's (substrate) surface. Systems with a Cc element have a Nyquist plot that consists of an arc of a circle with the center somewhere below the x-axis instead of a semicircle, as shown in Figure 5.15. Geometric distributions, such as surface in-homogeneities [181] and porosity of the electrode [182], are known to lead to Cc behavior in EIS measurements.

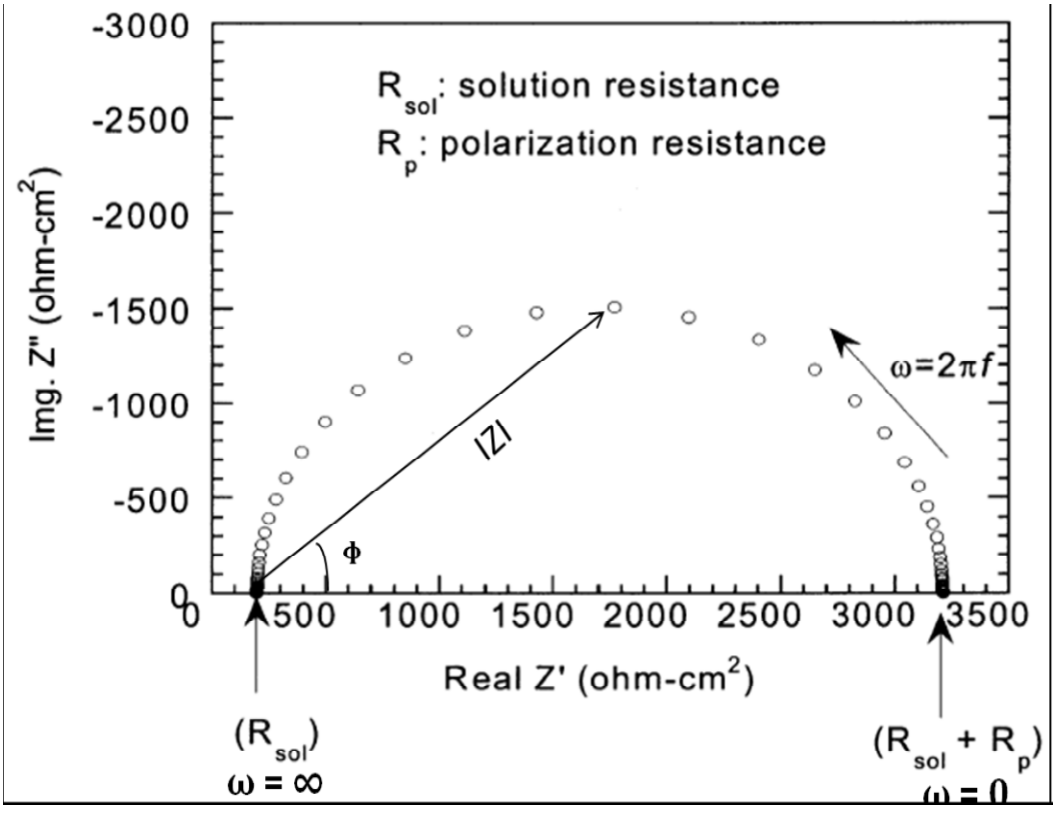


Figure 5.15: A typical Nyquist plot that depicts the real and imaginary impedance values, on the X and Y- axis, respectively, for the aforementioned equivalent circuit

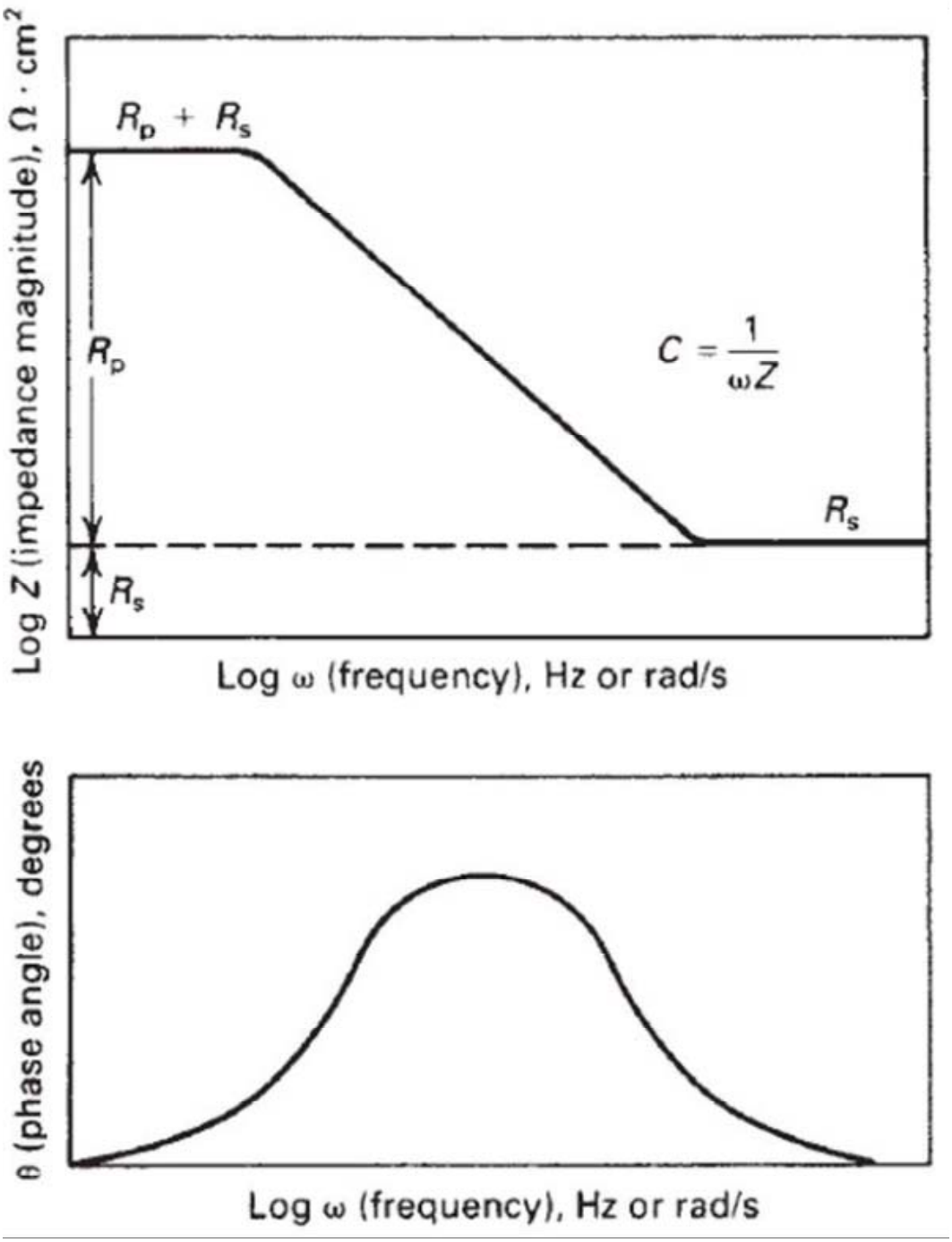


Figure 5.16: A typical Bode plot that shows log frequency on the x-axis, and both the absolute value of the impedance Log Z and phase-shift θ on the y-axis [176] for the aforementioned equivalent circuit.

The two general equivalent circuit models used to represent the bare and PGCL coated MZC in this research are shown in Figure 5.17 and 5.18, respectively.

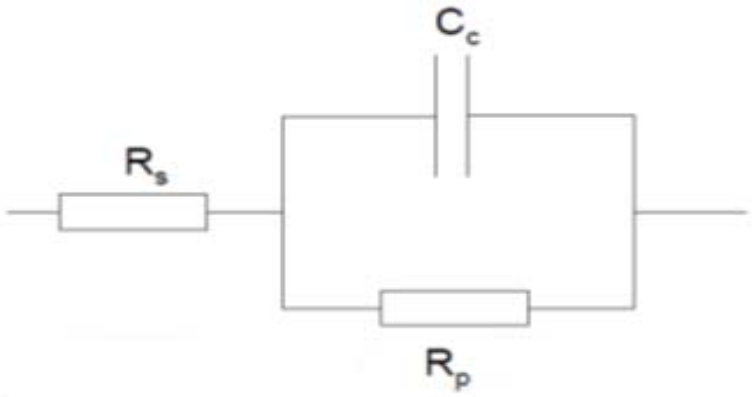


Figure 5.17: Electrical equivalent circuit of a bare MZC

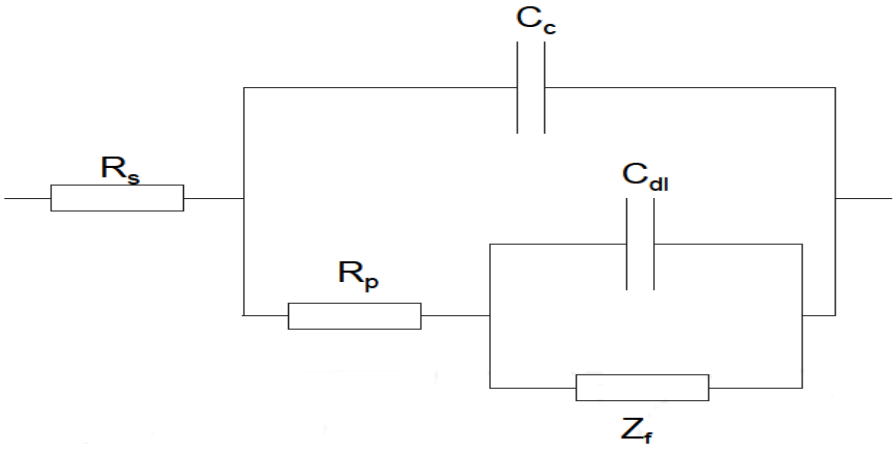


Figure 5.18: Electrical equivalent circuit of MZC with PGCL coating

Parameter $R_p$ coupled with $C_c$, represent the processes that occur at the substrate layer (at the electrolyte/substrate layer interface). $Z_f$ corresponds to the charge transfer resistance associated with the penetration of the electrolyte through the pores or pinholes that exist in the external coating and $R_p$ is the polarization resistance at the electrolyte/substrate interface in the pores. $Q_c$ corresponds to capacitance of the coating

layer and $Q_s$ to the capacitance at the electrolyte/substrate interface, which seems to be associated with the double layer formation [183]. $R_s$ is the ohmic resistance of the electrolyte. The impedance of a constant phase element ($C_c$) Q is given by Equation 5.11 [184]:

$$Q = ZC_c = (1/Y_0)/ (j\omega)^n \quad (5.11)$$

where $Y_0$ corresponds to the admittance of the electrode, j is the imaginary number ($j = \sqrt{(-1)}$), $\omega$ is the angular frequency ($\omega = 2\Pi f$ and f is the frequency) and n (0~1) is an exponential term, which is related to the slope of the log ($Z_{mod}$) vs. log f in Bode plot. $C_c$ has the unit Ss^n (Siemens-second^n). $C_c$ is a mathematical construct that characterizes the response of a process with a constant phase shift over a large frequency range. In Equation 5.11, when n = 1, $C_c$ behaves as a pure capacitor and when n = 0, $C_c$ behaves as a resistor.

### 5.5.1 Electrochemical Impedance Spectroscopy (EIS) Results

Electrochemical impedance spectroscopy (EIS) tests were performed in accordance with ASTM G 3-89 [185] at 37 °C employing a GAMRY® potentiostat (G-750). EIS tests were conducted within a frequency range of 1.0E-02 Hz to 1.0E+05 Hz with 10 points per decade, using PBS as the electrolyte.

Figure 5.19 shows the Nyquist plots of mechanically polished, acid etched and anodized MZC. The capacitive arc provides an estimate of corrosion resistance of the material, in terms of its relative diameter, which is directly proportional to the charge transfer resistance ($R_{ct}$). Thus, an increase in semi-circle diameter corresponds to an

increase in corrosion resistance. The anodized MZC had the highest increase in the diameter of the capacitive arc showing that it had the higher corrosion resistance than mechanically polished and acid etched MZC.

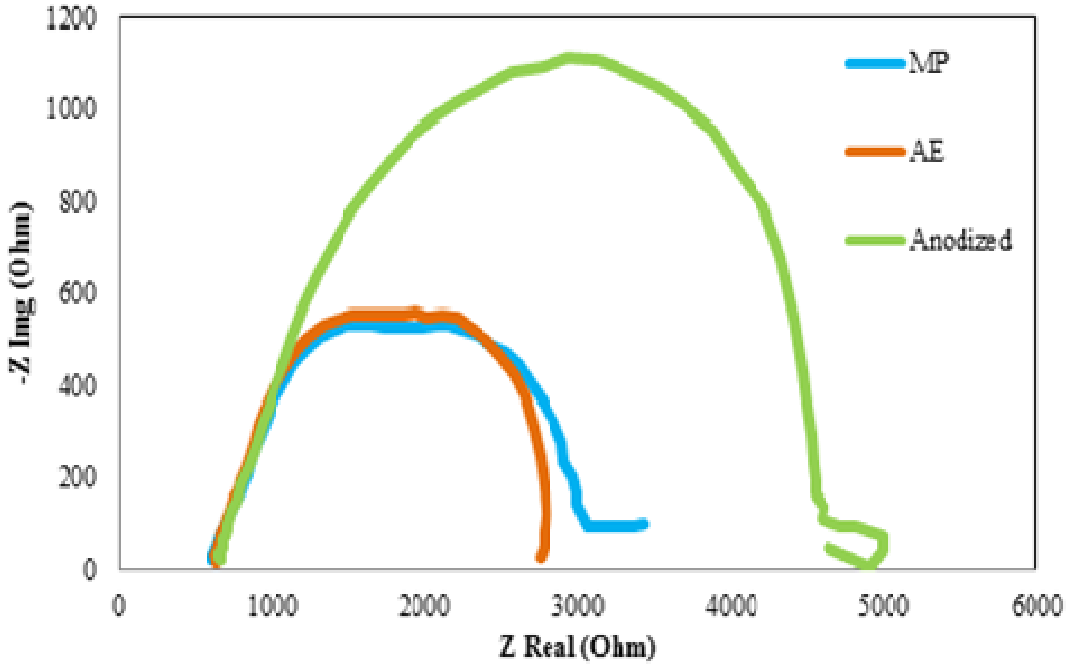


Figure 5.19: Nyquist plots of surface treated MZC

Figure 5.20 shows the bode plot (impedance vs frequency) of surface treated MZC. The impedance spectra showed two time constants. The time constant in the high frequency range corresponded to the resistive and capacitive response of the oxide layer ($R_{oxide}$ and $C_{oxide}$, respectively). The time constant in the low frequency range was attributed to the double layer capacitance at the metal-electrolyte interface, $C_{dl}$ and the corresponding charge transfer resistance. The higher the impedance value, the better is the corrosion resistance of the sample. It can be noted that the anodized MZC showed higher impedance when compared to mechanically polished and acid etched MZC.

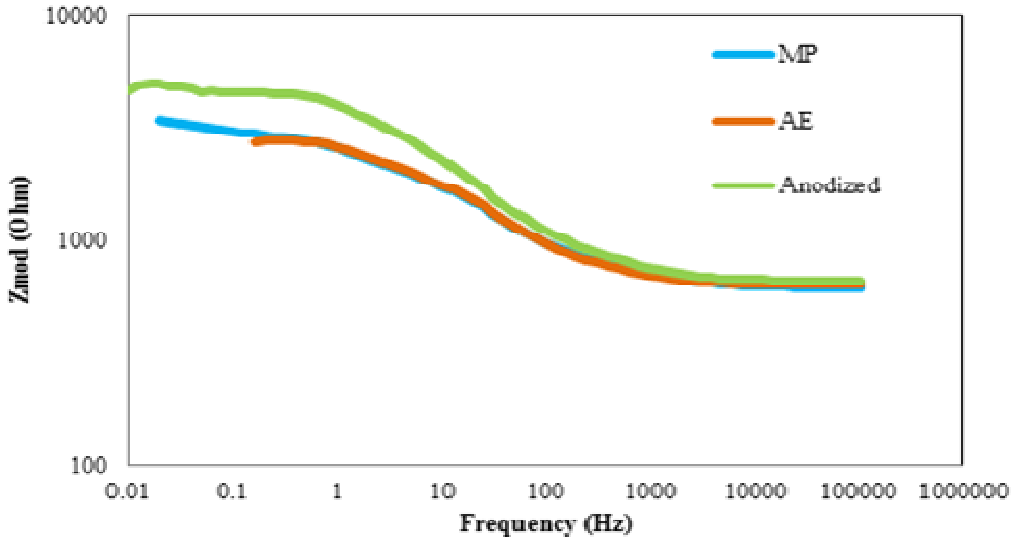


Figure 5.20: Bode plot (phase Vs frequency) for bare MZC alloy in PBS at 37 $^{o}$C

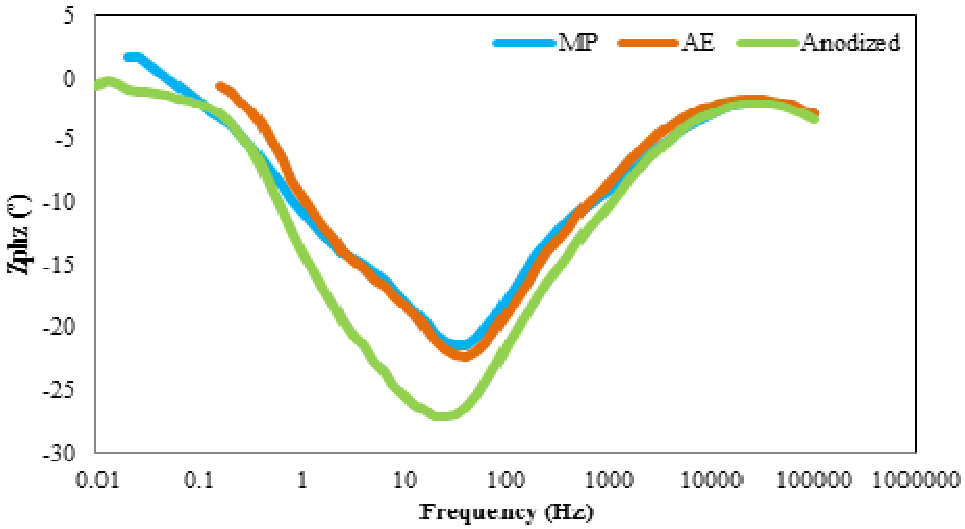


Figure 5.21: Bode plot (impedance Vs frequency) for bare MZC alloy in PBS at 37 $^{o}$C

Figure 5.21 shows the bode plot (phase vs frequency) of surface treated MZC. The degree of phase shift is a function of the type and proportion of protective layer produced on the surface of the alloys. The anodized MZC produced a phase shift at a lower frequency (~ 29.99 °) when compared to mechanically polished and acid etched

MZC. This was attributed to the presence of a thick and dense oxide layer which imparted surface passivation.

Figure 5.22 shows the equivalent circuit of surface treated MZC, where $R_s$ represents the resistance of the electrolyte, $R_p$ is the resistance of the pore and crack walls in the outer porous layer in parallel with $Y_s$. $Y_s$ is the capacitance associated with the electrolyte double layer established at the interface.

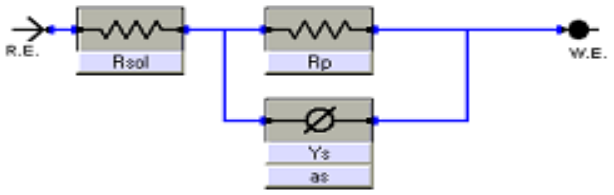


Figure 5.22: Equivalent circuit of the corrosion cell for surface treated MZC

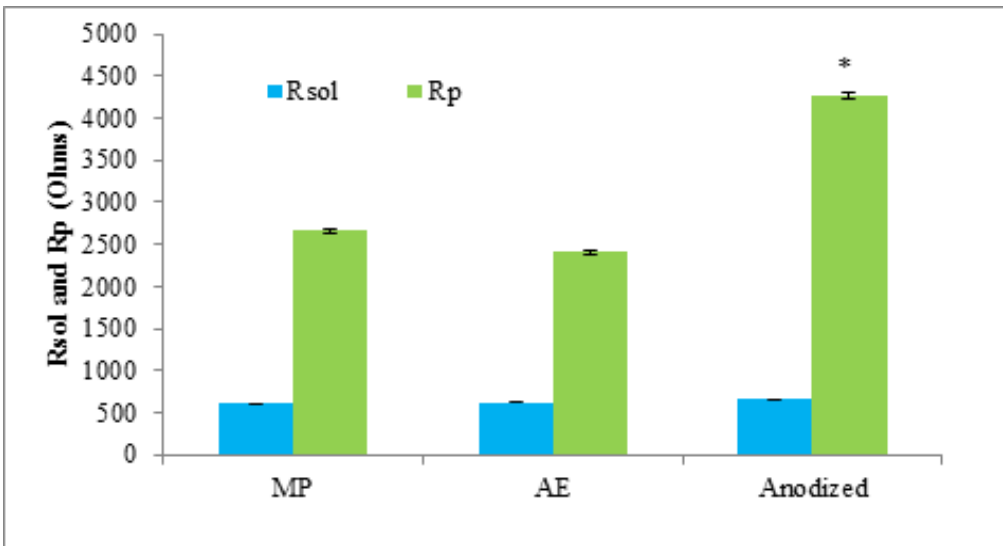


Figure 5.23: Equivalent circuit parameters for surface treated MZC (mean ± SD, n = 3)

Note: * refers to $p < 0.05$ indicating values are significantly different from mechanically polished MZC in one-way ANOVA analysis

From Figure 5.23, it can be observed that $R_p$ of anodized MZC was higher as compared with those of mechanically polished and acid etched MZC which was attributed to the protective dense oxide layer on anodized MZC.

Figure 5.24 represents the Nyquist plots of the surface treated MZC that were PGCL coated where the impedance magnitude of anodized MZC coated with PGCL was greater than that of the mechanically polished counterpart. As previously mentioned in section (5.4.1.1) anodization and PGCL coating together enhanced the corrosion resistance of MZC.

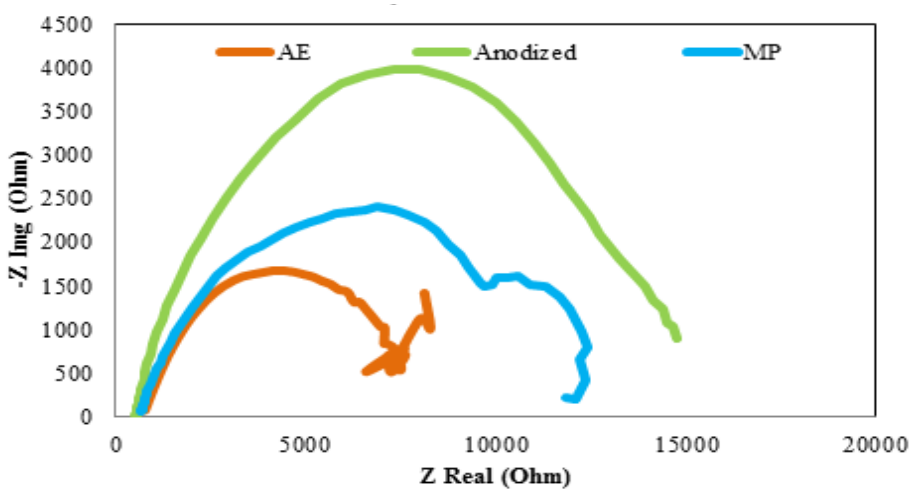


Figure 5.24: Nyquist plots of PGCL coated MZC in PBS at 37 $^{o}$C.

Impedance magnitude of acid etched PGCL coated MZC was less than both MP and anodized counterparts. It should be noted that the mechanically polished PGCL coated MZC displayed two distinct capacitance loops (semi-circles) which correspond to the coating capacitance and interfacial capacitance (double layer capacitance). The first capacitive loop represents the pore resistance and the second loop represents the establishment of a new surface coating.

Figure 5.25 shows the bode plot (phase vs frequency) of PGCL coated: mechanically polished, acid etched and anodized MZC. The higher the impedance value, the better is the corrosion resistance of the sample. Thus, it can be observed that the impedance magnitude of anodized PGCL coated MZC was higher than that of the mechanically polished and acid etched counter parts.

Figure 5.26 shows the bode plot (phase vs frequency) of PGCL coated surface treated MZC. The degree of phase shift was a function of the type and proportion of protective layer produced on the surface of the alloys. The anodized MZC produced a phase shift at a lower frequency (~ -43 °) when compared to mechanically polished and acid etched MZC. This was attributed to the presence of a thick and dense oxide layer along with PGCL coating which imparted surface passivation.

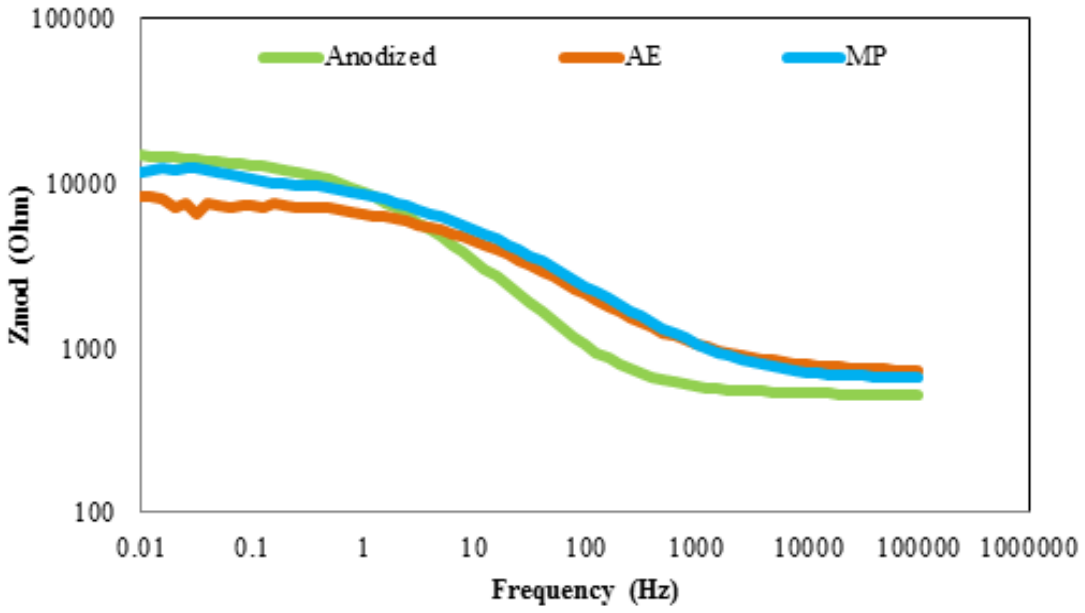


Figure 5.25: Bode plot (impedance modulus vs frequency) for PGCL coated MZC

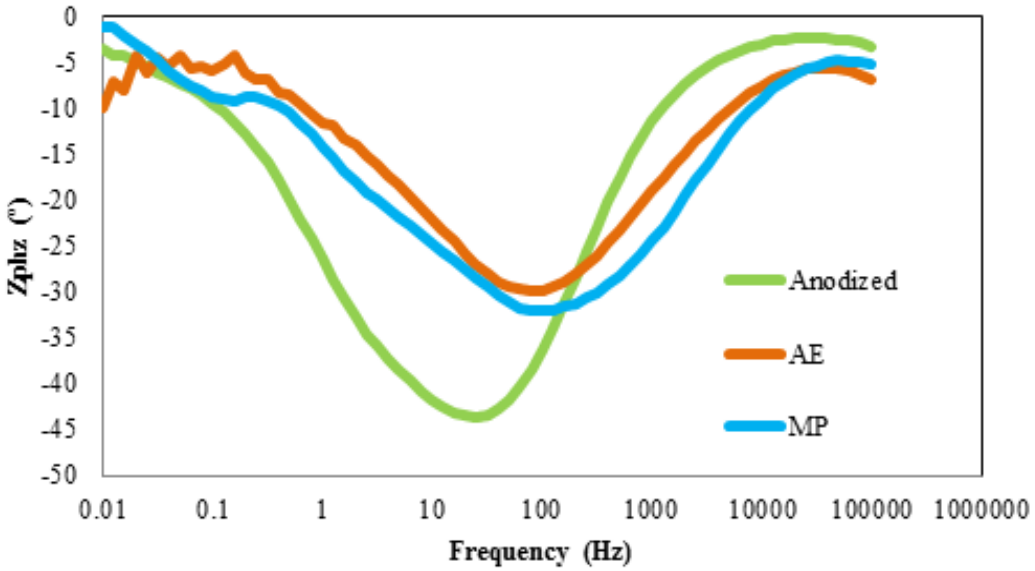


Figure 5.26 : Bode plots (phase vs frequency) for PGCL coated MZC

Figure 5.27 is the equivalent circuit of the PGCL coated surface treated MZC, where $R_p$ coupled with substrate represent the processes that occur at the substrate layer (at the electrolyte/substrate layer interface).

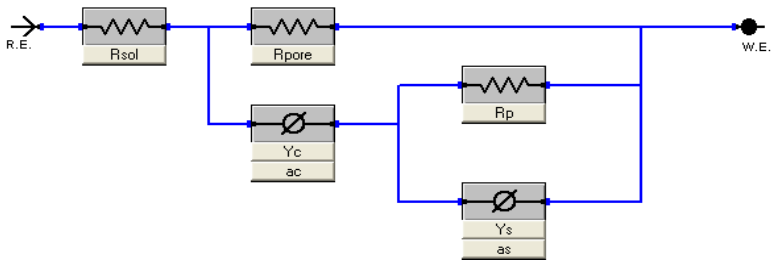


Figure 5.27 : Equivalent circuit for filmed corrosion surfaces

$R_{pore}$ corresponds to the charge transfer resistance associated with the penetration of the electrolyte through the pores or pinholes that exist in the external coating and $R_p$ is the polarization resistance at the electrolyte/substrate interface in the pores. $Y_c$ corresponds to capacitance of the coating layer and $Y_s$ to the capacitance at the

electrolyte/substrate interface, which appears to be associated with the double layer formation [109, 115]. $R_{sol}$ is the ohmic resistance of the electrolyte.

The higher is the resistance $R_{pore}$, the higher is the protective effect of the polymer coating [117]. From Figure 5.28, it can be observed that $R_{pore}$ and $R_p$ of PGCL coated anodized MZC were higher than those of mechanically polished and acid etched counter parts. This result also corroborates with the corrosion rates determined by potentiodynamic polarization and SEM/EDS analyses as discussed in sections (5.4.1.1) and (5.4.1.2).

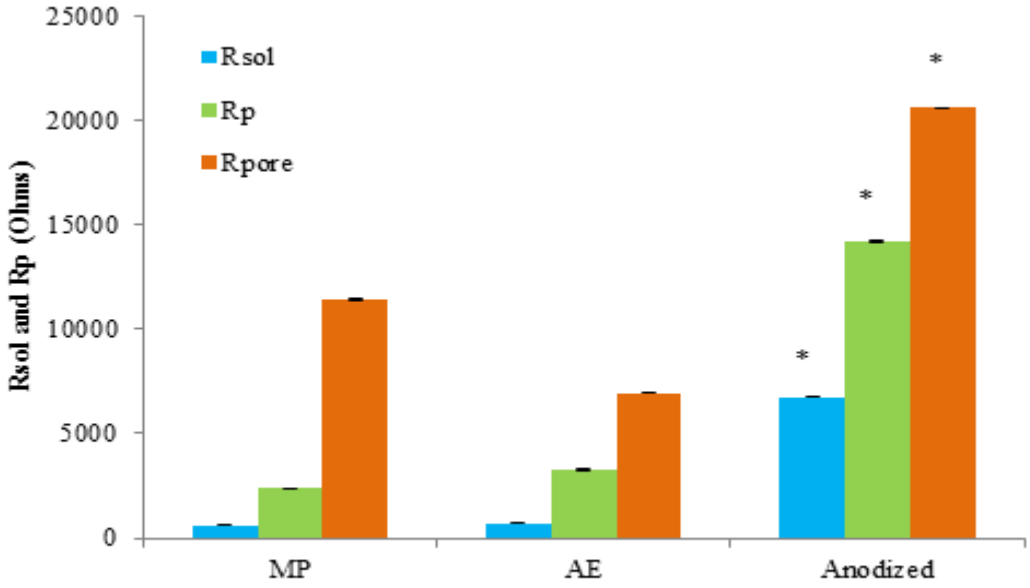


Figure 5.28: Equivalent circuit for filmed corrosion surfaces (mean ± SD, n = 3)

Note: * refers to $p < 0.05$ indicating values are significantly different from mechanically polished MZC in one-way ANOVA analysis.

# 6. BIOCOMPATIBILITY STUDIES

The objective of this research is to retard the initial corrosion of MZC without impairing its mechanical and biocompatible properties for cardiovascular stent applications. As detailed in chapter 5, investigations on the corrosion of MZC in PBS revealed that surface treatment and coating of the alloy with PGCL decrease the rate of corrosion. Because corrosion in turn, influences biocompatibility, it was imperative to assess the biocompatibility of the surface treated and PGCL coated MZC.

Biocompatibility is the capability of a material to coexist with living tissues or organisms without any deleterious effect. As a result, the interaction of the implant materials with the surrounding cells determines their biocompatibility [77]. Biocompatibility of an implant material depends on surface properties such as surface morphology, material composition, wettability and surface charge and in the case of bio-absorbable MZC, the nature and thickness of the passivating layer.

There are several methods to measure the biocompatibility of a material that require *in-vitro* or *in-vivo* processes. In the current research, *in-vitro* endothelial cell viability and hemocompatibility by platelet (from porcine blood) adhesion were conducted in accordance with ISO 10993 and ISO 10993-4 respectively.

Cytotoxicity of the MZC was measured in terms of endothelial cell viability in the presence of PBS corrosion extracts containing leached ions (Mg, Ca and Zn) obtained from potentiodynamic polarization tests as detailed in section 5.4.1.1. Usually, the type of cell chosen for experimentation is based on the typical application of the material being tested. Endothelial cells were chosen because they are associated with restenosis and thrombosis complications that sometimes arise after angioplasty.

During the implantation of cardiovascular stents via angioplasty, arterial injury at the implant location damages the endothelium layer, exposing the sub-endothelial matrix. This results in intimal hyperplasia, a physiological healing response after damage to blood vessels that causes thickening of the walls. This in turn leads to restenosis or narrowing of blood vessel with more than 50% luminal closure. Restenosis occurs in 15% - 20% of patients within 3 to 6 months after stent implantation. Stent struts that lacked endothelial coverage revealed focal aggregates of platelets and inflammatory cells [186]. Thus, platelet adhesion has the potential to form thrombus [186]

During and immediately following stent implantation, disruption of the endothelial layer can trigger the adhesion of proteins, such as fibrinogen, fibronectin, vitronectin, immunoglobulin and von Willebrand factor (vWF) (a blood glycoprotein) onto the newly exposed sub-endothelial layer. This ultimately leads to activation, adhesion and deposition of platelets [207, 210, 211], and subsequently to thrombus formation. Figure 6.1 shows the sequence of platelets adhering to the walls of a blood vessel where there are no endothelial cells. According to Simionescu et al. an ideal biomaterial used for cardiovascular implants is expected to withstand such thrombus formation as well as inflammatory host responses, at least until a *de novo* superficial endothelial layer is formed [187]. The primary objective of this research was for MZC to ensure affluent endothelial cell growth but with minimum platelet adhesion.

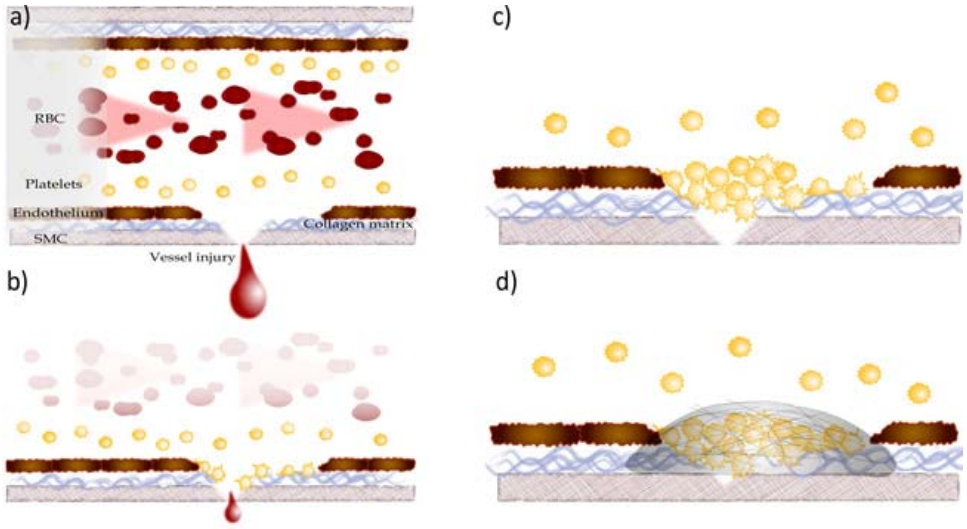


Figure 6.1: The sequential events following lack of endothelial cells

### 6.1 Cytotoxicity of Leached Ions on Endothelial Cell Viability

Cytotoxicity, which is an integral component in assessing the biocompatibility of implant materials. There are three methods to conduct cytotoxicity tests, namely extract dilution method, indirect contact method and direct contact method [188], which enables even weak cytotoxicity to be detected because of its high sensitivity [189]. The extract dilution method is more commonly adopted for *in-vitro* cytotoxicity tests for the evaluation of implant materials and devices, since it can be applied to a wide variety of raw materials and finished products that may release toxins from exposed surfaces [190]. The most commonly used test in the extract dilution method to quantify cytotoxicity of cells is the SRB assay test. The cell type chosen in these assays is usually based on the typical application for which the tested material is used. For example, endothelial cells are preferred for SRB assays if the intended use of the material is for the manufacture of cardiovascular stents.

In this investigation, SRB Assay was conducted by taking extracts of PBS remaining in the corrosion cell after potentiodynamic polarization tests with MZC as the working electrode. Before conducting the cytotoxicity test, the concentration of leached metal ions in the PBS was analyzed using inductive coupled plasma mass spectroscopy (ICP-MS).

## 6.2 Inductive coupled plasma mass spectroscopy (ICP-MS)

ICP-MS was performed using a Perkin Elmer Sciex (model ELAN DRC-II) equipped with mass spectrometer. The ICP-MS utilized an integrated circuit/radio frequency (IC/RF) power of 1300, nebulizer gas flow of 0.92 L/minute, plasma gas flow of 16 L/minute and lens voltage of 10.5 V. ICP-MS. PBS from three corrosion tests were combined and a 5ml aliquot was filtered to remove any precipitate prior to analysis.

### 6.2.1.1 ICP-MS Results

A comparison between the average concentrations of dissolved metal ions (Mg, Ca and Zn) in PBS after corrosion tests with bare metal MZC and surface treated MZC coated with PGCL are displayed in Figure 6. 2. These results indicated that the PBS with bare metal MZC that was acid etched had the highest concentration (~1758.1 ppb) of $Mg^{2+}$ ions as compared with that from the mechanically polished (~1442.9 ppb) and anodized (~1129 ppb) MZC. The elevated $Mg^{2+}$ ion content was attributed to galvanic corrosion induced by the presence of secondary phases ($Mg_2Ca$) as previously discussed. The lowest concentration $Mg^{2+}$ ions (~1129.2 ppb) leached into PBS was attributed to the presence of a protective oxide/hydroxide layer on the anodized MZC. The role of the oxide/hydroxide on anodized MZC is discussed in sections 4.2 and 4.4 as well as in section 5.4.1.1.

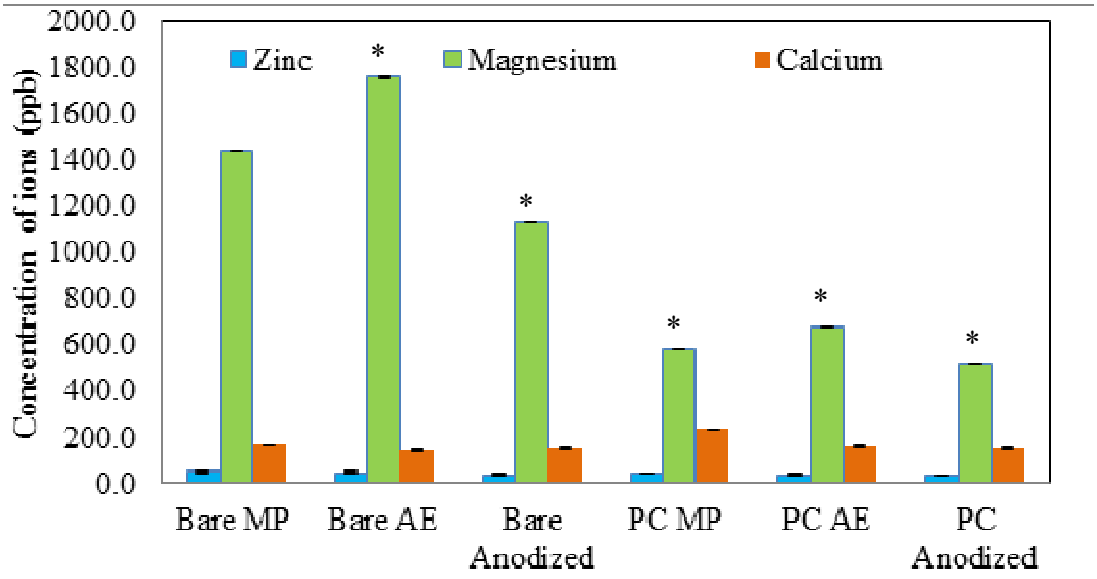


Figure 6.2: Comparison of concentrations of Mg, Zn and Ca ions in PBS after corrosion (mean ± SD, n = 3)

Note: * refers to $p < 0.05$ indicating values are significantly different from mechanically polished MZC in one-way ANOVA analysis

The ICPMS results of surface treated MZC coated with PGCL revealed significantly less $Mg^{2+}$ ions in the PBS after corrosion of acid etched (~585.1 ppb), mechanically polished (~681.1 ppb) and anodized (~516 ppb) MZC as compared with that in PBS from tests with bare metal surface treated MZC. This indicated that the PGCL coating provided an additional protective layer from the physiological environment that lead to a reduction in the rate of corrosion. Nevertheless, the same trend in $Mg^{2+}$ion concentration in the PBS after corrosion tests was obtained irrespective of whether bare metal MZC or PGCL coated MZC was used as the working electrode. It should be noted that the oxide/hydroxide and PGCL create chemical and physical barriers against ion diffusion to

and from the MZC substrate. Other researchers have reported that the metal ion release is not only related to the chemical composition of the alloy but also dependent on the compactness, stability, thickness of polymer/oxide coating and regeneration potential of the oxide film [191]. In conclusion, the ICPMS results directly correlate with corrosion rates determined in this investigation and the PGCL coated anodized MZC possess the highest corrosion resistance.

Elevated $Zn^{2+}$ ions have been reported to induce disruption of mitochondrial function at an equilibrium concentration of 10 $*10^4$ ppb and can lead to cell death [192]. In the current study, a concentration of 30-55 ppb of $Zn^{2+}$ ions were detected in the PBS after corrosion, which is significantly less than that associated with disruption of mitochondrial function and cell death. Similarly, the concentration of $Ca^{2+}$ ions in the PBS after corrosion was 100 -200ppb, which is well below the concentration that may pose any imbalance in the $Ca^{2+}/Mg^{2+}$ equilibrium described in section 2.1. Thus, the concentration of dissolved metal ions released from MZC should not have any deleterious effect on cells and may have beneficial effects on cells and local tissues [74].

### 6.2.2 Cell Culturing and Media for SRB Assay

Human Primary Umbilical Vein Endothelial Cells - HUVEC (ATCC® PCS-100-010™), obtained in a frozen state, were thawed to room temperature before culturing them. The cell culture media as recommended by the ATCC company was prepared by thawing and mixing one Endothelial Cell Growth Kit-VEGF (ATCC® PCS-100-041™) into one bottle of Vascular Cell Basal Medium (ATCC® PCS-100-030™) under aseptic conditions and in a fume hood. The cells along with cell culture media were placed in a

75ml flask and incubated at 37 $^0$C at 5% $CO_2$. The cell culture medium was changed in the flask after every 48 hours to remove the dead cells and provide sufficient nutrients for the existing cells. Once the cells reached confluency in the cell culture flask, they were tripsinized after approximately 7 to 8 days. These cells were subsequently utilized in cytotoxicity evaluation and cell growth tests.

### 6.2.3 Cytotoxicity (SRB assay) Protocol

A sulforhodamine B (SRB) assay (*In-vitro* Toxicology Assay Kit, Sulforhodamine B based-TOX6, Sigma-Aldrich, Saint Louis, MO) was conducted to assess cell viabilityin the presence of metal ions leached during potentiodynamic polarization tests of MZC samples. The PBS obtained after the corrosion tests (section 5.4.1.1) were filtered using a 0.2 micron filter, and 10% Fetal Bovin Serum, 1% penicillin and 0.3mg/L G418 powder were added. A 96 well-plate was used for seeding the HUVEC cells in which 200 µl of cell suspension of optimum density (20,000 cells/well or 1 x $10^5$ cells/ml) was used in each well. After 24 hours of incubation, the cell culture medium in the wells was removed and replaced by various proportions of cell culture medium and PBS (electrolyte after corrosion) to produce the following: 10% corrosion electrolyte and 90% cell culture media; 50% corrosion electrolyte and 50% cell culture medium. Finally 100% corrosion electrolyte and 100% cell culture medium as a control. At the end of 48-hour incubation period, 50 µL of cold (4 °C) 50% TCA was added to 200 µL of the liquid already present in each well. The well plate was left at room temperature for 30 minutes for the HUVEC cells to be fixed to the well plate. The TCA was removed from the wells and the well plate was rinsed using tap water at least 5 times and allowed to dry overnight. 100 µL of

0.4% (w/v) sulforhodamine B (SRB) dissolved in 1% acetic acid solution was added to the wells (staining of the cells). The greater the number of endothelial cells, the greater the amount of SRB dye (negatively charged pink color aminoxanthine dye) bound to the amino acids of endothelial cells [193]. The wells were then placed in an incubator for 30 minutes. After the staining period, the wells were rinsed with 1% v/v acetic acid at least 4 times to remove the unbound SRB dye and then allowed to dry. 200 µL of 10mM Trizma Base solution was added into each well to solubilize the bound SRB dye. The fluorescence of the viable cells was determined by placing the 96 well plate into a multiplate reader (TECAN GENios multiplate reader,Tecan, Männedorf, Schweiz) to obtain SRB readings of absorbance. Before obtaining the readings, the well plate was shaken for 5 minutes, by the plate reader. Additionally, these SRB assays were repeated on the aforementioned liquids, for a duration of 4 and 7 days, to determine the prolonged effects of these corrosion liquids on HUVEC cells. Absorbance values were subsequently presented in the form of normalized cell proliferation values with respect to a negative control (absorbance of cells grown in cell culture media alone).

### 6.2.4 Cytotoxicity Test Analysis (SRB Assay Test Analysis)

Endothelial cells were grown in the presence of dissolved ions present in the PBS collected after corrosion of surface treated and PGCL coated surface treated MZC. Cell viability was evaluated after 2, 4 and 7 days.

Figures 6.3 to 6.5 illustrate the cytotoxic behavior of corrosion extracts. All samples exhibited a gradual increase in cell growth in extracts of 10%, 50% and 100% over periods of 2, 4 and 7 days. These results can further be supported by ICP-MS analysis

(previous section, Table 6.1) that all the MZC had similar and low concentrations of Zn and is mainly Mg and Ca, which could have helped cells to sustain good health at day 7 with no cell culture media. However, there was a ~30% decrease in the net growth rate of cells exposed to 50% corrosion extract after day 4; and an increase after day 7. This increase at day 7 for 50% could be the time required for the cells to adjust to new environment. Cells exposed to 100% corrosion extract exhibited a slight increase in net growth rate over time.

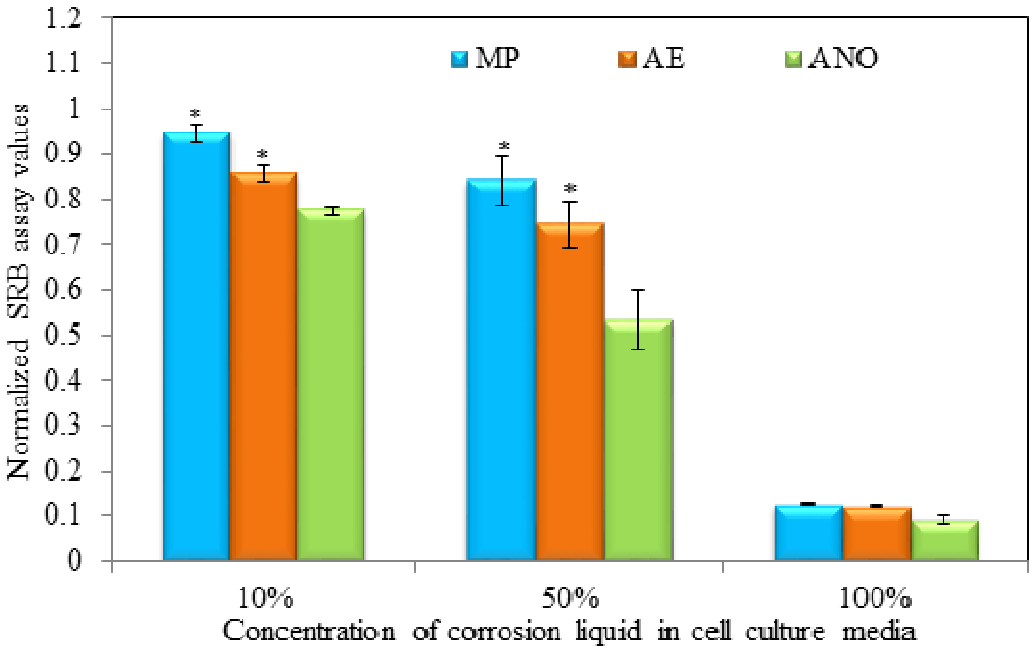


Figure 6.3: Net growth rate of HUVEC cells after 2 days of exposure to leached ions from potentiodynamic corrosion tests of uncoated MZC (mean ± SD, n = 3)

Note: * refers to $p < 0.05$ indicating values are significantly different from anodized MZC in one-way ANOVA analysis

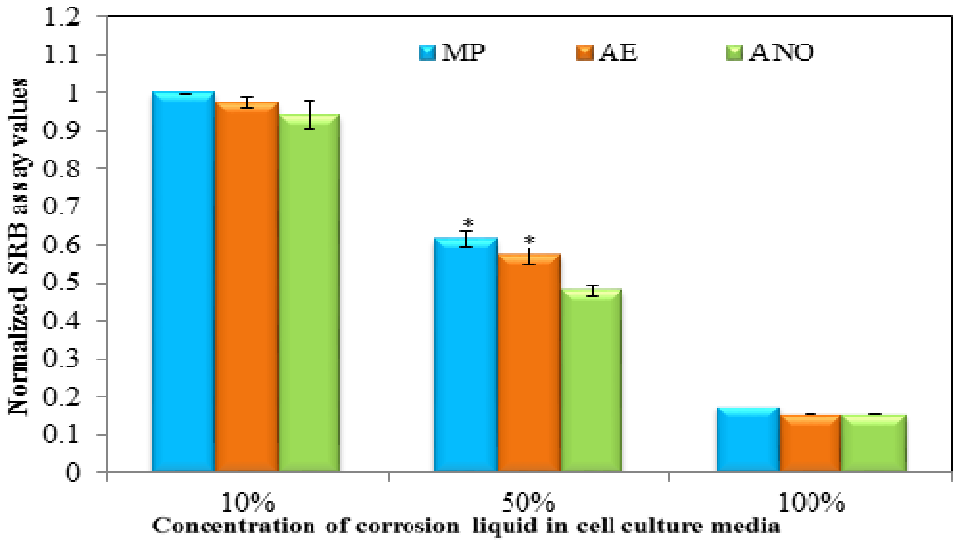


Figure 6.4: Net growth rate of HUVEC cells after 4 days of exposure to leached ions from potentiodynamic corrosion tests of uncoated MZC (mean ± SD, n = 3)

Note: * refers to $p < 0.05$ indicating values are significantly different from anodized MZC in one-way ANOVA analysis

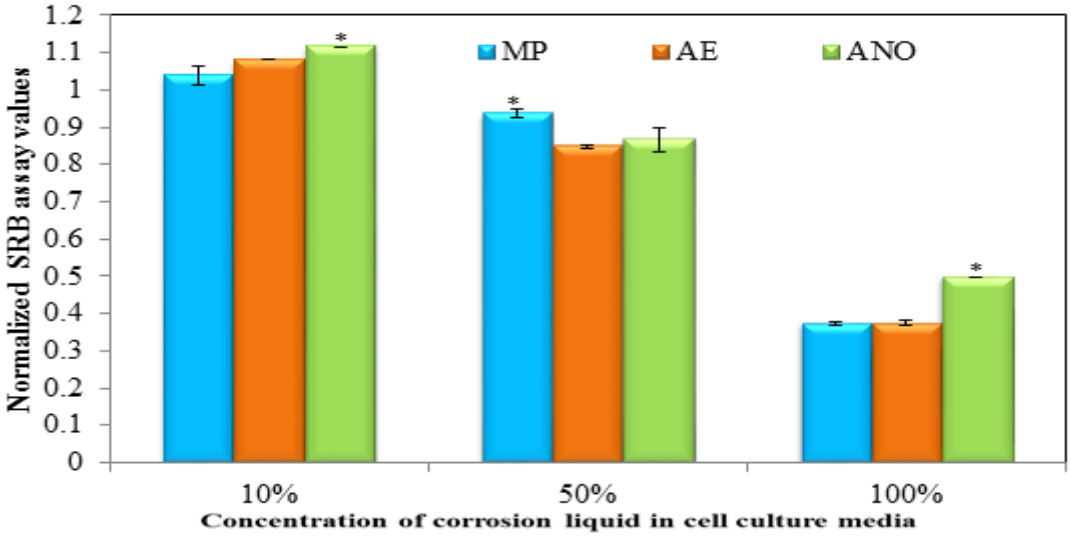


Figure 6.5: Net growth rate of HUVEC cells after 7 days of exposure to leached ions from potentiodynamic corrosion tests of uncoated MZC (mean ± SD, n = 3)

Note: * refers to $p < 0.05$ indicating values are significantly different from anodized MZC in one-way ANOVA analysis

Figures 6.7 to 6.9 illustrate the cytotoxicity behavior of corrosion extracts obtained from *in-vitro* potentiodynamic analysis of PGCL coated MZC in PBS at 37 °C.

Endothelial cells grown in the presence of dissolved ions of corrosion extract from PGCL coated MZC in PBS at 37 $^{o}$C evaluated after 2, 4 and 7 days showed an increase in cell growth when compared to uncoated MZC, which is comparable for control in 10% and 50% extracts for the periods of 2, 4 and 7 days. These results can further be supported by ICP-MS analysis that all the MZC samples had similar and low concentrations of Zn and is mainly Mg and Ca, which could have helped cells to sustain good health at day 7 with no cell culture media. Cells exposed to 10%, 50% and 100% corrosion extract exhibited a slight increase in net growth rate over time.

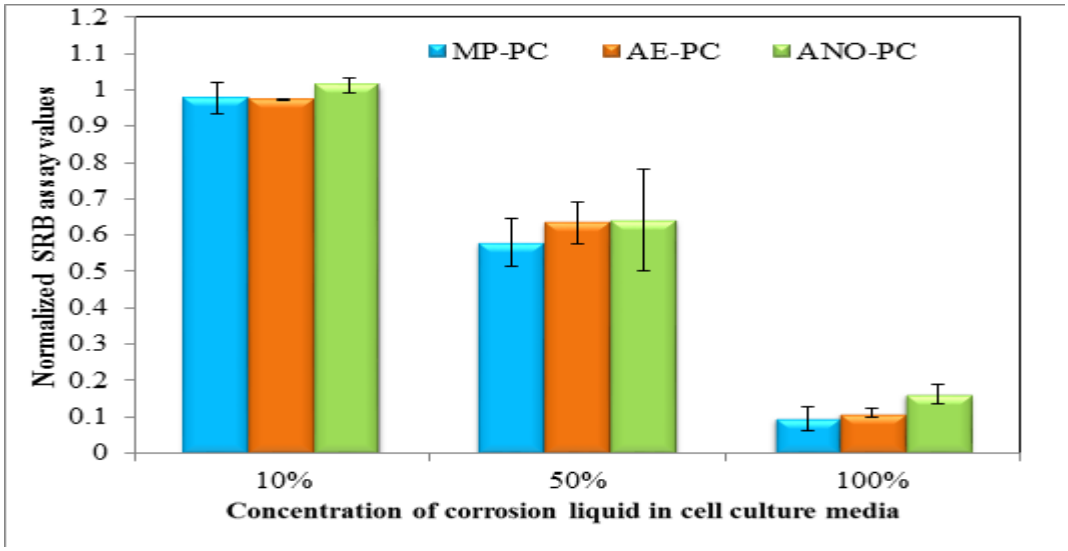


Figure 6.6: Net growth rate of HUVEC cells after 2 days of exposure to leached ions from potentiodynamic corrosion tests of polymer coated MZC (mean ± SD, n = 3)

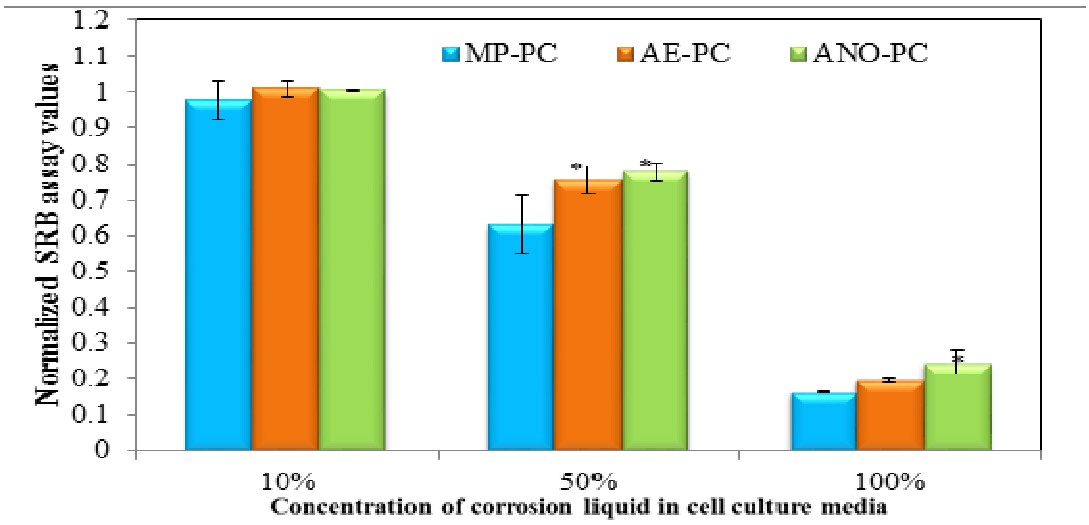


Figure 6.7: Net growth rate of HUVEC cells after 4 days of exposure to leached ions from potentiodynamic corrosion tests of polymer coated MZC (mean ± SD, n = 3)

Note: * refers to $p < 0.05$ indicating values are significantly different from mechanically polished MZC in one-way ANOVA analysis

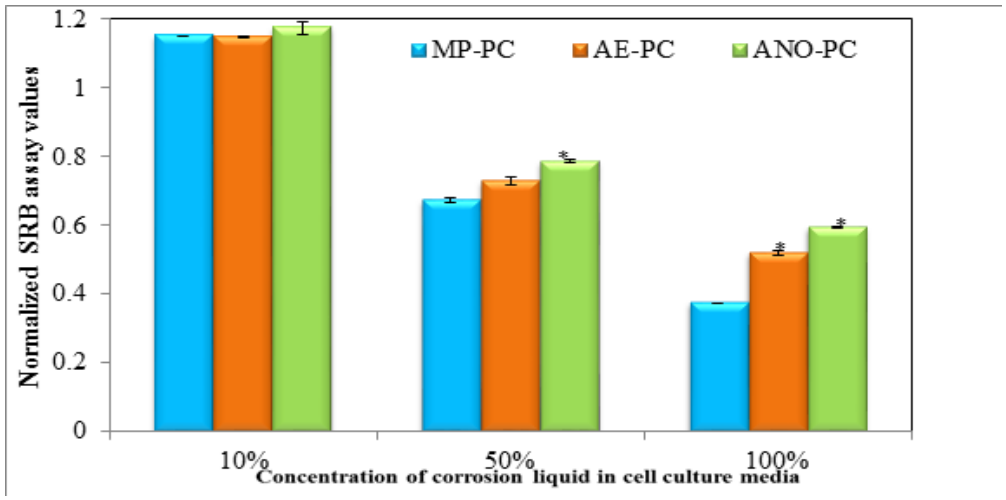


Figure 6.8: Net growth rate of HUVEC cells after 7 days of exposure to leached ions from potentiodynamic corrosion tests of polymer coated MZC (mean ± SD, n = 3)

Note: * refers to $p < 0.05$ indicating values are significantly different from anodized MZC in one-way ANOVA analysis

### 6.3 Hemocompatibility

In general, implants with surfaces in contact with blood can initiate activation, secretion, adherence, and aggregation of platelets and trigger subsequent plasmatic coagulation and immunological responses, depending on the material's hemocompatibility [207]. Spreading of platelets and the secretion of their stored constituents lead to further platelet aggregation [208]. Hemocompatibility of a cardiovascular implant material plays a major role in its thrombogenicity. Surface properties of a material mainly control its hemocompatibility which can be understood by investigating the affinity of various blood components (platelets, fibrinogen, etc.) towards its surface.

Hemocompatibility is the measure of evaluating materials compatibility with blood. *In-vitro* methods of testing hemocompatibility of a material are beneficial than in vivo methods because small levels of plasma hemoglobin that may not be measureable under *in-vivo* conditions can be quantified in these methods. Generally, hemocompatibility is measured with reference to platelets, coagulation, thrombosis, hematology, and immunology. ISO 10993–4 was utilized to evaluate the hemocompatibility of biomaterials for medical devices. According to ISO 10993-4 some blood interactions with the material that would be considered undesirable to the body are: activation and adhesion of platelets, formation of thrombus, injury to circulating cells and injury to cells or tissues. Sheppard et al. (1994) reported that all blood interactions are important because they are a series of events that potentially lead to the formation of a thrombus (thrombosis) [194].

### 6.3.1 Thrombosis

Thrombosis is the formation of a blood clot inside a blood vessel, obstructing the blood flow through the circulatory system. When a blood vessel is injured, the body uses platelets (thrombocytes) and fibrin to form a blood clot to prevent blood loss. It was reported by et al. that the primary cause of stent access failure in dialysis patients is due to thrombosis (~0.5 to 0.8 episodes/year/patient) [195, 196]. In general, implants with surfaces in contact with blood flow can initiate activation, secretion, adherence, aggregation of platelets and trigger subsequent plasmatic coagulation, and immunological responses, depending on the material's hemocompatibility [197]. Spreading of platelets and the secretion of their stored constituents lead to further platelet aggregation [198]. Indeed, blood contacting devices are prone to clotting and inflammatory responses, which impair their performance and can be detrimental to patients. For example, the migration of thrombus to vasculature within the brain may lead to stroke and in some cases, even death.

During and immediately following stent implantation, disruption of the endothelial layer can trigger the adhesion of proteins, such as fibrinogen, fibronectin, vitronectin, immunoglobulin and von Willebrand factor (vWF) (a blood glycoprotein) onto the newly exposed sub-endothelial layer. This ultimately leads to activation, adhesion and deposition of platelets [197, 199, 200], and subsequently to thrombus formation. In the case of a biomaterial, when it is exposed to blood, a rapid adsorption of plasma proteins will occur. Adsorption of higher amounts of fibrinogen on the surface of biomaterial renders increased thrombogenicity, whereas adsorption of higher amounts of albumin convert it into a hemocompatible surface [201]. An ideal biomaterial used for

cardiovascular implants is expected to withstand such thrombus formation as well as inflammatory host responses at least until a *de novo* superficial endothelial layer is formed. In the case of metallic implant materials, properties such as surface free energy, surface charge [202-204], roughness, wettability, surface composition (oxide layer, functional groups) [205], metal ion leaching and corrosion resistance ultimately affect their interaction with the surrounding blood proteins, platelets and extracellular material [206, 207].

In the case of cardiovascular stents, thrombogenicity is dependent on intrinsic properties, such as corrosion resistance, hemocompatibility and mechanical dexterity. However, the extrinsic properties of a stent, such as its dimensions, design, combination of the drug and polymer coating affect its thrombogenicity via platelet activation [208-212]. Additionally, its placement relative to the vessel wall, which imposes specific flow disruptions such as stagnation and recirculation, also has a similar effect. Activation is immediate and reaches a maximum state ~ 2 to 4 hrs following implantation of the device [213].

### 6.3.2 Platelet Adhesion Test

Platelet adhesion results in harmful thrombus formation. The more the platelet adhesion the less is hemocompatibility of the alloy. In current research hemocompatibility of the alloy was evaluated by flowing porcine blood (platelets) on MZC samples using a custom-built, multi-specimen, laminar flow chamber shown in Figure 6.9 This instrument investigates the adhesion of blood components (platelets) on implant materials.

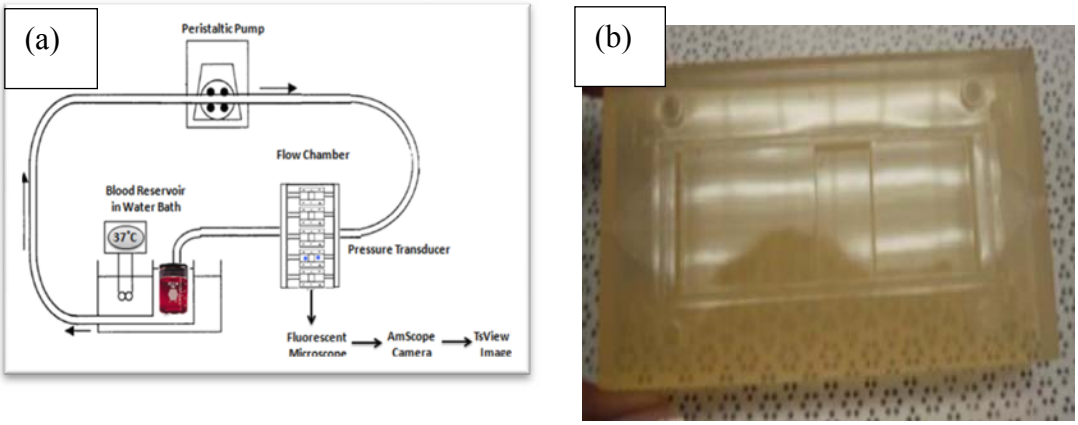


Figure 6.9: (a) Schematic of a closed-loop system for platelet adhesion studies and (b) The dynamic flow chamber for platelet adhesion studies

The flow loop for platelet adhesion studies consisted of a peristaltic pump to drive blood flow, silicon tubes to connect the flow chambers, a blood reservoir and a water bath to maintain the temperature of whole blood at 37 $^{0}$C (Figure 6.9). The velocity of blood flow was maintained at 113 cm/s, which is within the dynamic range of velocities measured in the veins of the upper limbs [214].

Prior to testing all the MZC samples were ultrasonically cleaned for 5 minutes in DI water, followed by cleaning in 70% ethanol for 5 minutes to eliminate impurities and foreign particles on the surface. Additionally, these MZCs were sterilized by exposing them to UV radiation for 40 minutes. The MZCs were placed in a recessed cavity of the chambers of the flow loop (n = 5 samples at a time) and a phosphate buffer saline (PBS) solution was used to prime the loop for 10 minutes. Approximately 500 ml of freshly collected whole porcine blood (Mary's Ranch Inc., Miami, FL) was mixed with 150 ml of sodium citrate anticoagulant. 333.5 ml of 10 mM mepacrine dye solution was added for every 500 ml of whole porcine blood to fluorescently label the platelets [215]. The blood was passed over the metallic samples in the loop for 35 minutes. After each run,

samples were extracted and carefully washed with PBS three times to remove any residual blood components. Platelets that adhered on the surface treated and surface treated MZC that were PGCL coated, were observed under a fluorescent microscope (Nikon Eclipse E 200, Nikon, Melville, NY). The number of platelets adhered to each sample was counted carefully using an image analysis software (Image J, NIH, Bethesda, MD).

A statistical analysis was performed on platelet adhesion data using a one-way ANOVA analysis, followed by post-hoc testing (Tukey HSD). A significant difference between materials was interpreted to occur at $p < 0.05$.

### 6.3.3 Platelet Adhesion Analysis

. In general as reported by Hansi et.al, magnesium alloys revealed few platelets adhered to the surface, whereas a greater amount of fully grown platelets were observed on 316L steel and cobalt chromium alloys [216]. Figure 6.10 shows florescent microscope images of platelets on surface treated MZC. These platelets were globular in shape which are indicative of the platelets being in the resting stage with no activation.

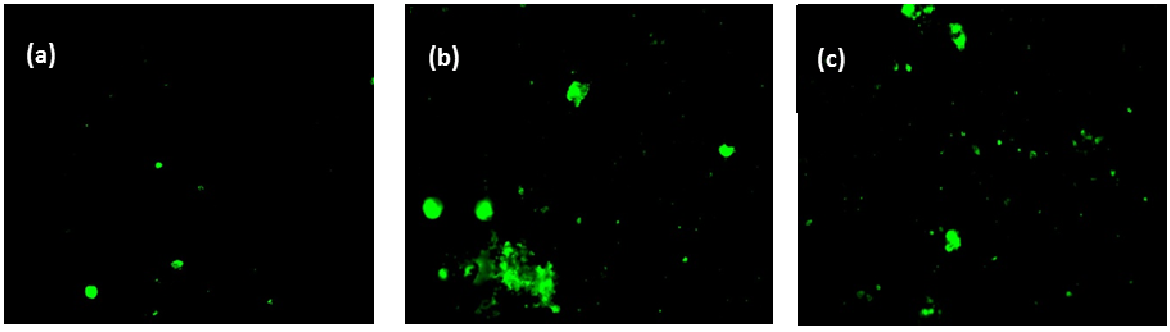


Figure 6.10: Florescent microscopic images of pig platelets adhered to uncoated MZC: (a) mechanically polished (b) anodized and (c) acid etched

Figure 6.11 displays the correlation of number of platelets adhered on the surface treated MZC with the polarity of the surface treated MZC. The anova analysis of platelet adhesion and Tukey test for statistical significance revealed that the platelet adhesion on mechanically polished (MP) MZC was significantly less than that on anodized and acid etched (AE) MZC. As reported by et al. the platelet adhesion and aggregation were controlled by composition of the metals surface oxide film as its relative permittivity (electrostatic forces) influences the amount of adsorbed proteins [217]. These platelet adhesion results further corroborate well with the previously described, XPS (section 4.4) and EDS (section 4.2) that the anodized MZC had higher oxide/hydroxide composition as compared with mechanically polished and acid etched MZC sample. In the case of acid etched MZC even though there was less oxides (when compared to mechanically polished samples) present on the surface, the high surface roughness attracted more number of platelets to get adhered on to its surface. So in the case of surface treated MZC increase in the surface roughness and oxide/hydroxide composition increased the polarity of the surface, which increased the platelet adhesion. The same was observed by et al. in the case of the biodegradable stent material where the polarity of the sample was directly proportional to platelet adhesion [218].

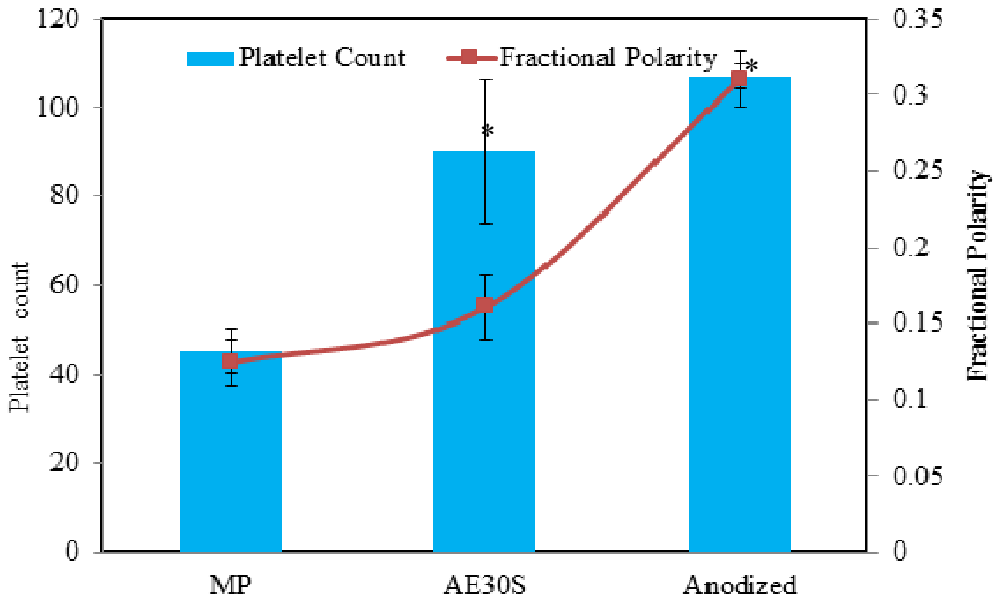


Figure 6.11: Porcine platelets adhered to uncoated MZC and its relation with surface polarity (mean ± SD, n = 3)

Note: * refers to $p < 0.05$ indicating values are significantly different from mechanically polished MZC in one-way ANOVA analysis

Figure 6.12 shows florescent microscope images of platelets on PGCL coated MZC. These platelets were also globular in shape which was indicative of the platelets being in the resting stage with no activation.

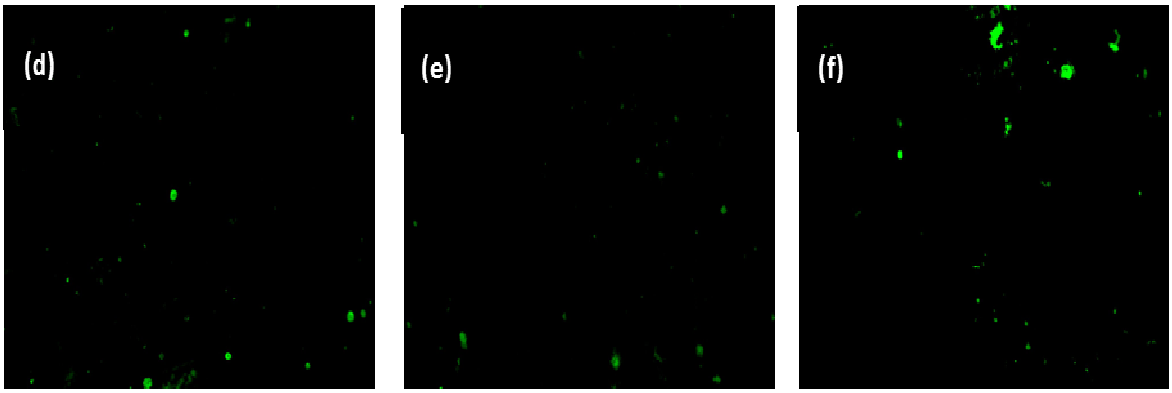


Figure 6.12: Florescent microscopic images of porcine platelets adhered to polymer coated MZC samples: (a) mechanically polished (b) anodized and (c) acid etched

Figure 6.13 displays the correlation of number of platelets with the polarity of the surface treated MZC that were PGCL coated. The anova analysis of platelet adhesion and Tukey test for statistical significance. It was revealed that the platelet adhesion on PGCL coated anodized MZC was significantly less than that on mechanically polished and acid etched (AE) MZC. This may be attributed to the decrease in fractional polarity.

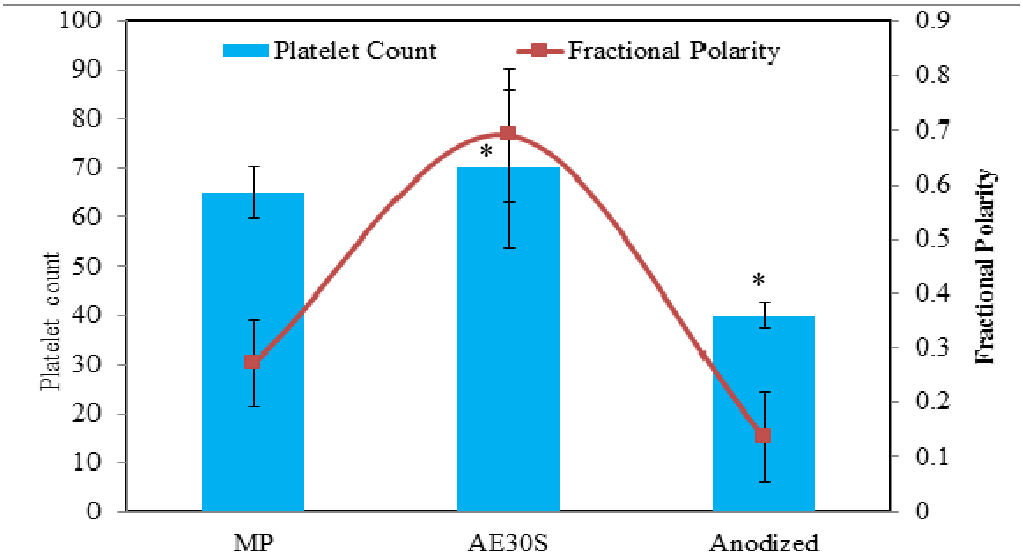


Figure 6.13: Porcine platelets adhered on the surface of polymer coated MZC samples and its relation with polarity (mean ± SD, n = 3)

Note: * refers to $p < 0.05$ indicating values are significantly different from anodized MZC in one-way ANOVA analysis

## 7. ANALYSIS OF MECHANICAL INTEGRITY WITH DEGRADATION TIME

The experimentation in the current research showed that the anodized polymer coated MZC had a corrosion rate of 0.12 mm/year (section 5.4) that is below the required magnesium stent implant corrosion rate (< 0.2 mm/year) with minimal endothelial cell toxicity (section 6.3) and platelet adhesion (section 6.5). To utilize this alloy as biomedical implant the material should also have sufficient strength not only at the moment of being implanted but also when the alloy degrades over the time while in contact with body fluids. This chapter describes different studies that were conducted to evaluate the mass loss and evolution of the strength over the implantation or immersion time [219]. The schematic in Figure 7.1 summarizes the tests performed to analyze the mechanical integrity of the polymer anodized MZC.

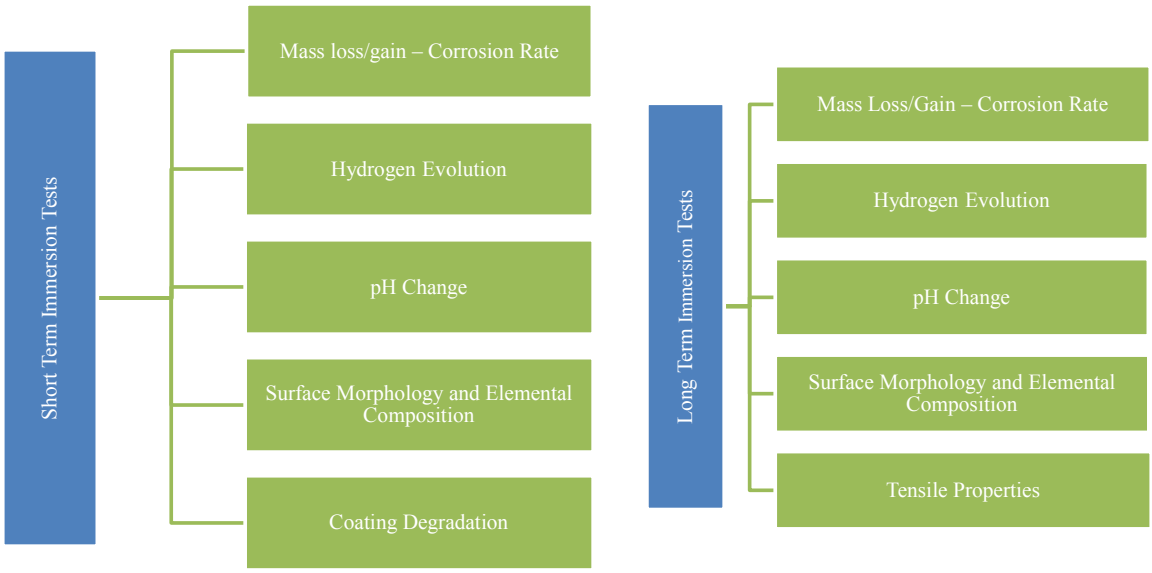


Figure 7.1: Schematic of experiments conducted to analyze the mechanical integrity of the anodized MZC

### 7.1 Immersion Test

According to Pietak et al. [220] the best technique to measure the mechanical integrity of the Mg alloy is to assess the mechanical properties of the alloy as a function of the degradation time. However, this procedure has several shortcomings due to the association of non-soluble degradation products that precipitate on the sample and obscure the mass loss [220]. The mechanical properties can be evaluated using various tests like: three-point bending, tensile tests, nanoindentation, etc. These tests can be performed under physiological conditions or in air.

In the current research, mechanical integrity of the anodized MZCs were analyzed using a very simple and traditional immersion method as a function of degradation time. Additionally, these immersion tests also assist in monitoring degradation mechanism and measuring corrosion rate of the anodized MZCs. Degradation mechanism of the anodized MZC can be analyzed by monitoring parameters like: weight loss/gain, hydrogen gas evolution and pH change at regular intervals. At each interval, SEM/EDS was utilized to visually observe the surface of the corroded sample and analyze the elemental composition of the corroded products on the sample. Further, EIS was utilized to observe the stability of the polymer coating at the same regular intervals of time. In current study immersion tests were performed only on the anodized (uncoated or polymer coated) MZCs as it showed superior corrosion resistance with good biocompatibility and hemocompatibility.

Figure 7.2 shows a schematic representation of the immersion test setup to measure the corrosion rates of the samples. In this setup anodized samples were placed at

the bottom of a beaker filled with PBS, with a funnel placed above the sample. A solution filled measuring cylinder was placed over the funnel to collect and measure the hydrogen gas evolved during the displacement of the solution. The samples were soaked in 300 mL of PBS at 37 $^{o}$C for regular intervals of time (short/long). After each interval of time the samples were cleaned by immersing them in 180 g/l of chromic acid for 20 min.

The weight gain/loss in grams was calculated using the equations 7.1 and 7.2 [36, 221, 222].

$$weight\ gain = \frac{weight\ after\ immersion - weight\ before\ immersion}{surface\ area} \quad 7.1$$

$$weight\ loss = \frac{weight\ before\ immerison - weight\ after\ cleaning}{surface\ area} \quad 7.2$$

The corrosion rates were also calculated from the quantity of hydrogen evolved and weight change in the sample during the immersion test. The corrosion rate (CR, mm/year) was calculated as follows:

$$CR = \frac{tW.10}{\rho AT} \quad 7.3$$

where, t is a constant (8760 h), W is mass loss, g (mass before immersion - mass after cleaning)/surface area, A is the surface area before immersion (cm$^2$), T is the immersion time (h) and ρ is the sample density (g/cm$^3$).

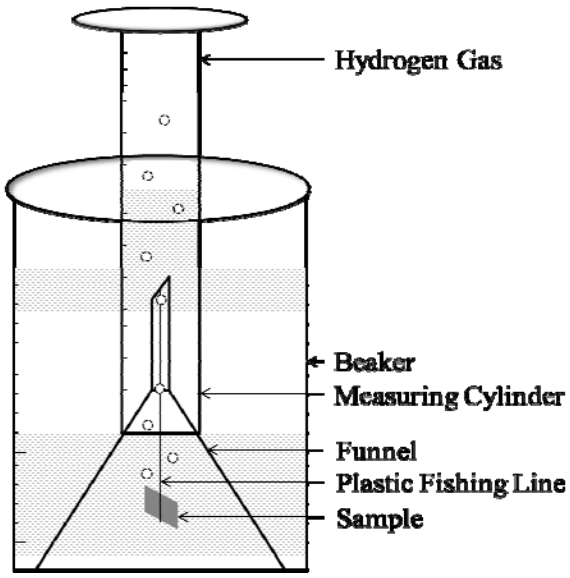


Figure 7.2: Schematic representation of immersion test setup

### 7.2 Short Term Immersion Studies

The short term immersion tests were performed in accordance with ASTM G31-72 [222] by soaking the samples in 300 mL of PBS for short period of time 96 hours (4 days) at 37 $^{o}$C. At regular intervals of time (24, 48, 72 and 96 hours) the corrosion parameters (corrosion rate, hydrogen evolution and pH change), surface morphology and coating stability were analyzed.

### 7.3 Corrosion Rate Determination

With the weight loss/weight gain values obtained from Equations 7.1 and 7.2, corrosion rates were calculated using the Equation 7.3. An average of three different sample's weight loss/gain was measured. The volume of test solution was large enough to avoid any appreciable change in the corrosivity of the samples during the test either through exhaustion of corrosive constituents or by accumulation of corrosive products that might affect further corrosion [222]. The samples were removed from PBS, rinsed in

distilled water, air dried and then weighed before and after each time interval. Once the immersion test was completed, the samples were cleaned by immersing in 180 g/l of chromic acid for 20 min. Calculated weight gain (grams) and corrosion rate (mm/year) are presented in the Figure 7.3. For uncoated anodized MZCs the weight gain and corrosion rate gradually increased with immersion time. However, anodized MZCs with PGCL coating's weight gain and corrosion rate has no significant difference with immersion time. This can be attributed to the PGCL coating that acted as passive layer to corrosion rate.

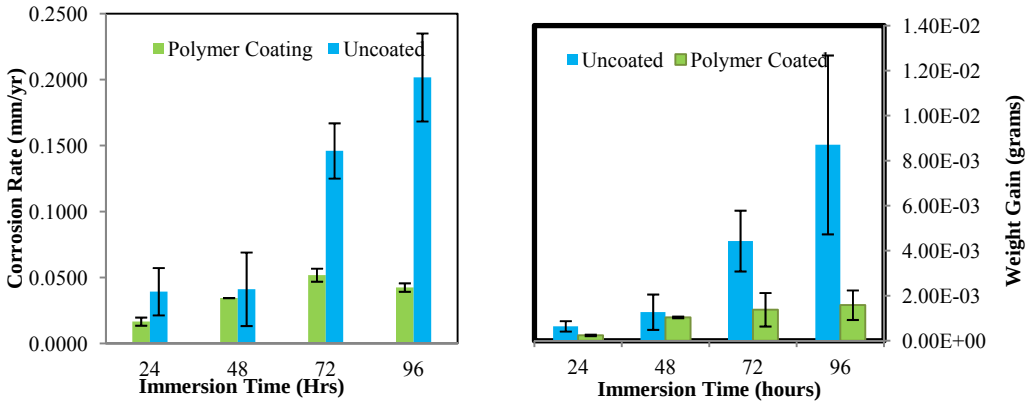


Figure 7.3: Corrosion rate and weight gain of PGCL coated and uncoated anodized MZCs in PBS at 37 °C

### 7.4 Surface Morphology Analysis

Figure 7.4 (a)–(d) shows the surface morphologies of uncoated anodized MZCs after regular intervals of immersion in PBS. It was noticed that the anodized MZC's surface was with a layer of corrosion products (Figure 7.4 (a)). After 24 hours of immersion the coating changed to a block and nodular structure shown in Figures 7.4 (b), (c) and (d) with increased amount of corrosion. As the immersion time increased the size of the block and nodular decreased and the coating appeared denser shown in Figures 7.4 (c)

and (d). This is attributed to the formation of corrosion products that has phosphates, during the immersion in PBS [223]. This was further proved by the EDS analysis (Table 7.1) where the phosphorus and oxygen content increased after 72 and 96 hours of immersion.


Figure 7.4: SEM photo micrographs of uncoated anodized MZCs in PBS at 37 °C for (a) 24, (b) 48, (c) 72 and (d) 96 hours

Table 7.1: EDS analysis of uncoated anodized MZCs in PBS at 37 °C

| **Immersion Time** | **Composition (Wt %)** | | | | | |
|---|---|---|---|---|---|---|
| | **Mg** | **Zn** | **Ca** | **O** | **P** | **K** |
| 24 hours | 40.11 | 1.84 | 0.93 | 37.46 | 13.74 | 5.92 |
| 48 hours | 37.7 | 1.52 | 0.34 | 41.66 | 13.53 | 5.25 |
| 72 hours | 30.45 | 1.37 | 0.58 | 43.62 | 17.82 | 6.16 |
| 96 hours | 32.11 | 1.19 | 0.38 | 44.1 | 16.09 | 6.13 |

Figure 7.5 (a)–(d) depicts the surface morphologies of the anodized MZC coated with PGCL during short term. It can be seen that the PGCL coating was covered by corrosion products in Figure 7.5 (a) after 24 hours of immersion with minute polymer peeling. Figures 7.5 (b), (c) and (d) reveal that the amount of corrosion products increased with increasing immersion time. This was further proved by the EDS analysis